國立臺灣大學工學院機械工程學研究所

碩士論文

Department of Mechanical Engineering

College of Engineering

National Taiwan University

Master’s Thesis

# 探討單向方波電流電解對於水平銅管池沸騰熱傳影響

# Effects of unidirectional square wave current electrolysis of pool boiling heat transfer on a horizontal copper tube

唐海田

TANG, HAITIAN

指導教授：陳炳煇 博士

Advisor: Ping-Hei Chen, Ph.D.

中華民國 113 年 7 月

July，2024

doi:10.6342/NTU202404361

# 國立臺灣大學碩士學位論文
# 口試委員會審定書
# MASTER'S THESIS ACCEPTANCE CERTIFICATE
# NATIONAL TAIWAN UNIVERSITY

探討單向方波電流電解對於水平銅管池沸騰熱傳影響

Effects of unidirectional square wave current electrolysis of pool boiling heat transfer on a horizontal copper tube

本論文係唐海田(姓名)R10522122（學號）在國立臺灣大學 機械工程學研究所完成之碩士學位論文，於民國 113 年 07 月 24 日承下列考試委員審查通過及口試及格，特此證明。

The undersigned, appointed by the Department of Mechanical Engineering，College of Engineering on 24 (date) 07 (month) 2024 (year) have examined a Master's thesis entitled above presented by TANG，HAITIAN (name)R10522122 (student ID) candidate and hereby certify that it is worthy of acceptance.

口試委員 Oral examination committee:

| | | |
|---|---|---|
| ____________________<br>（指導教授 Advisor） | ____________________ | ____________________ |
| ____________________ | ____________________ | ____________________ |
| ____________________ | ____________________ | ____________________ |

系主任/所長 Director: ____________________

doi:10.6342/NTU202404361

# 誌謝

時光荏苒，三年的研究生活轉瞬即逝。回想當初剛入學的自己，對於科學研究的基本步驟和方法還懵懵懂懂，而如今能夠順利完成人生的第一篇學位論文，這是一個重要的里程碑。這一路走來，我深感這份成果凝聚了無數人的幫助與支持，我心中充滿了無限的感激之情。

首先，我要衷心感謝我的指導教授陳炳煇老師。感謝老師在整個研究過程中的悉心指導與支持，每當我在研究中遇到瓶頸或困難時，老師總是耐心地提供寶貴的建議與意見，這讓我受益匪淺，並且為我指引了前進的方向。

我要感謝研究室的同學、學長以及研究夥伴們，感謝你們在整個研究過程中經常用心聆聽我的報告，與我深入討論研究和實驗的相關問題，分享你們寶貴的見解和經驗，並提供了許多方法與建議，這些幫助對我來說非常重要。

此外，我還要感謝在研究所期間與我一起修課的同學，以及台大晨曦社的朋友們。感謝你們慷慨地分享研究經驗和交流心得，並在心靈上給予我許多支持與啟發，這不僅促進了我的學術成長，也讓我個人收穫良多，進步顯著。

在我入學的時候，正值 COVID-19 疫情期間，我要特別感謝中華扶輪教育基金會及 PP Jasmine, 感謝您們在我碩士班一年級時，疫情期間無私地提供獎學金，給予了我極大的經濟支持，使我能專注於學業和研究，不必為經濟問題擔憂。

我要衷心感謝我的爸爸媽媽、家人以及曾幫助過我的所有朋友。感謝爸爸媽媽支持我讀研究所的決定，並無私地為我支付在台灣的留學費用。感謝我的朋友們，在我壓力大的時候，你們總是安慰我、鼓勵我，為我加油打氣。

最後，我也要感謝自己，感謝一路走來從未拋棄、不放棄的自己。雖然在研究過程中，我曾多次質疑自己的能力，但我始終堅守初心，沒有放棄最初的理想和決心。

doi:10.6342/NTU202404361

# 摘要

沸騰傳熱具有高效的傳熱效率，可以在較小的溫度差的情況下進行大量的的熱量傳遞，從而提升能量傳遞的效率和系統性能，廣泛應用於熱交換器，電子冷卻和工業過程中。本研究探討了單向方波電流電解對水平放置銅管池沸騰傳熱性能的影響。本研究的實驗在一大氣壓的飽和狀態下進行，使用碳酸鈉溶液作為工作流體。通過電解水產生氫氣以增加沸騰時的核化點數量，進而提升相變位點數量，從而增強熱傳性能。本研究分析並比較了無電解、直流電流電解和單向方波電流電解條件下的傳熱過程中的傳熱係數（Heat Transfer Coefficient）和氣泡動態特性。實驗的結果顯示，當電流為12mA時，單向脈衝電流頻率在25mHz電解的情況下，熱傳係數(HTC)的提升最為顯著，相較於無電解情況下，熱傳係數提升了1.31倍。實驗中透過高速攝影機進行捕捉沸騰時氣泡的圖片，進而觀察在不同電解條件下氣泡動態特性。我們還比較了在不同熱通量度條件下，在水平銅管上下表面的溫度分佈情況。這些研究結果對在提升能量傳遞效率和系統性能方面具有潛在應用價值。

關鍵詞：池沸騰，電解，氣泡動態分析

# Abstract

Boiling heat transfer is crucial due to its high heat transfer efficiency, allowing significant heat transfer with slight temperature differences, thereby enhancing energy efficiency and system performance. This is especially important in power generation, electronics cooling, and industrial processes. This research examined how unidirectional square wave current electrolysis influences the heat transfer performance of a copper tube positioned horizontally. The experiment was conducted at atmospheric pressure and saturation conditions, using sodium carbonate solution for the working fluid. We used a high-speed camera to capture images of the process for analyzing bubble dynamics. This study compared the heat transfer coefficient （HTC） and bubble dynamics in the heat transfer processes with and without electrolysis, including direct current (DC) electrolysis and unidirectional square wave current electrolysis. The experimental results show that when the current is 12mA, under unidirectional pulse current electrolysis at a frequency of 25mHz, the heat transfer coefficient (HTC) is enhanced the most, with an increase of 1.31 times compared to the condition without electrolysis. We then analyzed the bubble dynamics to investigate bubble aggregation on the upper and lower surfaces of the horizontal copper tubes under different heat flux conditions. The bubble formation and detachment processes on both surfaces of the tube were examined using high-speed camera comparisons to determine the nature of the bubbles. The dynamics properties of the bubbles were analyzed under different electrolysis conditions. These findings are significant as they contribute to the understanding of boiling heat transfer and can potentially be applied in various industries to enhance energy efficiency and system performance.

**Keywords: pool boiling, electrolysis, bubble dynamics analysis**

doi:10.6342/NTU202404361

# Nomenclature

| | |
|---|---|
| $A$ | total surface area |
| $A_c$ | cross-sectional area of the sample |
| $A_s$ | surface area at the out diameter of the sample |
| $E$ | equivalent weight |
| $E$ | total energy |
| $F$ | gas evolution efficiency |
| $f_{lv}$ | area fraction of liquid and vapor |
| $f_{sl}$ | area fraction of solid and liquid |
| $F$ | Faraday constant |
| $G$ | gravitational acceleration |
| $h_{lv}$ | latent heat for liquid and vapor |
| $h_P/ h_{B0}, h_D/ h_{B0}$ | heat transfer coefficient ratio |
| $I$ | current |
| $K$ | thermal conductivity of copper |
| $K$ | The surface roughness factor |
| $L$ | length of the sample |
| $M$ | mass of elements |
| $M$ | molar mass |
| $N$ | number of moles |
| $Pa$ | pressure of air |
| $Ps$ | pressure of saturated vapor |
| $P_0$ | atmosphere pressure |
| $P_\sigma$ | pressure due to surface tension |
| $P_l$ | pressure within the liquid |
| $P_{liquid}$ | pressure within the liquid |
| $Q$ | heat flux over the surface area of the sample |

doi:10.6342/NTU202404361

| | |
|---|---|
| $Q$ | electric charge |
| $Qin$ | heat input |
| $Qloss$ | heat loss |
| $R$ | roughness ratio |
| $r_c$ | radius for the thermocouples location from the center of the sample |
| $r_0$ | outer radius of the sample |
| $T$ | total time |
| $T_{5mm}$ | temperature of the thermocouple located at 5 mm depth of the sample |
| $T_{10mm}$ | temperature of the thermocouple located at 10 mm depth of the sample |
| $T_m$ | mean temperature of four thermocouples at 10 mm depth of the sample |
| $T_s$ | Surface temperature |
| $T_{sat}$ | saturated temperature of the working fluid |
| $\Delta T_w$ | wall superheat |
| $vol_m$ | molar volume |
| $V$ | volume of the fluid |
| $V$ | voltage |
| $V_h$ | volumetric generation rate for hydrogen |
| $Vv$ | volumetric generation rate for vapor |
| $\Delta x$ | depth difference of the thermocouple’s location |
| $Z$ | height of the fluid |
| $Z$ | electro-chemical equivalent |
| ~ | approximately |

doi:10.6342/NTU202404361

## Greek Symbols

| | |
|---|---|
| $\Delta$ | difference |
| $\Gamma$ | Liquid/gas surface tension |
| $\gamma_{sl}$ | the surface tension of the solid-liquid interface |
| $\gamma_{so}$ | surface tension of solid-vapor interface |
| $\Theta$ | contact angle |
| $\theta^*$ | the apparent contact angle |
| $\theta_\gamma$ | the equilibrium contact angle from Young‘s equation on an ideal solid without roughness |
| $V$ | Valence |
| $\rho$ | density of the fluid |
| $\rho_v$ | the density of the vapor |

## Abbreviations

| | |
|---|---|
| CA | contact angle |
| DI | deionized |
| CHF | critical heat flux |
| HTC | heat transfer coefficient |
| DC | direct current |
| Ra | average surface roughness |
| ONB | the onset of nucleate boiling |
| P | test conditions under Unidirectional square wave pulsed current |
| D | test conditions under direct current |
| USWPC | Unidirectional square wave pulsed current |
| CCTCL. | Chuan Chi Trading Co., Ltd. |

doi:10.6342/NTU202404361

## Table of Contents

口試委員審定書 ........................................................................ i

誌謝 ........................................................................ ii

摘要 ........................................................................ iii

Abstract ........................................................................ iv

Nomenclature ........................................................................ v

Table of Contents ........................................................................ viii

List of Figures ........................................................................ xi

List of Tables ........................................................................ xv

Chapter 1 Introduction ........................................................................ 1

1.1 Preface ........................................................................ 1

1.2 Background ........................................................................ 4

1.3 Literature review ........................................................................ 9

1.3.1 Passive techniques ........................................................................ 10

1.3.1.1 Surface roughness and wettability modification ............ 10

1.3.1.2 Surface and microstructure expansion ............................ 14

1.3.2 Active techniques ........................................................................ 17

1.3.2.1 Vibration-induced effect ........................................................ 17

1.3.2.2 Electric field control ........................................................ 21

1.4 Research purpose and objective ........................................................ 26

1.5 Thesis structure ........................................................................ 27

doi:10.6342/NTU202404361

**Chapter 2 Theory ........................................................................28**

**2.1 Surface energy** ..........................................................................28

**2.2 Effect of surface wettability on pool boiling and static contact angle** .30

**2.2.1 Young’s equation.** ..........................................................................34

**2.2.2 Wenzel’s model** ..........................................................................37

**2.2.3 Cassie-Baxter model** ..........................................................................41

**2.3 Electrolysis** ..........................................................................43

**Chapter 3 Experiment methodology ................................................47**

**3.1 Experiment setups** ..........................................................................47

**3.2 Preparation of copper tube** ..........................................................................52

**3.3 Working fluid preparation** ..........................................................................55

**3.4 Experimental Procedure** ..........................................................................57

**3.5Data Reduction** ..........................................................................58

**3.6 Uncertainty Analysis** ..........................................................................60

**Chapter 4 Results and Discussion ....................................................62**

**4.1 Verification of the Experimental Setup** ..........................................................62

**4.2 Mechanism of electrolytic boiling heat transfer** ....................................63

**4.3 Comparison of Unidirectional Square Wave Pulsed Current and Direct Current Electrolysis in Pool Boiling Heat Transfer** ....................................66

**4.4 Comparison of boiling curves in using different frequency of unidirectional Square Wave Pulsed Current Electrolysis in Pool Boiling Heat Transfer** ..........................................................................79

**4.5Bubble dynamics** ........ 81

**4.6Circumferential surface temperature difference** ........ 84

**Chapter 5 Conclusions and Future Prospects ........ 88**

**5.1 Conclusions** ........ 88

**5.2Future prospects** ........ 89

**Reference ........ 91**

doi:10.6342/NTU202404361

# List of Figures

Figure 1. The experimental framework proposed by Nukiyama. ................................ 5

Figure 2. Pool Boiling Curves with Water as Working Fluid at Atmospheric Pressure, Illustrated by Nukiyama[1]. ................................ 6

Figure 3. Pool boiling curve with water as the working fluid under atmospheric pressure. [2]. ................................ 7

Figure 4. Heat transfer enhancement techniques [3]. ................................ 9

Figure 5. Visualization of Bubble Formation and Departure in Nucleate and Transitional Boiling [4]. ................................ 12

Figure 6. Boiling curves Across the range from nucleate boiling to film boiling of three test surfaces[4]. ................................ 13

Figure 7. SEM images of (a) flat surface, (b) deposition of cubic $Cu_2O$ crystals on the anodic surface, and (c) deposition of dendritic copper branches on the cathodic surface, along with the respective static contact angles (CAs) of deionized water on each surface. ................................ 16

Figure 8.HTCs of different surfaces ................................ 16

Figure 9. Boiling HTCs in terms of heat flux of DI water for different vibrational frequencies[8]. ................................ 18

Figure 10. Boiling HTCs in terms of heat flux of nanofluid for different vibrational frequencies[8]. ................................ 19

Figure 11. Vibration arrangement. ................................ 20

Figure 12. boiling curves of different frequencies and amplitudes of vibration ......... 21

doi:10.6342/NTU202404361

Figure 13. Boiling curves in different electrolytic current, with the current of 0A,0.01A,0.02A,0.04A,and 0.08A[10]. .......... 23

Figure 14. Pool boiling HTCs and HTC enhancements of different input currents[10].23

Figure 15. Pool boiling curves of (a) NaBr (b) MEGA-10 (c) SDS (d) DTAB. Black lines represent plain DI water, red lines represent input potential of -0.1V and blue lines represent input potential of -2.0V. .......... 25

Figure 16. Turning bubbles on and off with a potential switch. (a) The experimental setup involved a 2.6 mM SDS solution (negatively charged), where potential was applied to the silver foil surface with an immersed counter electrode made of titanium (b) Switching from -0.1V to -2.0V ceased the bubble nucleation. (c) Switching from -2.0V to -0.1V promoted the bubble nucleation. .......... 25

Figure 17. Contact angle effects at the liquid-gas-solid interface-wetting. .......... 30

Figure 18. Contact angle effects at the liquid-gas-solid interface-non-wetting. .......... 31

Figure 19. CHF values of TiO2 superhydrophilic surface and copper surface [14]. 33

Figure 20. The schematic of Young’s model. .......... 35

Figure 21. The Cross-section of a liquid drop on an ideal surface. .......... 36

Figure 22. The schematic of Wenzel’s model. .......... 39

Figure 23. Schematic of the drop in the Wenzel’s model. The radius of the drop is a. The smooth region is b. [19] .......... 39

Figure 24. The schematic of the Cassie-Baxter model. .......... 41

Figure 25. (a) side-view, (b) top-view. of the drop in the Cassie-Baxter state [19]. ... 42

Figure 26. Schematic of the experimental setup. .......... 50

Figure 27. Design of the experimental test section. .......... 51

Figure 28. Schematic of the experimental setup. .......... 52

doi:10.6342/NTU202404361

Figure 29. Surface profile of the polished copper measured by the laser confocal microscope. .......... 53

Figure 30.Laser scanning confocal microscope. .......... 54

Figure 31. Contact angle goniometer. .......... 56

Figure 32. Pool boiling curves of DI water and Sodium carbonate solution as working fluid over a copper tube. .......... 56

Figure 33. Cylindrical Copper Tube with DI Water as working fluid of Pool Boiling Curves and Previous Studies and Rohsenow Correlation. .......... 62

Figure 34.Mechanism of electrolytic pool boiling. .......... 64

Figure 35.The volumetric generation rate of hydrogen gas at the heat flux of ~3.74 $kW/m^2$ in pool boiling. .......... 66

Figure 36.Waveforms of Direct Current and unidirectional square wave currents. .......... 67

Figure 37. Pool boiling curves for electrolysis ($Na_2CO_3$ water solution,Direct Current). .......... 72

Figure 38. HTCs of test conditions for electrolysis( $Na_2CO_3$ water solution ,Direct Current). .......... 72

Figure 39. Pool boiling curves for electrolysis ($Na_2CO_3$ water solution,.Unidirectional Square Wave Pulsed Current). .......... 73

Figure40. HTCs of test conditions for electrolysis ($Na_2CO_3$ water solution , unidirectional square wave plused current). .......... 73

Figure 41.Comparison of pool boiling curves for unidirectional square wave current and DC current at 3mA. .......... 75

Figure 42.Comparison of HTC curves of unidirectional square wave current and DC current at 3mA. .......... 75

doi:10.6342/NTU202404361

Figure 43.Comparison of pool boiling curves for unidirectional square wave pulsed current and DC current at 8mA. ........ 76

Figure 44.Comparison of HTC curves of unidirectional square wave current and DC current at 8mA. ........ 76

Figure 45.Comparison of pool boiling curves for unidirectional square wave pulsed current and DC current at 12mA. ........ 77

Figure 46.Comparison of HTC curves of unidirectional square wave pulsed current and DC current at 12mA. ........ 77

Figure 47.Comparison of pool boiling curves for unidirectional square wave current and DC current at 16mA ........ 78

Figure 48. Comparison of HTC curves of unidirectional square wave current and DC current at 16mA. ........ 78

Figure 49.Comparison of pool boiling curves for unidirectional square wave current in different frequencies at 12mA ........ 80

Figure 50.High-speed imaging was employed to document the dynamics of bubbles at varying heat flux intervals during the course of electrolytic boiling experiments conducted with a sodium carbonate solution serving as the working fluid. ........ 82

Figure 51. Bubble Dynamics at a Heat Flux of 107.74 $kW/m^2$ During USWPC Electrolytic Boiling Using $Na_2CO_3$ Solution as the Working Fluid ........ 83

Figure 52. Temperature differences of copper tube surface for the test conditions B0, P1 and P3. ........ 85

# List of Tables

Table 1. Classification of different levels of wettability. ........................................... 32

Table 2. A summary of the effects of wettability on boiling...................................... 34

Table 3. Measurement results of the contact angle between water and sodium carbonate solution ....................................................................................................................... 55

Table 4 Uncertainty analysis with a plain copper tube using DIwater as the working fluid............................................................................................................................. 61

Table 5 . Experimental conditions for electrolytic pool boiling using $Na_2CO_3$ water solution as the working fluid. ........................................................................... 68

Table 6. The enhancement ratio of HTCs at a heat flux of 107.74 kW/m². ................ 70

Table 7.The enhancement ratio of HTC at a heat flux of 363.41 kW/m².................... 70

doi:10.6342/NTU202404361

# Chapter 1 Introduction

## 1.1 Preface

Boiling, a process of vigorous vaporization, is a fascinatingly complex phenomenon that occurs simultaneously on the surface and within the liquid. The primary location of the process is at the solid-liquid interface, where steam bubbles rapidly form, grow, and detach. Normally, the solid surface exhibits a temperature surpassing the liquid's saturation temperature (boiling point) under the same pressure conditions. This temperature difference ($Ts > Tsat$ at $P_{liquid}$) is a key factor in boiling.

Boiling is a process of vaporization of the liquid. However, in contrast to evaporation, boiling is characterized by high intensity, with many bubbles forming within the liquid. These bubbles then expand and rise to the surface, bursting and releasing gas. The temperature at which a particular liquid undergoes a phase change from liquid to gas, under a specified external pressure, is referred to as the boiling point of the liquid. Before the temperature reaches the point at which the liquid begins to boil, tiny bubbles first appear on the walls of the container. Initially, these tiny bubbles adhere to the container walls. As the temperature rises, the tiny bubbles gradually increase in size. When they become large enough, they begin to rise. During the ascent, the volume of the gas inside the bubbles may undergo a slight decrease. As the temperature rises, the bubbles expand once more and rapidly ascend to the surface of the liquid, where they subsequently burst, releasing the gas within.

The boiling process can also be explained from a microscopic perspective. It is always the case that a small amount of air is dissolved within the liquid. Furthermore, Air can also be found on the walls of the container and in the surface cracks of solid impurities in the liquid. As the temperature of the liquid within the vessel rises, the kinetic energy of the air molecules also increases, thereby augmenting their thermal movement. This causes the air to separate from the liquid and exist in a gaseous state within the liquid, forming tiny bubbles. At the interface between the bubbles and the liquid, a small number of liquid molecules also evaporate into a gaseous state, entering the bubbles. Therefore, the bubbles contain both air and saturated vapor. The pressure within the bubbles is the sum of the pressure of the air ($\boldsymbol{P_a}$) and the pressure of the saturated vapor ($\boldsymbol{P_s}$). The pressure outside the bubbles is the sum of the atmospheric pressure ($\boldsymbol{P_0}$), the pressure due to surface tension ($\boldsymbol{P_\sigma}$), and the pressure within the liquid($\boldsymbol{P_l}$).$P_l = \rho g h$ where $\rho$ stands for the density of the working fluid, and $h$ stands for the depth of the bubbles within the fluid. Consequently, the relationship can be expressed as follows:

$$P_a + P_s = P_0 + P_\sigma + P_l \tag{1}$$

In general, it can be assumed that $P_\sigma \ll P_l \ll P_0$ , $P_\sigma$ $and$ $P_l$ can be ignored, thus simplifying the relationship to

$$P_a + P_s = P_0 \tag{2}$$

At this stage, the bubble volume is relatively small, and the buoyant force acting on them is minimal, preventing them from rising to the liquid surface.

As the temperature increases, the pressure inside the bubbles rises, causing them to expand in volume. This increases the buoyant force acting on them, allowing them to break free from the container walls and the surfaces of impurities and start to rise. At the point at which the temperature reaches a level at which the vapor pressure within the bubbles $(\boldsymbol{P_a} + \boldsymbol{P_s})$ is equal to the atmospheric pressure ($\boldsymbol{P_0}$), and $\boldsymbol{P_a} + \boldsymbol{P_s} > \boldsymbol{P_0}$, the internal pressure exceeds the external pressure. This causes the bubbles to expand further. When bubbles ascend to the liquid's surface, they rupture and discharge the contained air and vapor, leading to the process of boiling.

Accordingly, the condition for boiling is that the saturated vapor pressure within the bubbles is equal to the external pressure. The saturated vapor pressure depends on temperature; thus, at a constant external pressure, the boiling point of the liquid is also continuous. As external pressure rises, the fluid must be heated to a higher temperature to increase the saturated vapor pressure within the bubbles and achieve boiling. Consequently, the boiling point of the liquid is observed to increase with an increase in external pressure and decrease with a reduction in external pressure.

If a liquid has been boiling for an extended period, the air within it is primarily expelled, rendering it challenging to form bubbles. Even when heated to a temperature above its boiling point, the liquid may not boil. Such a liquid is termed a superheated liquid. In a superheated liquid, the high kinetic energy of the molecules gives rise to intense thermal motion. At a specific point within the liquid, due to the rapid movement of high kinetic energy molecules to other locations, the surrounding molecules with lower kinetic energy cannot immediately fill the void, resulting in the formation of a small vacuum region known as a cavitation bubble. Once formed, a significant number of molecules rapidly evaporate into the bubble. Given the elevated temperature, the saturated vapor pressure within the bubble is also considerable, resulting in a rapid expansion and the release of a substantial quantity of high-temperature gas, akin to an explosion. This phenomenon is designated as explosive boiling. If the temperature of the gas is sufficiently elevated and the quantity of gas released is considerable, it can result in the container being ruptured. Consequently, high-pressure boilers must have measures to prevent and avoid explosive boiling.

doi:10.6342/NTU202404361

## 1.2 Background

The study of boiling phenomena can be divided into two primary categories: pool boiling and flow boiling. Pool boiling, also known as large-space boiling, involves boiling that occurs on a heated surface submerged in a large volume of liquid. In addition to the convective movement caused by the boiling, the liquid in the pool remains static. Flow boiling is the phenomenon in which a liquid is circulated through a pipeline by a pump and undergoes the boiling process.

In 1934, Nukiyama [1] conducted a classical experiment on pool boiling. The structure of his experiment is shown in **Figure 1**. An electrically heated platinum filament is immersed in water, and the two ends of the filament are energized. This allows the heating power to be obtained by multiplying the current flowing through the filament with the voltage at its ends. The temperature can then be deduced from the resistance of the platinum filament.

doi:10.6342/NTU202404361

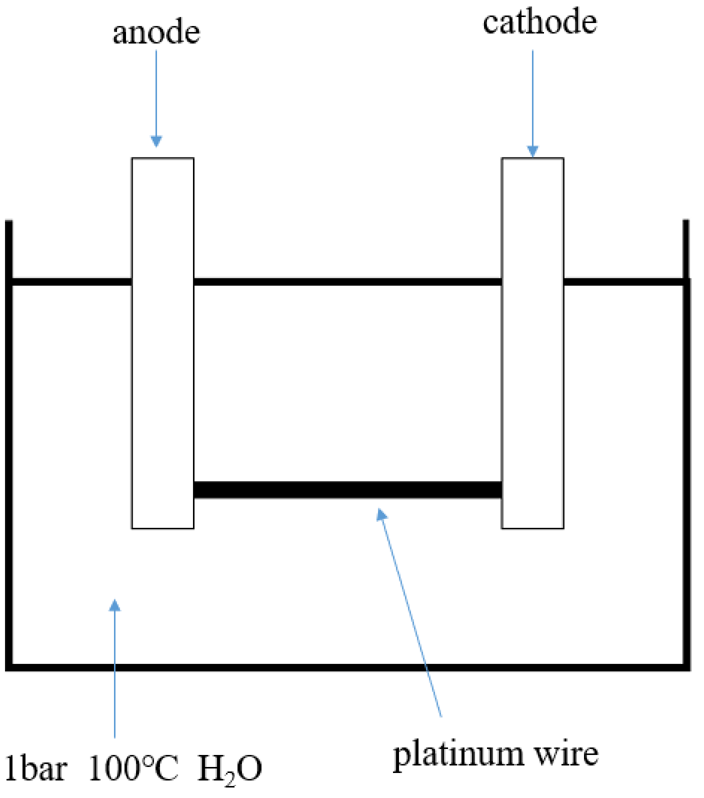

Figure 1. The experimental framework proposed by Nukiyama.

The findings of this study can be visually depicted through graphical representation, as illustrated in **Figure 2,** where the relationship between the temperature of the platinum wire and the heat flux is graphed.

doi:10.6342/NTU202404361

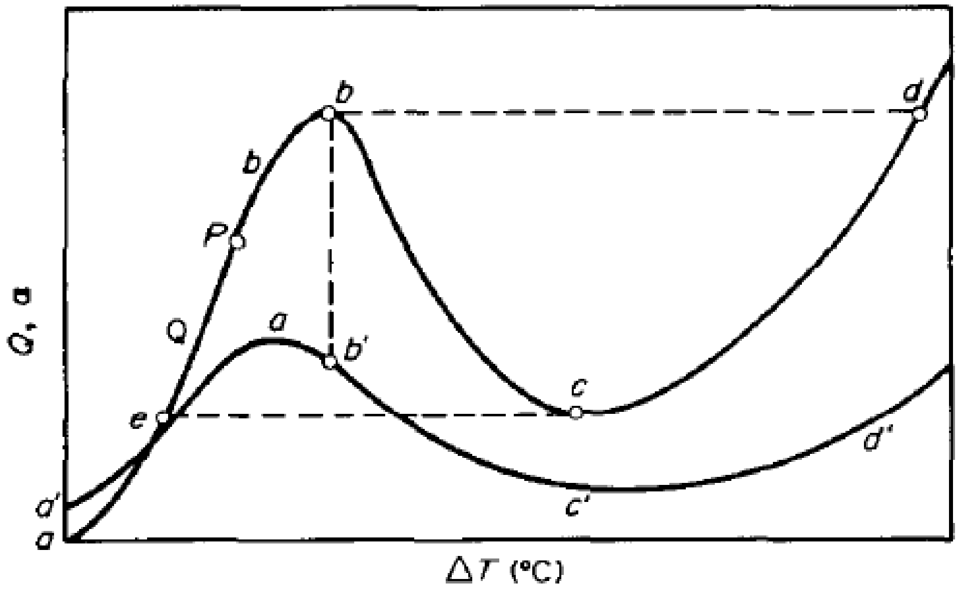

Figure 2. Pool Boiling Curves with Water as Working Fluid at Atmospheric Pressure, Illustrated by Nukiyama[1].

Figure 2 presents two pool boiling curves corresponding to the heating and cooling processes. The two curves do not coincide. During the heating process, the system transitions from natural convection to nucleate boiling, where the heat flux peaks as the surface temperature increases. As the temperature difference rises, the system enters the film boiling regime, characterized by an initial decline in heat flux followed by a gradual increase. In contrast, during the cooling process, the vapor film formed during heating remains stable for an extended period, delaying the transition back to nucleate boiling. This persistence leads to a different cooling path, where the temperature differential is lower than during the heating phase. The discrepancy between the heating and cooling curves results in a characteristic hysteresis loop, underscoring the inherent asymmetry in phase-change heat transfer processes.

The relationship between wall superheat, ΔTsat, and wall heat flux, q, during pool boiling of a saturated liquid was first elucidated by Nukiyama [1], as depicted in **Figure 3.**

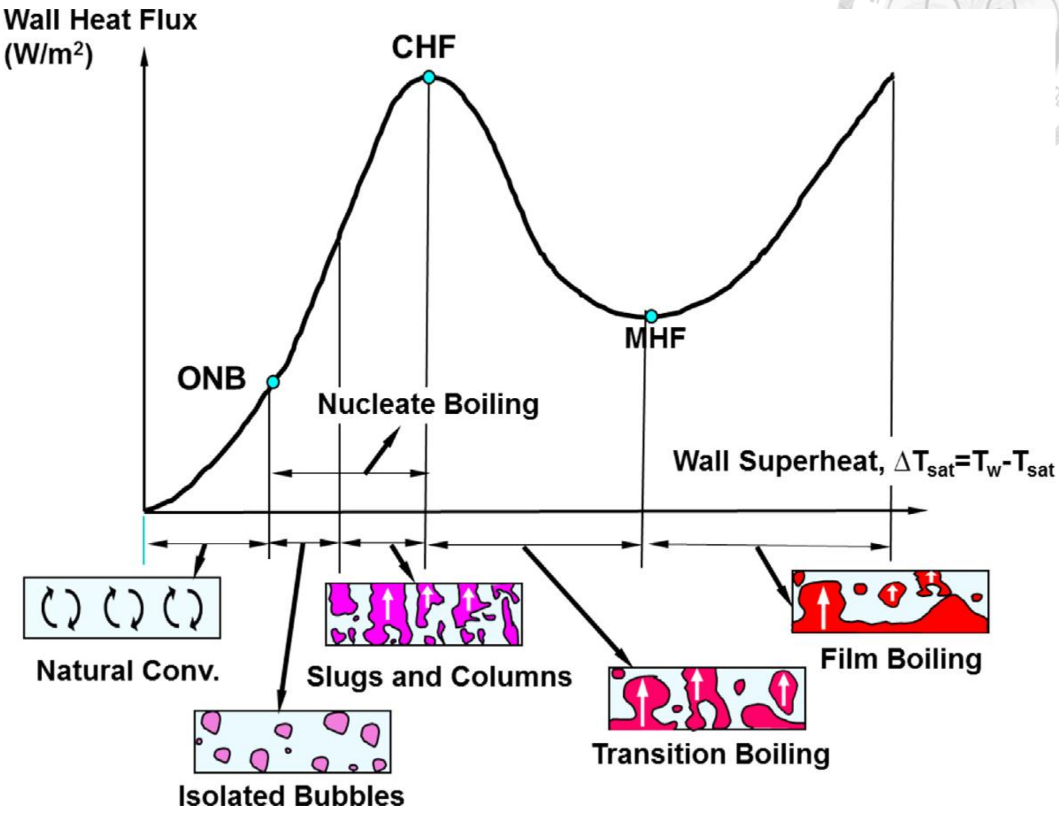

Figure 3. Pool boiling curve with water as the working fluid under atmospheric pressure. [2].

The process of pool boiling can be classified into four discrete phases: ①natural convection, ②nuclear boiling, ③transition boiling, and ④film boiling as illustrated in **Figure 3**.

The initial stage of heat transfer is known as natural convection. In this stage, the fluid flow is caused by the natural convection process, whereby the liquid is slightly overheated. In general, the degree of overheating does not exceed 5 degrees Celsius. The heated liquid rises due to the natural convection process, which causes the liquid to evaporate.

The onset of boiling (ONB) represents the point at which natural convection ceases and nucleate boiling commences. The boiling stage can be further subdivided into two distinct regions, as illustrated in **Figure 3.**In the first region, called isolated bubbles, the nucleation sites are activated, and the bubbles are generated, grown, and detached, all in independent motions. In the second stage, designated as "slugs and columns", bubbles converge and detach from the heated surface in jets. They then travel on the heated surface in large bubbles or air bombs.

As the nuclear-boiling state progresses, the bubbles merge into gas columns, which limits the heat exchange near the surface. Once the peak heat flux is reached, this value is designated as the critical heat flux（CHF）,representing a pivotal point in the transition from boiling to another phase. During the transition boiling phase, the boiling phenomenon may be unstable and is a complex region where part of the heated surface is in the membrane boiling region, oscillating between the nuclear and membrane boiling phases and part of the membrane boiling region of the air-bomb and air-column type.

The membrane boiling region is defined as a state in which a film of gas covers the heated surface, the gas film separates the liquid and does not contact the heated surface, causing instability at the gas-liquid phase interface where gas bubbles emerge from the surface and enter the liquid.

In contrast, film boiling involves a large vapor layer covering the entire test surface. This is due to the suboptimal heat exchange at the wall surface, which may result in the wall overheating and a rapid increase in temperature. Consequently, to guarantee the integrity of the experimental system and prevent it from burning out, it is of paramount importance to closely monitor the critical heat flux.

## 1.3 Literature review

The process of boiling is employed in a multitude of industrial contexts for a plethora of applications, including the production of steam, the purification of substances, the cooling of nuclear reactors, the processing of metals, the regulation of air temperature, refrigeration, the management of fluids, the generation of power, and the cooling of electronic devices. In thermal transfer enhancement, technological solutions can be employed to accelerate heat dissipation. These methods are typically classified as either active techniques and passive techniques. As illustrated in **Figure 4**, active enhancement techniques encompass methodologies such as ultrasonic enhancement and electrohydrodynamics. In contrast, passive enhancement techniques comprise strategies including the expansion of surface area, the enhancement of thermal conductivity, and the modification of flow channels by incorporating inserts or additional devices.

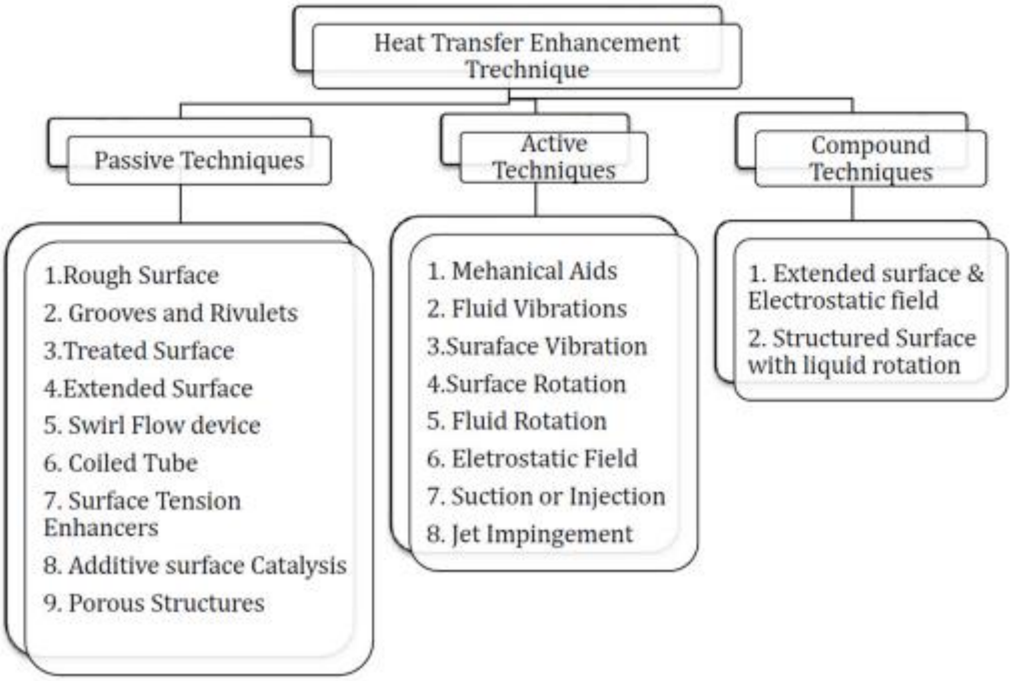

Figure 4. Heat transfer enhancement techniques [3].

### 1.3.1 Passive techniques

Passive methods aim to improve boiling heat transfer by modifying surface properties and structure without relying on external energy input. The main passive methods include surface roughness modification, surface wettability modification, and surface and microstructure expansion. The main advantages of passive methods in improving heat transfer in pool boiling are cost effectiveness, relative simplicity of technology implementation, and stable operation without the need for additional energy input or complex control systems. However, the disadvantages include limited heat transfer enhancement, lack of design flexibility, and, in some cases, the need for refined design and fabrication of complex surface structures, which can increase the complexity and cost of initial design and fabrication.

#### 1.3.1.1 Surface roughness and wettability modification

Surface roughness is a critical factor influencing heat transfer efficiency in pool boiling, along with other variables. A substantial body of research has examined the impact of surface roughness on its interactions with air bubbles. Furthermore, the interplay between surface roughness and wettability represents a considerable interest in contemporary scientific discourse.

Kim et al. [4] examined the influence of surface roughness and contact angle on the heat transfer characteristics and critical heat flux (CHF) of pool boiling on hydrophobic surfaces. The surface roughness values ranged from 0.042 to 1.54 micrometers, with the corresponding static contact angles ranging from 116° to 153°. The results demonstrated

doi:10.6342/NTU202404361

that hydrophobic surfaces exhibited significantly lower CHF values than those observed for hydrophilic surfaces. To illustrate, the smoothest surface, with a roughness average (Ra) of 0.042 µm and a contact angle of 116°, achieved a peak CHF of 67.4 kW/m², which is approximately 16 times higher than the typical CHF values observed on hydrophilic surfaces (around 1100 kW/m²). The study concluded that the contact angle primarily influences CHF on hydrophobic surfaces, while roughness indirectly influences CHF by altering the contact angle.

As illustrated in **Figure 5** and **Figure 6,** when exposed to low heat flow densities (5 kW/m²), surfaces with relatively even topography (roughness ranging from 0.042 to 0.113 µm) exhibit diminished pool boiling heat transfer coefficients (HTC). However, the smoother surfaces' heat transfer coefficient (HTC) gradually increases as the heat flux rises until it reaches its peak value. This phenomenon is attributable to the fact that smoother surfaces exhibit a higher density of nucleation sites at lower heat flux, which reduces the number of bubbles forming at 5 kW/m². Nevertheless, as the heat flux rises to 20 kW/m² and 40 kW/m², a notable surge in bubble formation is observed. However, when subjected to higher heat flow densities of approximately 40 kW/m², bubbles begin to spread across a considerable portion of the surface, exhibiting a phenomenon analogous to that observed on uneven surfaces. This results in a reduction in the Heat Transfer Coefficient (HTC). Surfaces exhibiting moderate roughness levels (approximately 0.112 to 0.113 µm) exhibit peaks in HTC within the heat flow density range of 30 kW/m² to 40 kW/m². In contrast, on the smoothest surface (roughness approximately 0.042 to 0.052 µm), it was observed that a delay in achieving the maximum boiling heat transfer coefficient (HTC) occurred at a heat flux of 45 kW/m². As the heat flux approaches 60 kW/m², a transition to membrane boiling is observed on smoother surfaces.

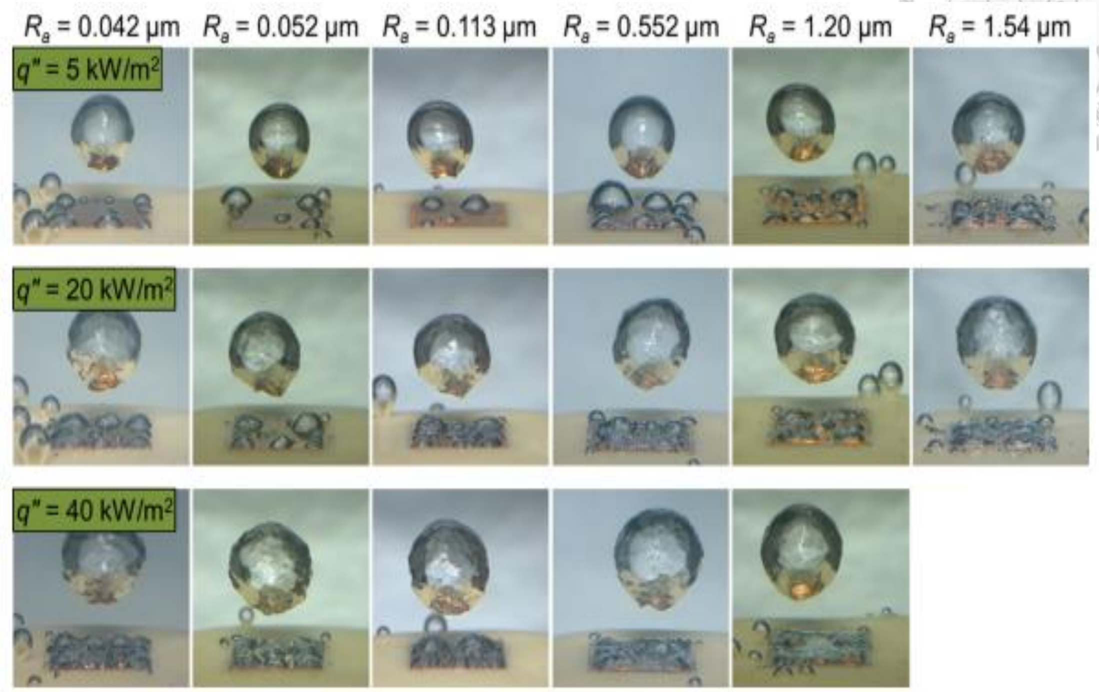

Figure 5. Visualization of Bubble Formation and Departure in Nucleate and Transitional Boiling [4].

doi:10.6342/NTU202404361

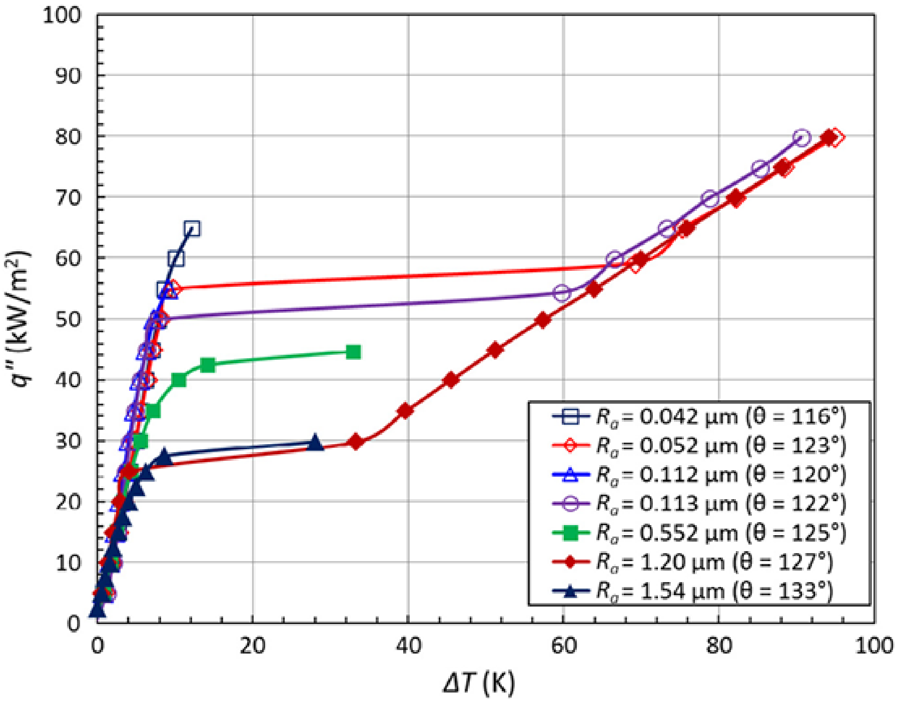

Figure 6. Boiling curves Across the range from nucleate boiling to film boiling of three test surfaces[4].

In an experimental investigation, Hai Trieu Phan et al. [5] studied the impact of surface wettability on the transfer of heat during nucleate boiling. A theoretical framework was introduced to clarify the relationship between surface-wetting properties and heat transfer during nucleate boiling. By employing a nanocoating technique, the contact angle of water was modified from 20° to 110° by altering the topology and chemical composition of the nanoscale surface. It was demonstrated that for hydrophilic (wetted) surfaces, more excellent surface wettability resulted in an increase in the detachment radius of vapor bubbles and a concomitant decrease in the frequency of bubble emission. Moreover, on hydrophobic (non-wetting) surfaces, the degree of superheating required for initial bubble growth was lower. However, bubbles in contact with hydrophobic surfaces could not separate from the surface, and their radius of curvature increased with time. With increased heat flux, bubbles spread across the surface and coalesce with bubbles formed elsewhere, resulting in large areas of the surface being covered with vapor. The best heat transfer coefficient was found on surfaces where the water contact angle is approximately 0° or 90°.

### 1.3.1.2 Surface and microstructure expansion

Huaqiang Chu et al.[6] investigated the influence of surface structural modifications on the transfer of heat during boiling in pools at both macro- and micro-scales. Their study elucidated the distinct roles of macro- and micro-structures in eliminating boiling hysteresis and enhancing boiling heat transfer performance. The techniques of micro-scale enhancement for heat transfer in pool boiling involve various methods such as micro-fins, open micro-channels, micro-porous surfaces, micro-channels with micro-porous surfaces, and slots. The improvement in heat transfer performance is primarily attributed to the increased nucleation density facilitated by these microstructures. Additionally, the CHF is improved to a certain extent. However, it is noteworthy that channel structures with re-entrant cavities can enhance the CHF by separating the vapor and liquid paths. The study of pool boiling bubble dynamics on different surface structures has revealed that the detachment diameters of bubbles on various surface structures exhibit disparate trends when subjected to a specific heat flux. The presence of fins and micro channels significantly impacts bubble kinetics when heat flow density is increased compared to smooth planar surfaces. In the region of low heat flow density or low wall superheat, changes in heat flow density and wall superheat have a more pronounced effect on bubble detachment diameter and frequency. Microstructures effectively enhance the critical heat flux (CHF) due to augmented heat transfer area and capillary suction compared to smooth surfaces. Furthermore, by effectively differentiating between the replenishment liquid path and the vapor detachment path, the

doi:10.6342/NTU202404361

liquid supply rate near the CHF surface region can be augmented, which further optimizes the CHF.

As shown in **Figure 7** and **Figure 8,** Si hui Hong et al. [7] utilized electrodeposition techniques to fabricate metal surfaces featuring three-dimensional $Cu_2O$ crystals with a cubic structure and nanostructures resembling dendrites of copper, with contact angles measuring 127° and 139° for each. These changes reduced the avoided superheat from the original 15.3 K to 4.4 K and 2.9 K. They also observed significant improvements in the maximum heat transfer coefficients, with improvements of 311.4% and 389.2%, respectively. A comparative analysis of these studies underscores the significant impact of nanocavity configurations on bubble dynamics and mechanisms of heat transfer. Deep nano cavities with interconnected dendritic patterns were instrumental in generating significant capillary forces and reducing permeation resistance, thereby facilitating efficient boiling heat transfer. The elongated bubbles generated by these structures effectively inhibit the coalescence of bubbles and delay the formation of local vapor films, thereby mitigating the reduction in heat transfer efficiency that occurs under high heat flux conditions.

doi:10.6342/NTU202404361

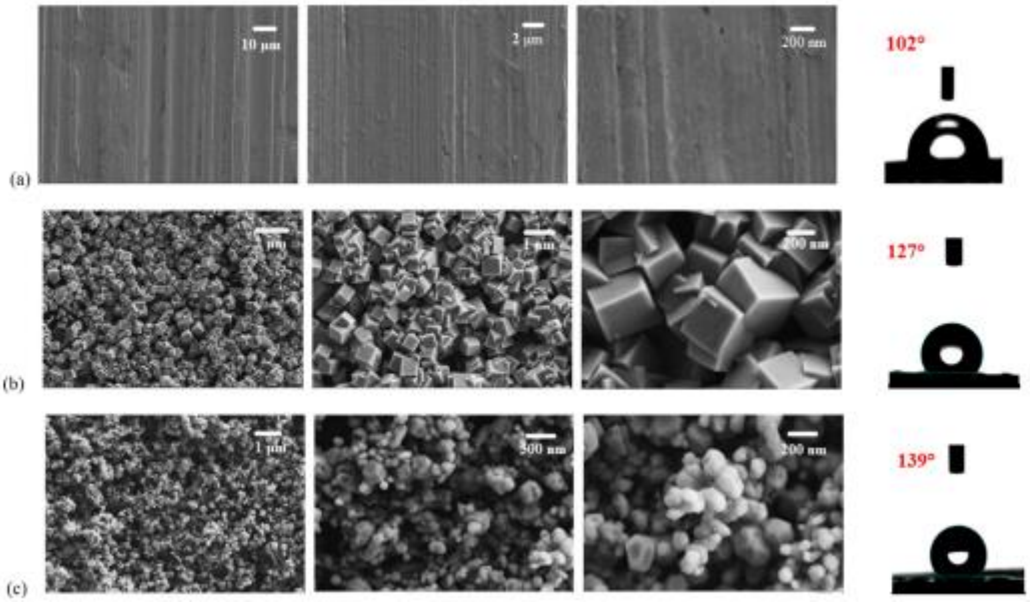

Figure 7. SEM images of (a) flat surface, (b) deposition of cubic $Cu_2O$ crystals on the anodic surface, and (c) deposition of dendritic copper branches on the cathodic surface, along with the respective static contact angles (CAs) of deionized water on each surface.

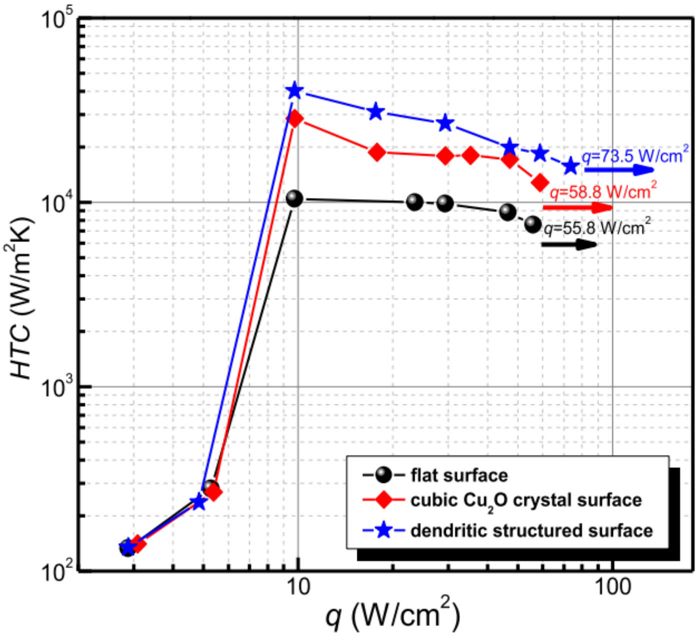

Figure 8. HTCs of different surfaces

The surface modification technique involving nanostructures led to a notable enhancement in boiling heat transfer performance. This was demonstrated by a decrease in the initial temperature overshoot during boiling and a significant enhancement in both the HTC and CHF. Nevertheless, there are still potential risks associated with this approach, including the high cost of surface modification, increased complexity, and potential reliability issues.

## 1.3.2 Active techniques

Active methods facilitate heat transfer during boiling by introducing an external energy source or regulating the process. The principal active methods include ultrasonic enhancement, magnetic field enhancement, electrohydrodynamic methods, mechanical vibration, electrolytic enhancement, and microfluidic and nanochannel flow. The principal advantages of active methods in pool boiling heat transfer enhancement are that they can markedly enhance both the efficiency of heat transfer and the CHF while exhibiting robust tunability to optimize heat transfer in real-time. However, these methods also result in increased energy consumption and system complexity. They may necessitate complex control equipment and sophisticated mechanical or electrical components, which in turn raise initial investment and maintenance costs.

### 1.3.2.1 Vibration-induced effect

Milad Boroumand Ghahnaviyeh et al.[8] investigated the impact of mechanical vibration on the pool boiling HTC of DI water and nanofluid on a copper surface. As shown in **Figure 9** and **Figure 10**, The research yielded substantial evidence of improvements in heat transfer efficiency. Specifically, the researchers found that applying mechanical vibration at an optimal concentration of 0.1 vol% and a frequency of 33 Hz resulted in a remarkable increase of 87.26% in the boiling HTC. Additionally, the study

doi:10.6342/NTU202404361

demonstrated that mechanical vibration reduced the bubble diameter upon detachment from the surface, indicative of enhanced buoyancy forces and reduced surface tension effects. These findings underscore the significant role of mechanical vibration in enhancing heat transfer processes of pool boiling.

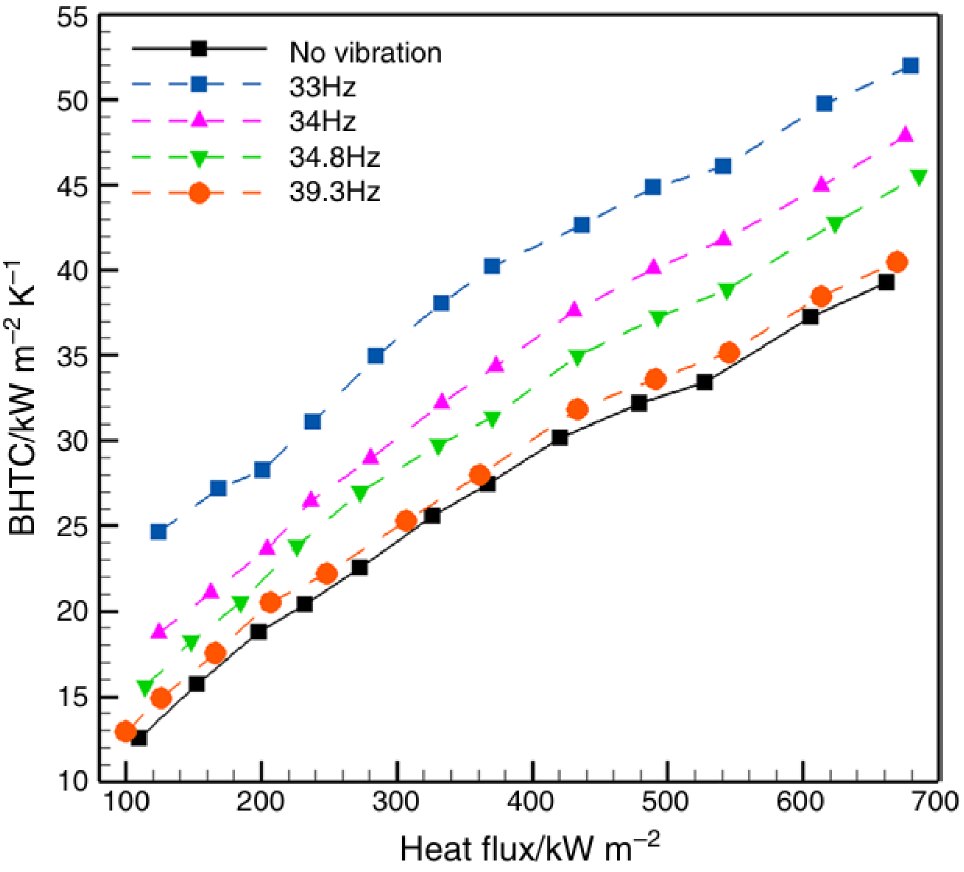

Figure 9. Boiling HTCs in terms of heat flux of DI water for different vibrational frequencies[8].

doi:10.6342/NTU202404361

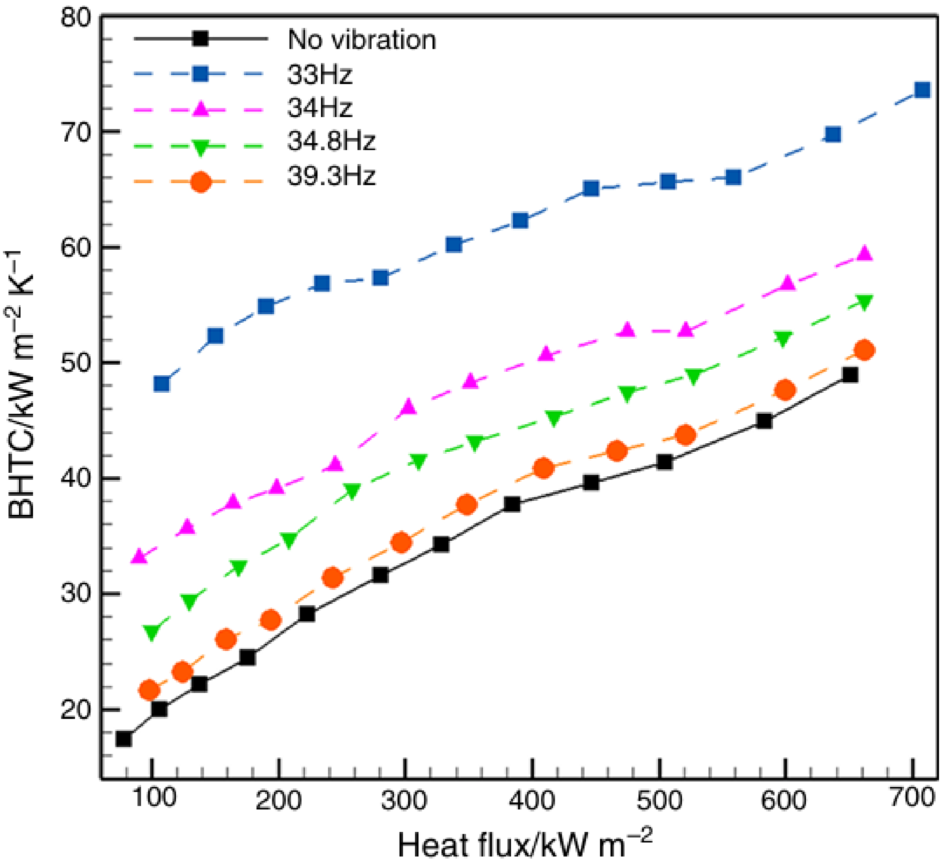

Figure 10. Boiling HTCs in terms of heat flux of nanofluid for different vibrational frequencies[8].

The study of Sathyabhama Alangar's research[9] has demonstrated that introducing vertical vibrations by an external excitation can significantly enhance the boiling heat transfer in a nuclear state pool. In the experiments(as shown in **Figure 11.**), vertical vibrations were applied to a circular copper test surface using a vibration exciter in the frequency range of 0-25 Hz and vibration amplitude in the 0-5 mm range. The results demonstrate that the surface subjected to external excitation boils at a lower superheat and exhibits a significantly reduced slope of the boiling curve despite maintaining the

doi:10.6342/NTU202404361

same heat flow density. Higher frequencies and amplitudes of vibration are observed to enhance heat transfer. Furthermore, some frequency and vibration amplitude combinations even result in doubling the HTC. The experimental results demonstrate that external excitation enhances boiling heat transfer, as shown in **Figure 12,** with the effect being dependent on the intensity of the excitation. The impact of vibration is notably pronounced at lower heat flux levels. Furthermore, it was shown that as the intensity of vibration increased. Additionally, the rate of heat flux removed from the surface at a given temperature also increased. This improvement in heat transfer is predominantly ascribed to alterations in the characteristics of the bubbles.

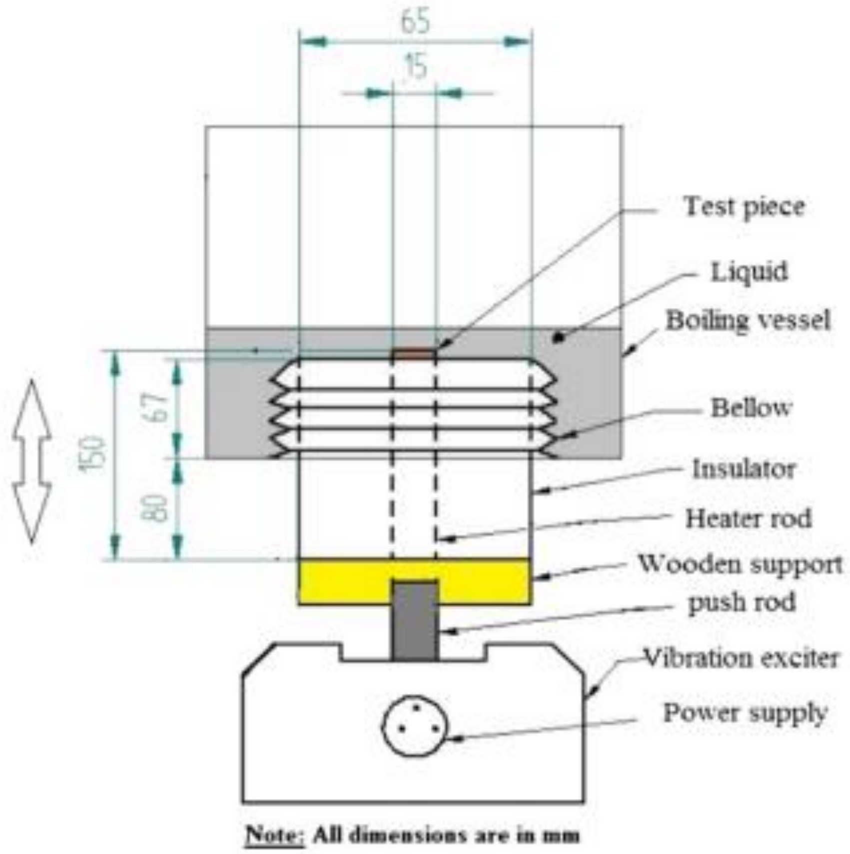

Figure 11. Vibration arrangement.

doi:10.6342/NTU202404361

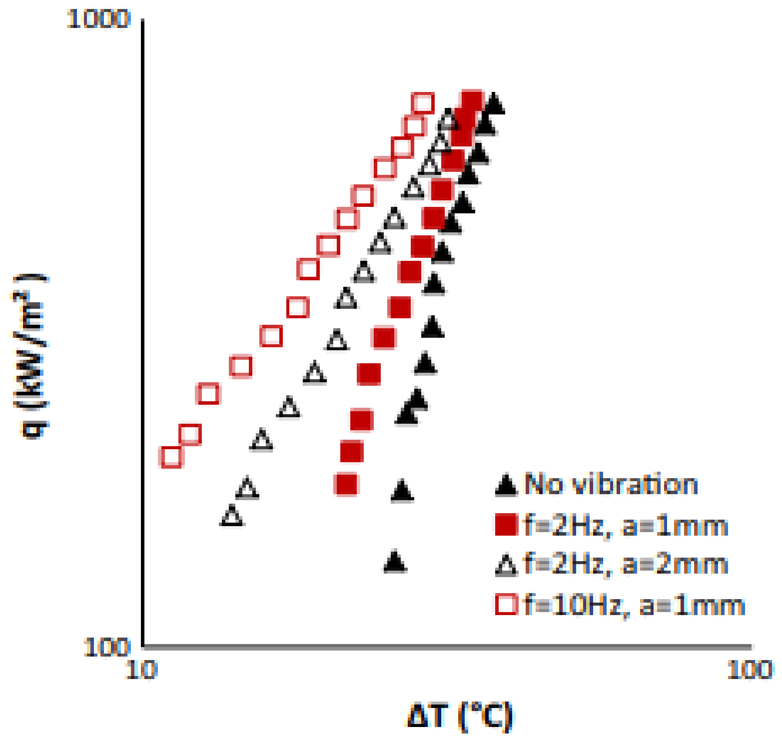

Figure 12. boiling curves of different frequencies and amplitudes of vibration

Vibration or ultrasonic methods of promoting pool boiling while effectively improving heat transfer efficiency present several potential cost, energy consumption, and equipment stability challenges. Operation requires precise control of frequency and amplitude to achieve optimum results. In addition, high-frequency vibration can cause fatigue or damage to equipment and materials, affecting lifetime. Therefore, although these methods offer significant advantages under certain conditions, a combination of technical limitations and cost-effectiveness must be considered in practical applications.

## 1.3.2.2 Electric field control

Using electric fields and electrolytic effects to facilitate heat transfer in pool boiling represents a novel approach that has emerged in recent years. The principal objective of

doi:10.6342/NTU202404361

this method is to employ electrolysis or electric fields to regulate the kinetic properties of bubbles.

The effect of electrolytically activated bubble nucleation on saturated boiling heat transfer was investigated by Tanaka et al. [10]. The research aimed to investigate the influence of electrolytically activated bubble formation on heat transfer during saturated boiling. This study employed a copper surface as the cathode in water electrolysis experiments and the copper was also set as the heat source. The hydrogen bubbles generated through electrolysis on the heated surface were utilized as nuclei for boiling bubbles, thereby enhancing the density of nucleation sites. The boiling curves are presented in **Figure 13.** As the electrolysis current increases, the superheat temperature of the wall decreases. This is demonstrated in **Figure 14,** which also shows that the HTC is higher in the region of the low heat flux. The generation of hydrogen bubbles through the process of electrolysis has a notable impact on the primary mechanism of heat transfer at low heat fluxes. This effect is manifested in a considerable enhancement of the heat transfer coefficient.

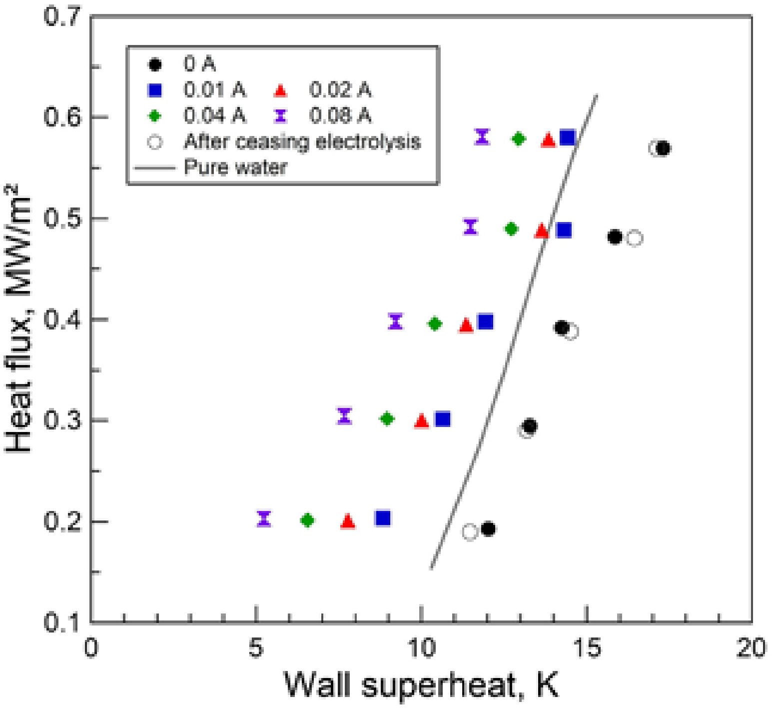

Figure 13. Boiling curves in different electrolytic current, with the current of 0A,0.01A,0.02A,0.04A,and 0.08A[10].

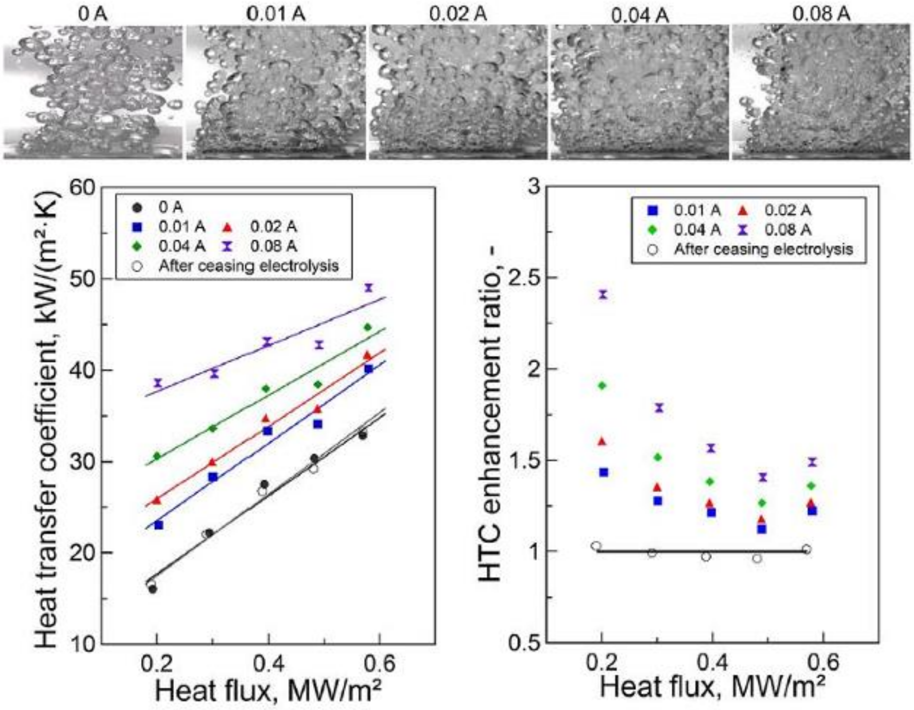

Figure 14. Pool boiling HTCs and HTC enhancements of different input currents[10].

doi:10.6342/NTU202404361

Cao et al. [11]explored the boiling performance of electrolyte solutions and applied electric fields. The researchers demonstrated that the process of bubble nucleation could be manipulated, indicating that bubbles could be activated or inhibited in order to regulate the performance of boiling. The experimental setup is shown in Figure 16; it is similar to that described by Tanaka et al. [21], wherein the working fluid is substituted with charged surfactants, and electric fields are alternated between -2V and -0.1V.**Figure 15. (a)** appears nearly identical, indicating that the electrolytic effects are minimal even with the application of electric fields. Consequently, the electrolytic effects observed in this study were negligible. **Figure 15. (c) and (d)** illustrate the boiling curves of surfactants, including Sodium Dodecyl Sulfate (SDS) and Dodecyltrimethylammonium Bromide(DTAB). The charged SDS and positively charged DTAB solutions may be influenced by the applied electric field. Due to the hydrophobic nature of dissociated ions in surfactants, they can alter surface wettability. A potential of -2V was applied, which resulted in the repulsion of SDS ions from the surface due to electrostatic attraction and repulsion. Consequently, the boiling curve shifts to the right due to a reduction in surface hydrophobicity. Conversely, when the potential value is maintained, The adsorption of DTAB ions onto the surface results in a shift of the boiling curve to the left, which is attributed to the surface becoming more hydrophobic. This illustrates the schematic of adjustable bubble nucleation, as shown in **Figure 15**. It demonstrates how bubbles can appear or disappear alternately by applying an electric field. Overall, the opening and closing of bubbles by adjusting the electrical potential have been demonstrated to enhance the heat transfer properties of boiling. Concurrently, electrolysis has been shown to activate the nucleation sites of bubbles. These electrical field techniques demonstrate potential for future boiling applications.

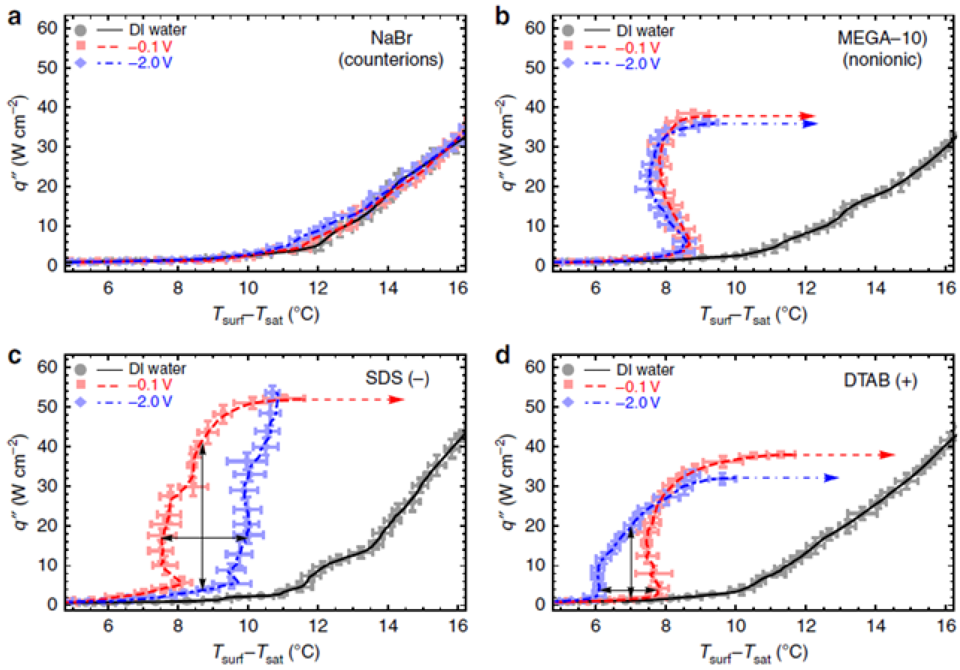

Figure 15. Pool boiling curves of (a) NaBr (b) MEGA-10 (c) SDS (d) DTAB. Black lines represent plain DI water, red lines represent input potential of -0.1V and blue lines represent input potential of -2.0V.

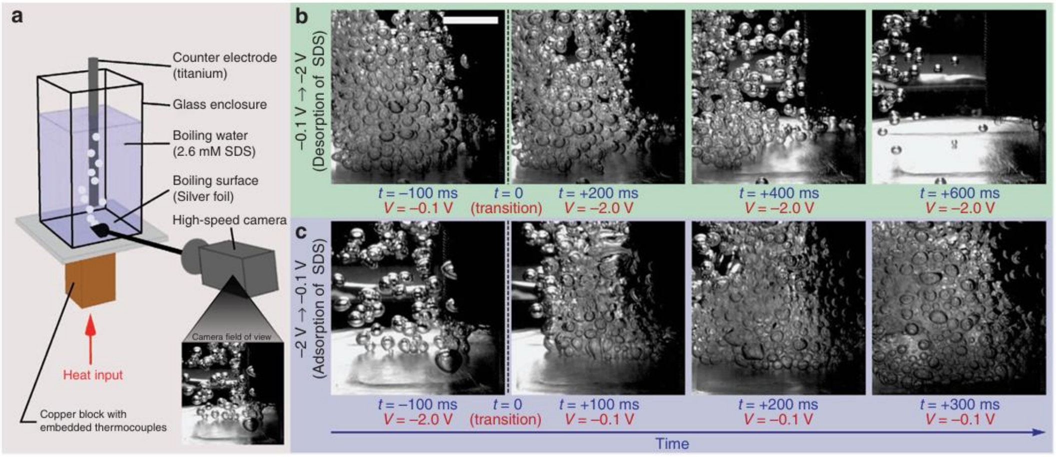

Figure 16. Turning bubbles on and off with a potential switch. (a) The experimental setup involved a 2.6 mM SDS solution (negatively charged), where potential was applied to the silver foil surface with an immersed counter electrode made of titanium (b) Switching from -0.1V to -2.0V ceased the bubble nucleation. (c) Switching from -2.0V to -0.1V promoted the bubble nucleation.

## 1.4 Research purpose and objective

This study examines the impact of heat transfer from horizontally oriented copper tubes during pool boiling, employing the active method of unidirectional square wave current electrolysis. The enhanced heat transfer characteristics of pool boiling on copper tubes have the potential to markedly enhance the performance of tubes undergoing boiling, including coil-and-shell heat exchangers in various industrial applications. The primary motivation and objectives of this study are summarized below.

This study compares the effects of unidirectional square wave pulsed current （USWPC） and direct current（DC） on heat transfer during pool boiling. Specifically, unidirectional square-wave current electrolysis was employed in this study to evaluate the impact of the aforementioned phenomenon on heat transfer during the high heat flux region of pool boiling. This was done under the assumption that excessive bubble aggregation would be prevented by intermittent energization of unidirectional square-wave current. Moreover, using a high speed camera, the study investigated the characteristics of boiling heat transfer performsnce and bubble dynamics under diverse conditions. Furthermore, the study investigated the temperature distribution on the circumference of a horizontally placed circular copper tube.

doi:10.6342/NTU202404361

## 1.5 Thesis structure

Firstly, **Chapter 1** provides a comprehensive overview of the phenomenon of boiling and its principles, along with a literature review of passive and active methods used to enhance pool boiling heat transfer. It also introduces the motivation and objectives of the study and briefly outlines the main concepts underpinning the research. **Chapter 2** elaborates on the theories employed in this study, including wettability, concepts related to contact angles, and the theory of bubble formation through water electrolysis. **Chapter 3** details the experimental methodology, including the preparation of test samples and working fluids, as well as the experimental procedures. An analysis of experimental errors is also included. **Chapter 4** first validates the consistency of the current experimental setup with the Rohsenow's correlation in the context of this study. Subsequently, a comprehensive investigation is undertaken to ascertain the influence of USWPC electrolysis on the augmentation of boiling heat transfer within a horizontal copper tube configuration. Subsequently, the results are elucidated through the utilization of high-speed camera visualization of bubble dynamics. Moreover, an assessment of boiling curves and temperature distributions in the vicinity of the copper tubes is presented to elucidate the efficacy of the boiling process. In the final part of the paper, The conclusions and future perspectives of this study are presented in **Chapter 5.**

doi:10.6342/NTU202404361

# Chapter 2 Theory

## 2.1 Surface energy

Surface energy is the energy required to create one unit of surface area[12]. In general, the bonding between atoms within a substance is typically characterized by stability and equilibrium. However, if the bonding between atoms is incomplete, resulting in imbalanced atoms, surface atoms will absorb material on their surface in order to reduce their surface energy. Consequently, these surface atoms exhibit a proclivity to adsorb substances present in their vicinity, thereby reducing their surface energy. This phenomenon frequently results in surfaces with low surface energy, which in turn correlates with poor wetting properties and relatively high contact angles. We can attribute this phenomenon to the weakened interatomic bonds at the surface.

In 1805, Young [13]developed the theory of surface energy to clarify the relationship between adhesion and cohesion forces. Within the context of a solid-liquid interface, When solid-liquid adhesive forces surpass cohesive forces within the liquid, the liquid tends to spread and wet the solid surface. On the contrary, if the cohesive forces within the liquid predominate over the adhesive forces between the solid and the liquid, the liquid adopts a spherical form, with the intention of wetting the surface. **Equation (3)** illustrates the trend of the minimized total surface energy.

$$\int \gamma dA + g\int \rho z dV = minimum \tag{3}$$

where

doi:10.6342/NTU202404361

**$\gamma$** surface energy per unit area[$J/m^2$]

**$A$:** the total surface area of fluid[$m^2$]

**$g$:** gravitational acceleration[$m^2$]

**$z$:** height of the fluid[m]

**$V$:** volume of the fluid[$m^3$]

**$\rho$:** density of the fluid[$kg/m^3$]

Since **Equation (3)** is subject to a constant volume constraint. Moreover, we can disregard the gravitational term in **Equation (3)** due to the droplet's characteristic length being significantly shorter than the capillary length. In such instances, the equation simplifies to the following form:

$$\int \gamma \, dA = minimum \tag{4}$$

**Equation (4)** illustrates that the fluid itself will adjust the surface area, that is, adjust the surface shape to minimize the total surface energy. Surface energy has a significant influence on the hydrophobicity of a material. In general, hydrophobicity is stronger when the surface energy is lower, whereas hydrophilicity is stronger when the surface energy is higher. The concepts of wettability and hydrophobicity will be introduced in Section 2.2.

doi:10.6342/NTU202404361

## 2.2 Effect of surface wettability on pool boiling and static contact angle

Surface wettability has been recognized as a crucial factor in pool boiling heat transfer. Wettability is defined as the capacity of a fluid to either spread or adhere to a solid surface in the presence of other immiscible fluids. The extent of wetting is contingent upon the static contact angle, representing the interface between the solid-liquid and liquid-vapor phases. This concept is illustrated in **Figure 17** and **Figure 18.** In other words, a contact angle below 90° indicates that the liquid wets the solid surface, whereas a contact angle exceeding 90° signifies the non-wetting behavior of the liquid.

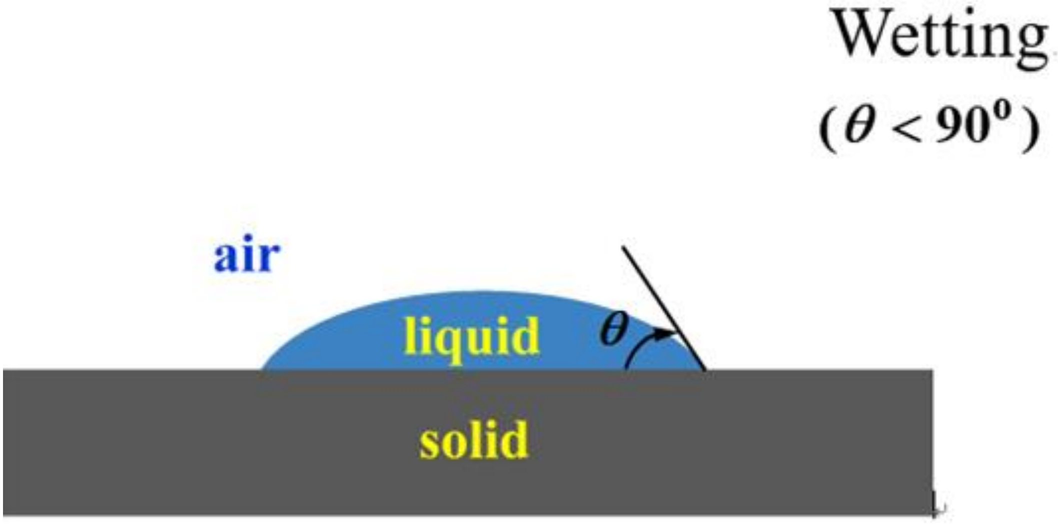

Figure 17. Contact angle effects at the liquid-gas-solid interface-wetting.

doi:10.6342/NTU202404361

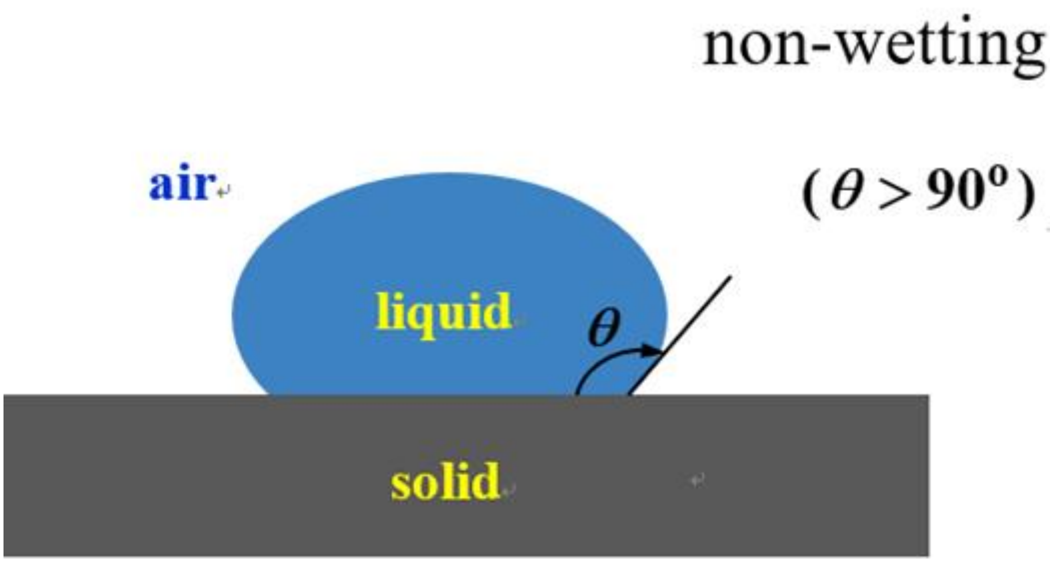

Figure 18. Contact angle effects at the liquid-gas-solid interface-non-wetting.

The contact angle enables the wetting state into four distinct intervals. As illustrated in **Table 1**, a contact angle exceeding 90° signifies a hydrophobic surface, whereas a contact angle less than 90° indicates that the interface is hydrophilic. Furthermore, a hydrophobic surface exhibiting a contact angle between 150° and 180° is classified as superhydrophobic. In contrast, a hydrophilic surface that shows a contact angle ranging from 0° to 10° is called superhydrophobic.

Table 1. Classification of different levels of wettability.

| Wetting state | Schematic | Contact angle range |
|---|---|---|
| Superhydrophilic | 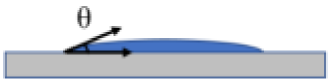 | $0^\circ \leq \theta < 10^\circ$ |
| Hydrophilic | 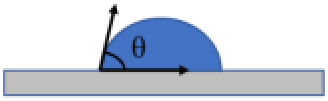 | $10^\circ \leq \theta < 90^\circ$ |
| Hydrophobic | 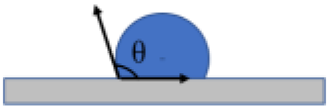 | $90^\circ < \theta \leq 150^\circ$ |
| Superhydrophobic | 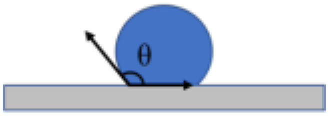 | $150^\circ < \theta \leq 180^\circ$ |

This section summarizes the impact of wettability on the boiling process. The boiling process on hydrophilic surfaces requires a higher degree of superheating to initiate, which reduces heat transfer efficiency. Conversely, the benefit of hydrophilicity is evidenced by a twofold increase in the CHF value compared to that of a conventional metal surface. This phenomenon is exemplified in **Figure 19**[14] .

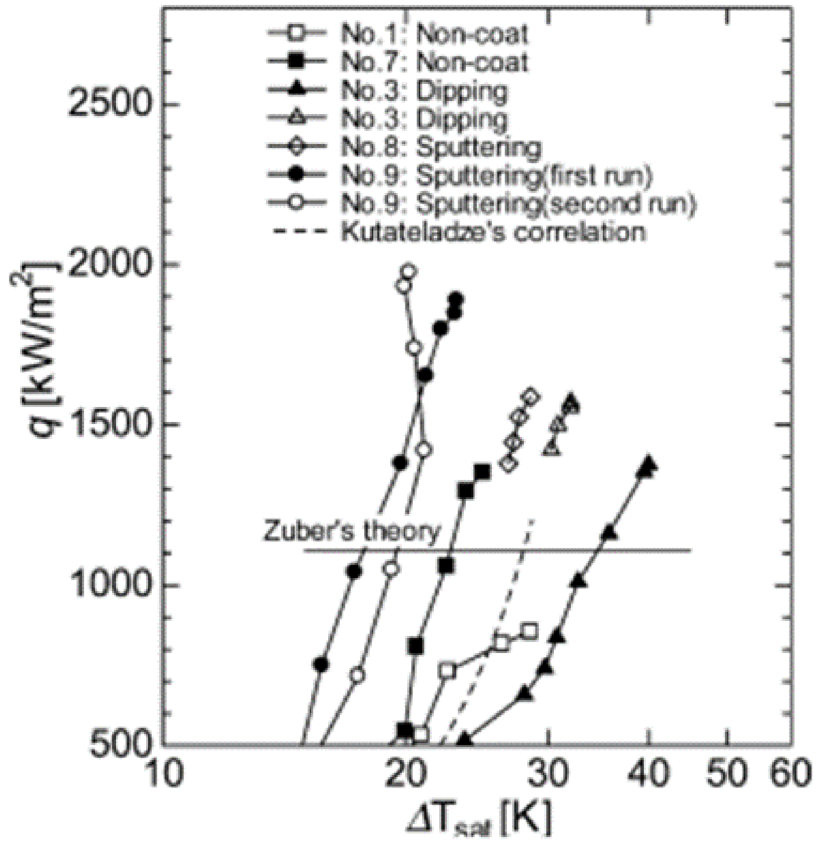

Figure 19. CHF values of TiO2 superhydrophilic surface and copper surface [14].

In contrast, hydrophobicity operates oppositely. Boiling onset on a hydrophobic surface occurs at lower wall superheat[15-17], substantially decreasing the critical heat flux (CHF). While hydrophobicity may seem disadvantageous overall, this is not necessarily the case. It can serve as an optimal nucleation site, thereby enhancing nucleate boiling. We conclude by summarizing the impact of wettability on pool boiling, as shown in **Table 2.**

Table 2. A summary of the effects of wettability on boiling.

| Specific Point in Pool Boiling | Hydrophilic Surface | Hydrophobic Surface |
|---|---|---|
| Onset of boiling | High superheat | Low superheat |
| Critical heat flux (CHF) point | Higher wall temperature | Lower wall temperature |
| Minimum heat flux (MHF) point | Higher wall temperature | Lower wall temperature |

### 2.2.1 Young’s equation.

In a scenario where a drop of liquid is placed on a completely smooth solid surface and reaches a stable equilibrium, the surface's wetting properties can be assessed by determining the surface's contact angle. In the absence of any contact angle（CA）hysteresis on the surface, the CA at the interface of a droplet could be elucidated by applying Young's equation, provided that the surface is not subjected to any external forces.

Young's equation:

$$\gamma_{sl} + \gamma cos\theta = \gamma_{so} \tag{5}$$

where

$\gamma$: surface tension of liquid/gas

$\gamma_{sl}$: interfacial energy of solid and liquid

doi:10.6342/NTU202404361

$\gamma_{so}$: surface energy of solid/gas

$\theta$ : contact angle in equilibrium

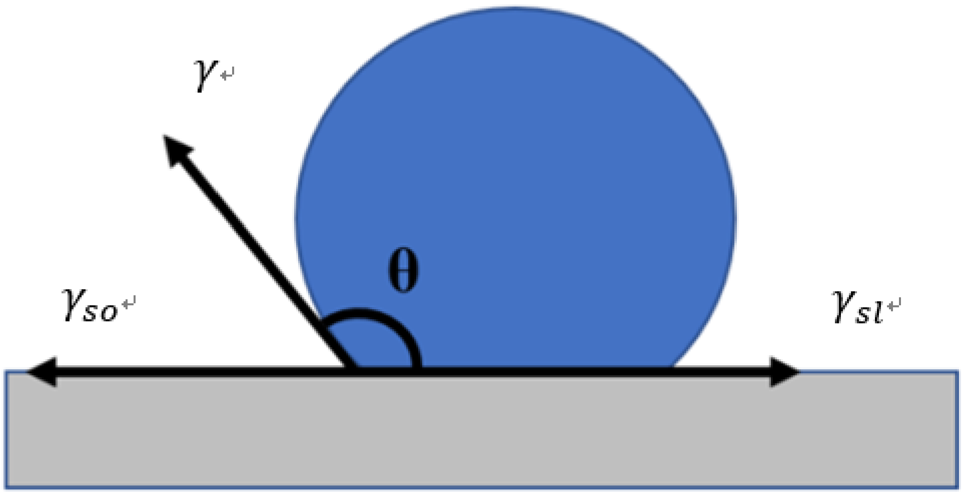

Figure 20. The schematic of Young’s model.

**Figure 20.** displays the schematic of Young’s model. Young's equation provides a theoretical framework for understanding the shape and behavior of droplets resulting from three-phase equilibrium. This equation is limited to rigid, completely flat, chemically inert surfaces with uniform chemical properties.Young's equation could be obtained using basic mathematical techniques within the framework of thermodynamics. **Figure 21.** illustrates a liquid drop on an ideal surface.

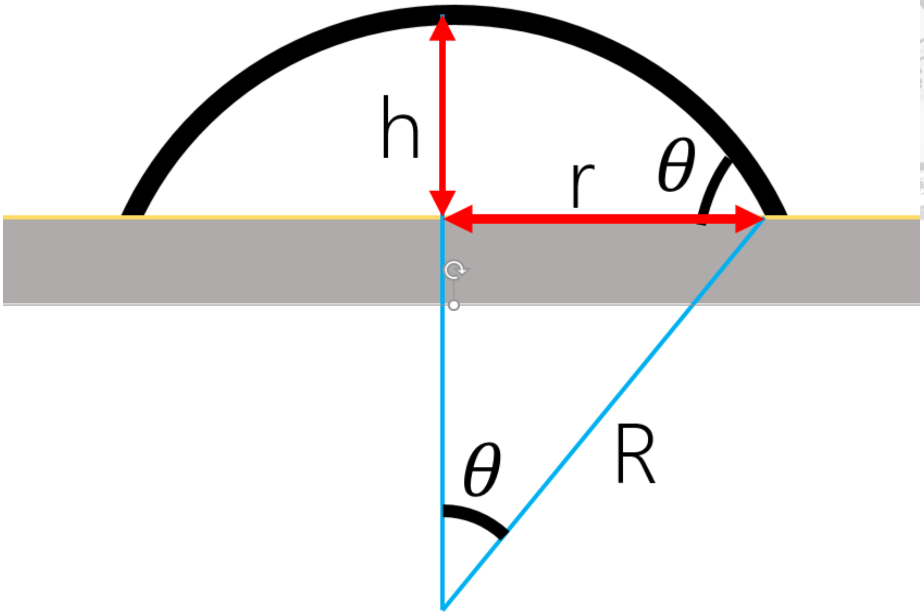

Figure 21. The Cross-section of a liquid drop on an ideal surface.

The volume of a sphere cap can be calculated by the following equations:

$$V = \frac{\pi h}{6}(3r^2 + h^2) \tag{6}$$

$$V = \frac{\pi R^2}{3}(1 - cos\theta)^2(2 + cos\theta) \tag{7}$$

$$A = 2\pi Rh \tag{8}$$

$$A = 2\pi R^2(1 - cos\theta) \tag{9}$$

where ***A*** represents the surface area of the cap

The total energy of the liquid drop can be expressed as:

$$\begin{aligned} E &= \pi r^2 \,(\gamma_{sl} - \gamma_{so}\,) + 2\pi Rh \cdot \gamma \\ &= \pi(Rsin\theta)^2 \,(\gamma_{sl} - \gamma_{so}\,) + 2\pi R^2(1 - cos\theta)\gamma \end{aligned} \tag{10}$$

Suppose *dE* represents the the variation of the energy

$$dE = 2\pi R \cdot (sin^2\theta dR + Rsin\theta cos\theta)$$
$$+\gamma(2(1 - cos\theta)dR + Rsin\theta d\theta) \tag{11}$$

The variation in energy at equilibrium is zero (*dE* = 0). Dividing both sides simultaneously by *dR* is written as:

$$\frac{dE}{dR} = 2\pi R \cdot [(\gamma_{sl} - \gamma_{so}) \cdot \left(sin^2\theta + Rsin\theta cos\theta \frac{d\theta}{dR}\right)$$
$$+\gamma \cdot \left(2(1 - cos\theta) + Rsin\theta \frac{d\theta}{dR})\right] = 0 \tag{12}$$

*dE/dR*=0 means that infinitesimal changes in droplet shape will not cause energy changes. In this case, the droplet's shape satisfies the minimum energy state. Here, to introduce *dθ/dR*, the condition where the droplet maintains a constant volume (dV = 0) is utilized. The volume of the liquid drop can be written as:

$$V = \frac{\pi R^3}{3}(1 - cos\theta)^2(2 + cos\theta) \tag{13}$$

Because of the constant volume condition, we can get $\frac{d\theta}{dR}$

$$\frac{d\theta}{dR} = -\frac{(1-cos\theta)(2+cos\theta)}{Rsin\theta(1+cos\theta)} \tag{14}$$

Substituting Equation(10) into Equation (8) gives

$$(\gamma_{sl} - \gamma_{so}) \cdot (\sin^2\theta\cos\theta(-\frac{(1-\cos\theta)(2+\cos\theta)}{(1+\cos\theta)}))$$
$$+\gamma \cdot \left(2(1 - cos\theta) - \frac{(1 - cos\theta)(2 + cos\theta)}{(1 + cos\theta)}\right) = 0 \tag{15}$$

The rearrangement of the aforementioned equations ultimately yields Young's equation.

$$\gamma_{sl} + \gamma cos\theta = \gamma_{so} \tag{16}$$

## 2.2.2 Wenzel's model

Young's equation is predicated on an idealized condition of liquid on a perfectly flat surface. However, general solid surfaces are not perfectly uniform. Furthermore, minor unevenness in elevation gives rise to varying degrees of surface roughness, affecting the static CA of a liquid droplet on a solid surface .Wenzel[18] has proposed an extension of Young's equation, which describes a theoretical model for the static contact angle of a liquid on a solid surface with roughness. The Wenzel's contact angle model is derived by the following Equation (14):

$$cos\theta^{*} = rcos\theta_{\gamma} \tag{17}$$

where

$\boldsymbol{\theta^*}$: the apparent contact angle

$\boldsymbol{\theta\gamma}$: the equilibrium CA on an ideal solid without roughness from Young's equation

$\boldsymbol{r}$: roughness factor

**Figure 22.** presents the conceptual framework of Wenzel's model, which employs a surface roughness factor to account for the surface roughness of the solid and to calculate the impact of surface roughness on the CA. The surface roughness factor, represented by *r*, which is crucial for further improving the wetting state, regardless of whether the surface is hydrophobic or hydrophilic, is defined as the ratio of the actual area to the projected surface area.

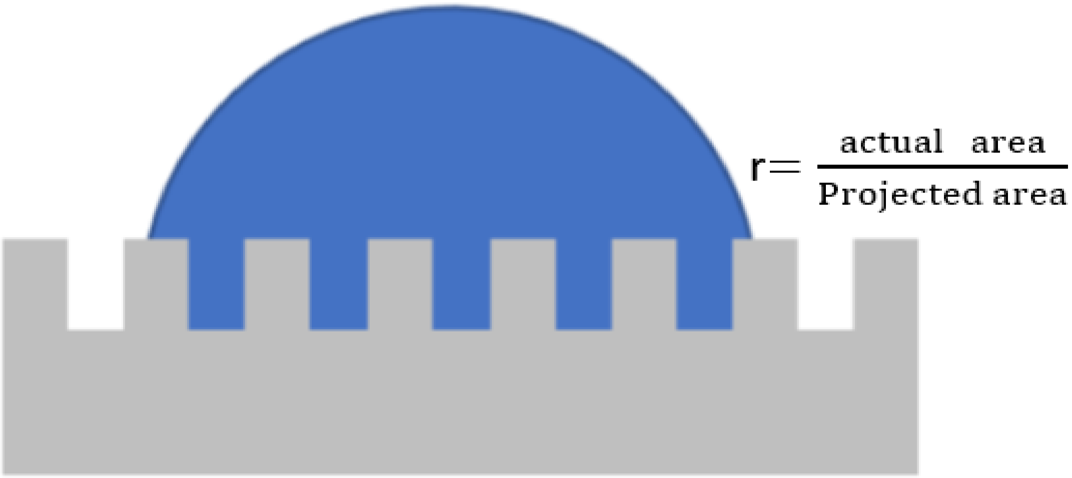

Figure 22. The schematic of Wenzel’s model.

**Figure 23.** depicts a droplet in the Wenzel’s state. The radius of the droplet is represented by aaa. When bbb is zero, the substrate is uniformly rough. It is assumed that the droplet's contact line is situated on the rough area of the substrate.

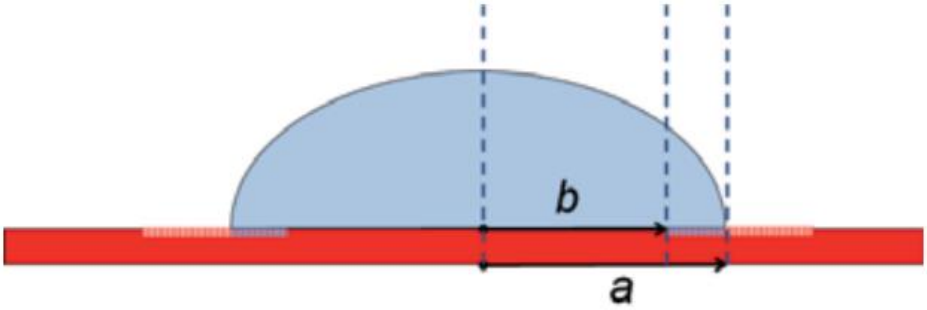

Figure 23. Schematic of the drop in the Wenzel’s model. The radius of the drop is a. The smooth region is b. [19]

As shown in **Figure 23**, the total energy of the system can be written as

$$E = \pi b^2(\gamma_{sl} - \gamma_{so}) + K\pi(a^2 - b^2)(\gamma_{sl} - \gamma_{so}) + A_s\gamma \tag{18}$$

Where

**$K$**: the surface roughness factor.

**$As$**: interfacial area of the gas/liquid

The variation of the energy could be written as

$$dE = d[\pi b^2(\gamma_{sl} - \gamma_{so})] + d[K\pi(a^2 - b^2)(\gamma_{sl} - \gamma_{so})] + d[A_s\gamma] \qquad (19)$$

Rearranging the above equation, it will be written as

$$dE = K\pi(\gamma_{sl} - \gamma_{so})d[a^2] + \gamma d[A_s] \qquad (20)$$

It is important that the constants associated with $\boldsymbol{b^2}$ were excluded due to their fixed nature. Consequently, the internal surface near the contact line does not determine the apparent CA. This contrasts with the preceding Wenzel's model, which considered the internal surface to be a significant influencing factor. The modified Wenzel equation is derived based on **Equation (8)** and the condition of ***dE*** equals zero at equilibrium state and

$$Kcos\theta_\gamma = cos\theta \qquad (21)$$

The revised Wenzel's equation presents a novel interpretation of the surface roughness factor, distinct from its predecessor. In Wenzel's original model, the roughness factor (***r***) was calculated based on the total surface area under the droplet.In contrast, the roughness factor ***K*** is now determined based on the specific local vicinity surrounding the contact line in **Equation (14)**.

doi:10.6342/NTU202404361

### 2.2.3 Cassie-Baxter model

Consider the case of a superhydrophobic surface, where droplets are observed to aggregate into spheres on the surface, with the nanoroughness of the surface structure trapping air within its structure, forming an air cushion that significantly reduces the solid-liquid contact area. Thus, The CA increases, rendering the two previous equations inapplicable. Consequently, Cassie and Baxter [20] propose a set of theoretical models, depicted in the accompanying **Figure 24**. to describe superhydrophobic types of surfaces.

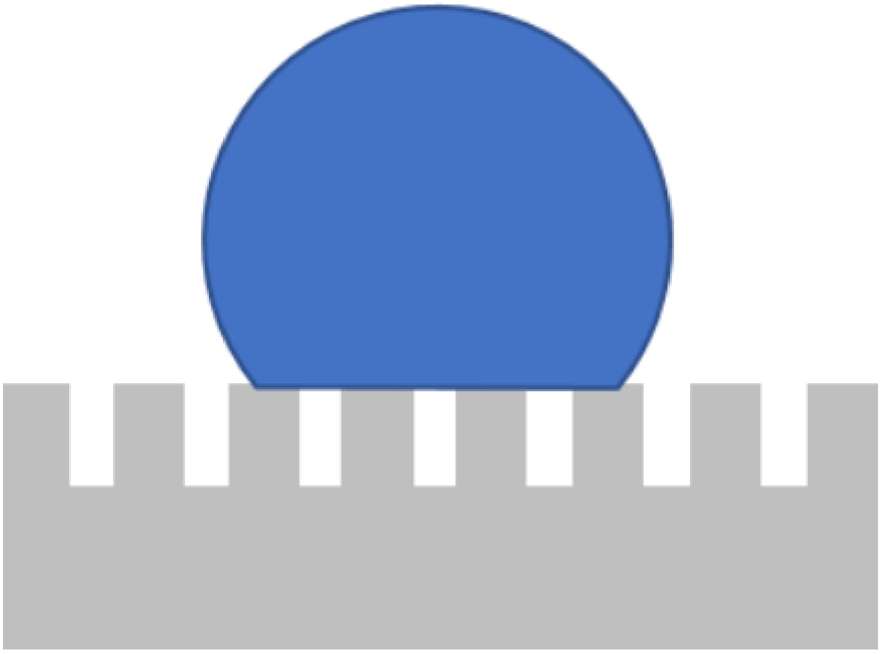

Figure 24. The schematic of the Cassie-Baxter model.

**Figure 25.** illustrates a droplet on a composite substrate consisting of two different ideal surfaces. The area fraction of the red region is labeled as $f_1$, while the yellow region is labeled as $f_2$

doi:10.6342/NTU202404361

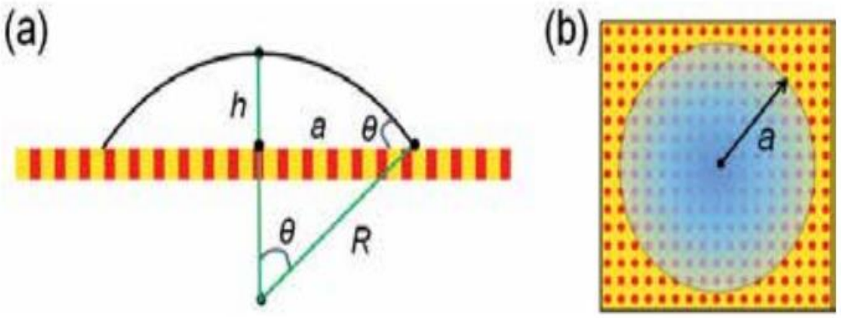

Figure 25. (a) side-view, (b) top-view. of the drop in the Cassie-Baxter state [19].

The system's total energy can be expressed based on the provided figure.

$$E = f_1\pi a^2\left(\gamma_{sl,f_2} - \gamma_{so.f_1}\right) + f_2\pi a^2\left(\gamma_{sl,f_2} - \gamma_{so,f_2}\right) + A_s\gamma \qquad (22)$$

In this context, ***As*** represents the gas/liquid interfacial area. The change in energy can be expressed as

$$dE = C_1 d(R^2 sin^2\theta) + C_2 d\big((1 - cos\theta)\big) \qquad (23)$$

and

$$C_1 = f_1\pi\left(\gamma_{sl,f_1} - \gamma_{so.f_1}\right) + f_2\pi\left(\gamma_{sl,f_2} - \gamma_{so,f_2}\right) \quad C_2 = 2\pi\gamma$$

From $dE=0$ at equilibrium and **Equation(8)**, the modified Cassie-Baxter equation is shown as follows:

$$f_1 cos\theta_1 + f_2 cos\theta_2 = cos\theta \qquad (24)$$

assume that $f_2$ is a fraction representing the contact angle with air and that $\theta_2 = \pi$, we can derive the modified Cassie-Baxter equation from **Equation (17)**. A notable distinction exists between the previous Cassie-Baxter equation and the modified one. The definition of the surface fraction is distinct. In contrast to the previous model, which derived the surface fraction from the total area under the drop, the revised equation (**Equation 17**) specifies that the surface fraction should be obtained from the local region near the contact line. Furthermore, the derivation indicates that the property or state of the internal surface within the triple line does not influence the apparent CA.

## 2.3 Electrolysis

Tanaka[10] demonstrated that the efficiency of boiling heat transfer can be enhanced through the electrolysis of deionized water. The formation of hydrogen bubbles induced by electrolysis on the heated surface acts as nuclei, thereby increasing nucleation sites and promoting the earlier onset of nucleate boiling(ONB). This section will delve into electrolytic principles to support the experimental methodology outlined in **Chapter 3.**

In the nineteenth century, Faraday[21] coined the term "electrolysis" to describe the redox reaction that occurs when an electric current is applied. Electrolysis involves the passage of direct current (DC) through an electrolyte, resulting in oxidation-reduction reactions at distinct anode and cathode electrodes. Before commencing electrolysis, two key considerations must be taken into account:

1. The electrolyte, typically a soluble substance, must be present to furnish free electrons in the solution and facilitate the flow of electric current between the electrodes.

2. Electrodes, another critical element in the electrolysis process, are submerged in the electrolyte solution. They act as conductors, establishing a connection to a power source. This connection enables the direct current to circulate and form a complete circuit, a crucial step in electrolysis. The anions and cations in the electrolyte are attracted to and discharged separately at the respective electrodes.

doi:10.6342/NTU202404361

The electrolysis of deionized (DI) water is significant in enhancing boiling heat transfer performance in this study, as evidenced by the seminal work of William Nicholson and Anthony Carlisle in 1800. Their experiment successfully decomposed water into hydrogen and oxygen through separate electrode reactions. (**Equation (25)& (26)**)

$$\mathrm{H_2O(l)} \rightarrow \mathrm{2H^+} + \mathrm{(aq)} + \frac{1}{2}\mathrm{O_2(g)} + \mathrm{2e^-}\ \text{(anode)} \tag{25}$$

$$\mathrm{2H_2O(l)} + \mathrm{2e^-} \rightarrow \mathrm{2OH^-(aq)} + \mathrm{H_2(g)}\text{(cathode)} \tag{26}$$

In the experimental setup, oxygen was produced at the anode, producing oxidation. Concurrently, hydrogen bubbles were generated at the cathode, a process crucial for improving heat transfer during boiling. The heated surface was set as the boiling experiment cathode sothat it would prevent surface oxidation. The rate of hydrogen bubble generation could be determined using Faraday's law of electrolysis. Michael Faraday[21] discovered two laws of electrolysis in 1834, along with corresponding mathematical formulations. The present study sought to quantify the connection between electrochemical investigations and these foundational laws.

In **Equation (27)**, the first law of electrolysis is stated: the quantity of substances accumulated on the electrodes is directly proportional to the electric charge applied.

$$\boldsymbol{\frac{m}{Q} = Z(m \propto Q)} \tag{27}$$

where

$\boldsymbol{Q}$**:** the electric charge applied

$\boldsymbol{m}$**:** the mass of the elements

$\boldsymbol{Z}$**:** the constant of proportionality (the electro-chemical equivalent of the substance. )

doi:10.6342/NTU202404361

Faraday's second law, as represented by Equation (28), demonstrates that the quantity of elements formed on the electrodes is directly proportional to their chemical equivalent weight.

$$\boldsymbol{m \propto E\left(E = \frac{M}{v}\right)} \tag{28}$$

where

$\boldsymbol{m}$**:** the mass of elements

$\boldsymbol{E}$*:* the equivalent weight

$\boldsymbol{M}$**:** the molar mass

$\boldsymbol{v}$**:** Valence, losing or gaining numbers of electrons.

The integration of Equation(27) and (28) yields Equation (29).

$$\boldsymbol{Z = \frac{m}{Q} = \frac{1}{F}\left(\frac{M}{v}\right) = \frac{E}{F}} \tag{29}$$

where $\boldsymbol{F}$ stands for the Faraday constant. Furthermore, this equation has the potential to be simplified into a more concise form specifically for constant-current electrolysis, as exemplified in **Equation (30)**.

$$\boldsymbol{n = \frac{It}{Fv}} \tag{30}$$

where

$\boldsymbol{n}$**:** the number of moles for the substance

$\boldsymbol{I}$: the constant applied current

$\boldsymbol{t}$: the total time of the current

The hydrogen generation rate in electrolysis was determined by directly applying the summarized formula in **Equation (30)** to the transformed **Equation (31).**

doi:10.6342/NTU202404361

$$\boldsymbol{V_h = f \times vol_m \times \frac{I}{\upsilon F}} \quad (31)$$

Where

$\boldsymbol{V_h}$**:** the volumetric hydrogen generation rate

$\boldsymbol{f}$: the gas evolution efficiency

$\boldsymbol{vol_m}$**:** the molar volume of the gas

Consequently, the activation of electrolytic bubble nucleation can be evaluated through the equations above, thereby enabling the determination of the rate of bubble generation. This provides the foundation for further research into the dynamics of bubbles.

doi:10.6342/NTU202404361

# Chapter 3 Experiment methodology

## 3.1 Experiment setups

The experimental setup structure of this study was categorized into three functional groups: the support unit, the heating and recording unit, and the electrolysis-generating unit, as displayed in **Figure 26.**

Firstly, the supporting unit consisted of a Quartz chamber， a cover, and a copper tube, all horizontally placed, labeled as “L” and “N” in **Figure 26.** The temperature capacity of quartz glass exceeds 100 degrees Celsius, which is the standard boiling point of water at atmospheric pressure. Moreover, quartz glass facilitates convenient observation of bubble dynamics changes on the copper tube's surface. The dimensions of the quartz cavity are 10 centimeters long, 10 centimeters wide, and 15 centimeters high. Positioned above the chamber was a lid, securely fastened to the chamber wall with four screws and four nuts on 4 sides. Next, a rubber seal was inserted between the lid and the chamber wall to prevent leakage of the working fluid through potential gaps. The copper tubes were positioned at the lower center of the chamber and secured by a PEEK holder. Within the chamber, two brackets supported the peek holder, ensuring the horizontal alignment of the copper tubes. The details of the copper tubes and the peek holder will be further elaborated in the heating unit section.

Secondly, the heating unit comprised a copper tube, a heater, a DC power supply, a spherical condenser tube, a condenser, and an auxiliary heater, as depicted in **Figure 27.** The outer diameter of the copper tube measured 23cm, and the inner diameter is 18 mm and the height of the copper tube is 20 mm. On both sides of the copper column（shown in **Figure 28**.）were 16 holes, each with a diameter of 1mm. Eight holes were evenly distributed on either side, and temperature probes were inserted into eight holes on the

doi:10.6342/NTU202404361

left side to monitor temperature variations. On the other side, the inserts were inserted without the temperature probes to fix the copper tube. A cylindrical heater was the primary heat source for the copper tube. Before insertion, the cylindrical heater was evenly coated with a heat-conductive paste to minimize thermal resistance upon contact. The cylindrical heater was powered by a DC power supply unit, as illustrated in **Figure 26**. A spherical condenser tube was connected to the chamber lid to liquefy gas, thereby maintaining the conservation of the working fluid's mass. In the condenser tube, condensate was discharged from the top to the bottom, facilitating more efficient convection as gas rose from the bottom. The water temperature in the condenser was set at 4 degrees Celsius, ensuring that return water remained at the same temperature. This configuration demonstrates that condensation exceeds evaporation capacity, ensuring adequate working fluid conservation. Moreover, since tap water temperature typically remains at 4 degrees Celsius, this design feature is advantageous for future industrial applications. Furthermore, an auxiliary heater connected to a power supply is situated within the chamber. The primary function of the auxiliary heater is to preheat the working fluid up to a saturated temperature before commencing the experiment. Additionally, it maintains the working fluid at saturated temperature throughout the experiment's duration.

The electrolysis unit primarily facilitates the electrolysis of the working fluid during the experimental process. It comprises a signal generator, a Current meter, a Voltage meter, a light-emitting diode, and two electrodes. The chemical equation for the electrolysis of water is as follows:

Anode/positive electrode reaction:

$$\mathrm{H_2O(l) \rightarrow 2H^+(aq) + \frac{1}{2}O_2(g) + 2e^-} \tag{15}$$

Cathode/negative electrode reaction:

$$2H_2O(l) + 2e^- \rightarrow 2OH^-(aq) + H_2(g) \tag{16}$$

Overall reaction:

$$2H_2O \rightarrow 2H_2(g) + O_2(g) \tag{17}$$

A signal generator produces a unidirectional pulsed signal with a period set to 40 seconds. This duration accounts for the time required for the working fluid to undergo electrolysis after energization and the interval necessary for gas bubbles from electrolysis to detach entirely from the copper surface after de-energization. The signal generator operates on a 20-second energization followed by a 20-second power-off cycle, depicting the idealized current versus time diagram. Functionally equivalent to a power supply, the signal generator, in conjunction with a current meter, a light-emitting diode (LED), a working fluid, and two electrodes, forms a circuit loop for the electrolysis of the working fluid. The LED and the working fluid are arranged in series to provide the power source for electrolysis. At the same time, a voltmeter connected in parallel between the two electrodes monitors the current magnitude continuously throughout the experiment. Furthermore, the voltmeter measures and tracks the voltage level across the electrodes. During experimentation, the two electrodes are designated as anode and cathode. The anode, submerged in the working fluid, facilitates oxygen generation, while the cathode, inserted into a copper tube, serves as the point of hydrogen generation. This setup prevents oxidation of the copper, ensuring that only hydrogen is produced on its surface. To rectify the signal generated by the generator and prevent the formation of oxygen bubbles on the copper surface, a light-emitting diode (LED) is incorporated into the circuit. The LED leverages its unidirectional conductivity to control the signal flow. Throughout the experiment, continuous monitoring of ammeter and voltmeter readings ensures alignment with theoretical principles. The LED's illumination and extinguishing indicate the current power status, affirming whether energization is active at any given time.

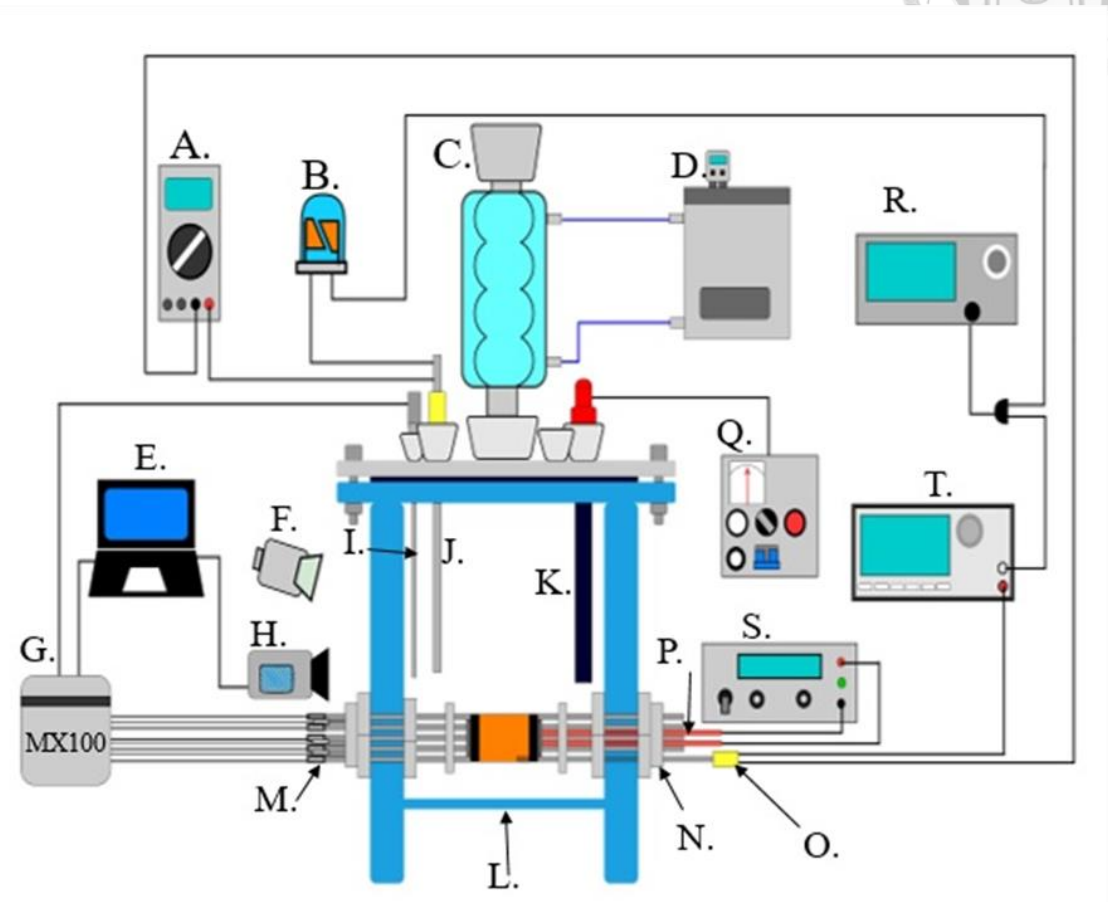

Figure 26. Schematic of the experimental setup.

A. Voltage meter
B. Light-emitting diode
C. Reflux condenser
D. Chiller unit
E. Computer
F. Light source
G. Data logger
H. High-speed camera
I. T-type pool thermocouple
J. Stainlessness electrode
K. Auxiliary heater
L. Quartz chamber
M.T-type thermocouples
N. Peek holder
O. Stainlessness electrode
P. Cartridge heater
Q. Autotransformer
R. Signal generator(for electrodes)
S. DC power supply (for heating)
T. Current meter

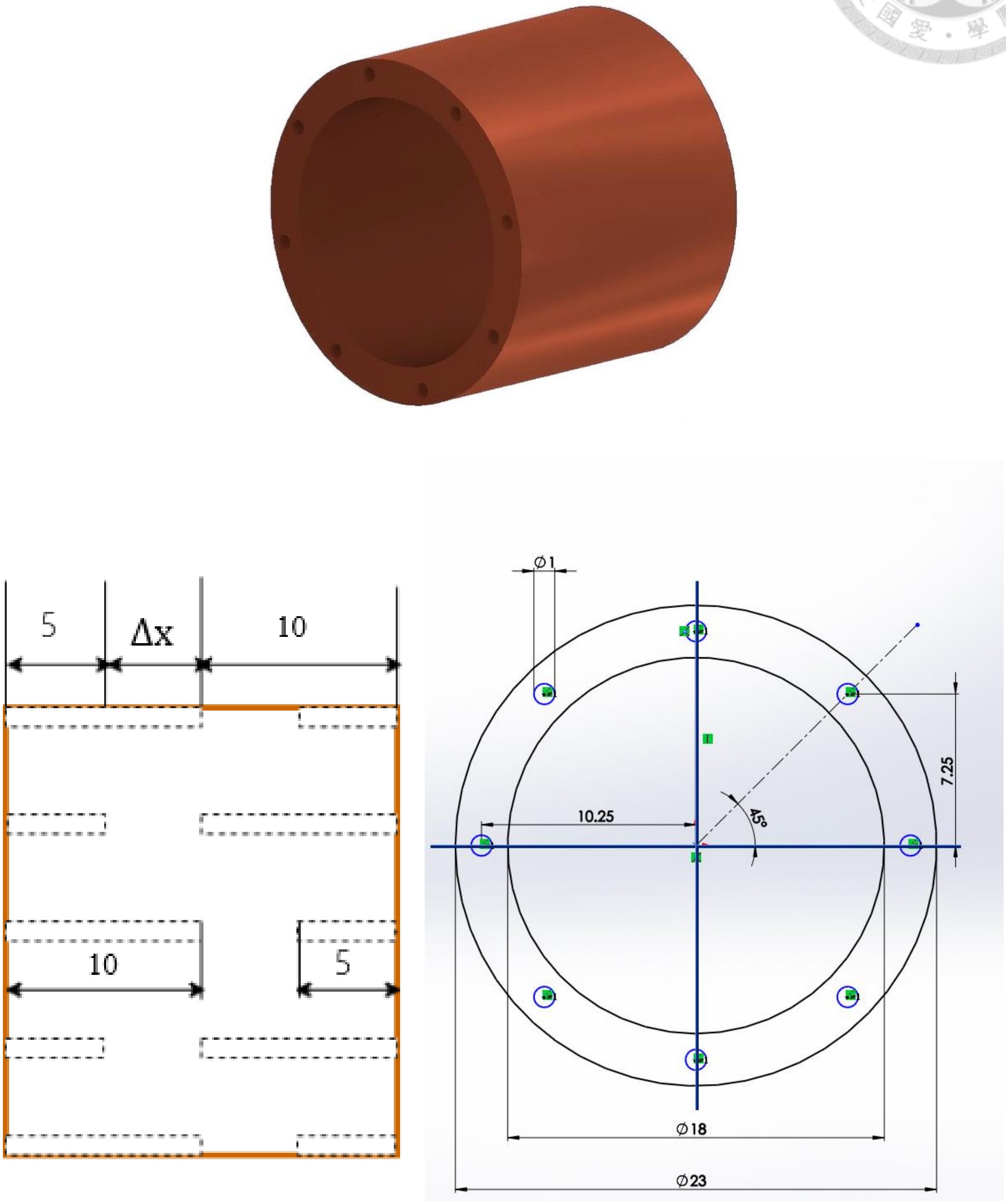

Figure 27. Design of the experimental test section.

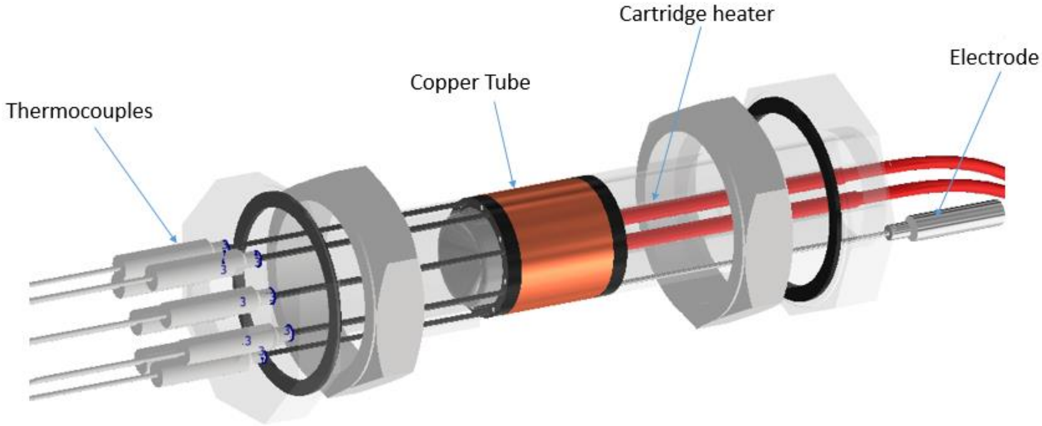

Figure 28. Schematic of the experimental setup.

## 3.2 Preparation of copper tube

The outer diameter of the copper tubes utilized in this study was 23 mm, with a length of 20 mm. In the preparation stage, the outer surface of the copper tubes was sanded with 2000-gauge sandpaper. The purpose of sanding with sandpaper was to remove the oxidized layer on the surface of the copper tubes. Once the surface was sanded until smooth, it was cleaned with acetone. The copper tubes were then cleaned with water to remove residual particles from the surface. The water was subsequently dried using an air compressor. Finally, the tubes were placed in a preheated oven at 150 degrees Celsius for 10 minutes.

**Figure 29.** illustrates the surface roughness of the treated surface, which was quantified by a laser scanning confocal microscope (NTUME Precision Metrology Lab, Japan, Controller: The VK-X1000 measuring head was utilized in conjunction with the VK-X1100 measuring head (**Figure 30.**).And the surface roughness was Ra=1.020 microns after the surface treatment.

| 150X | Polished Copper tube | Polished Copper plane |
|---|---|---|
| 3D | 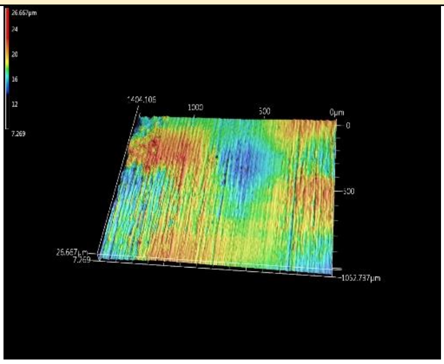 | 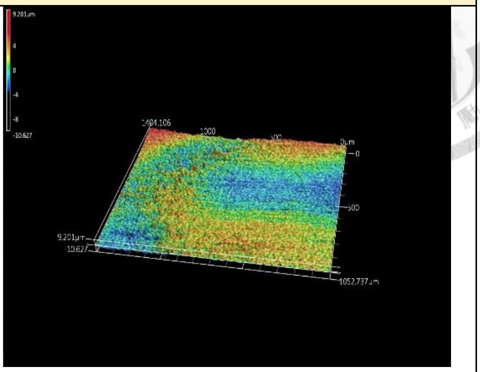 |
| Confocal | 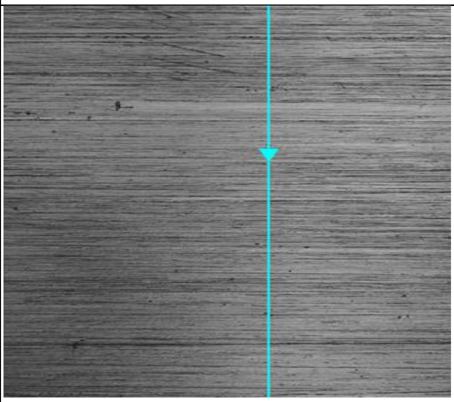 | 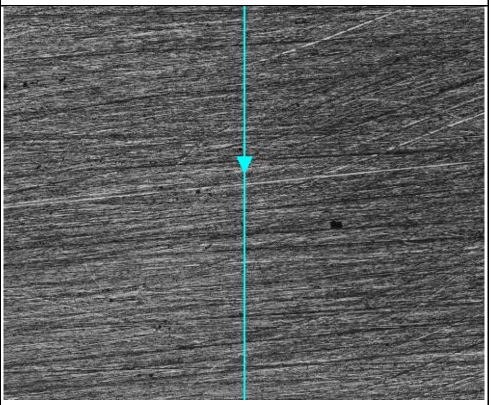 |
| Profile | 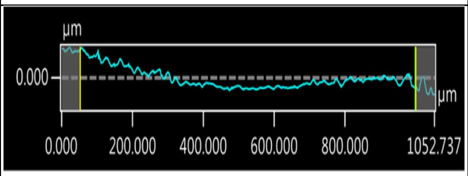 | 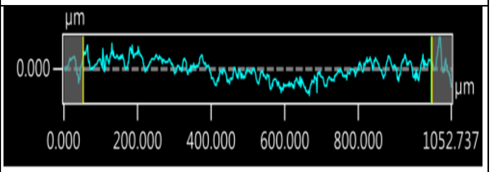 |
| Surface Roughness | 1.020µm | 1.381µm |

Figure 29. Surface profile of the polished copper measured by the laser confocal microscope.

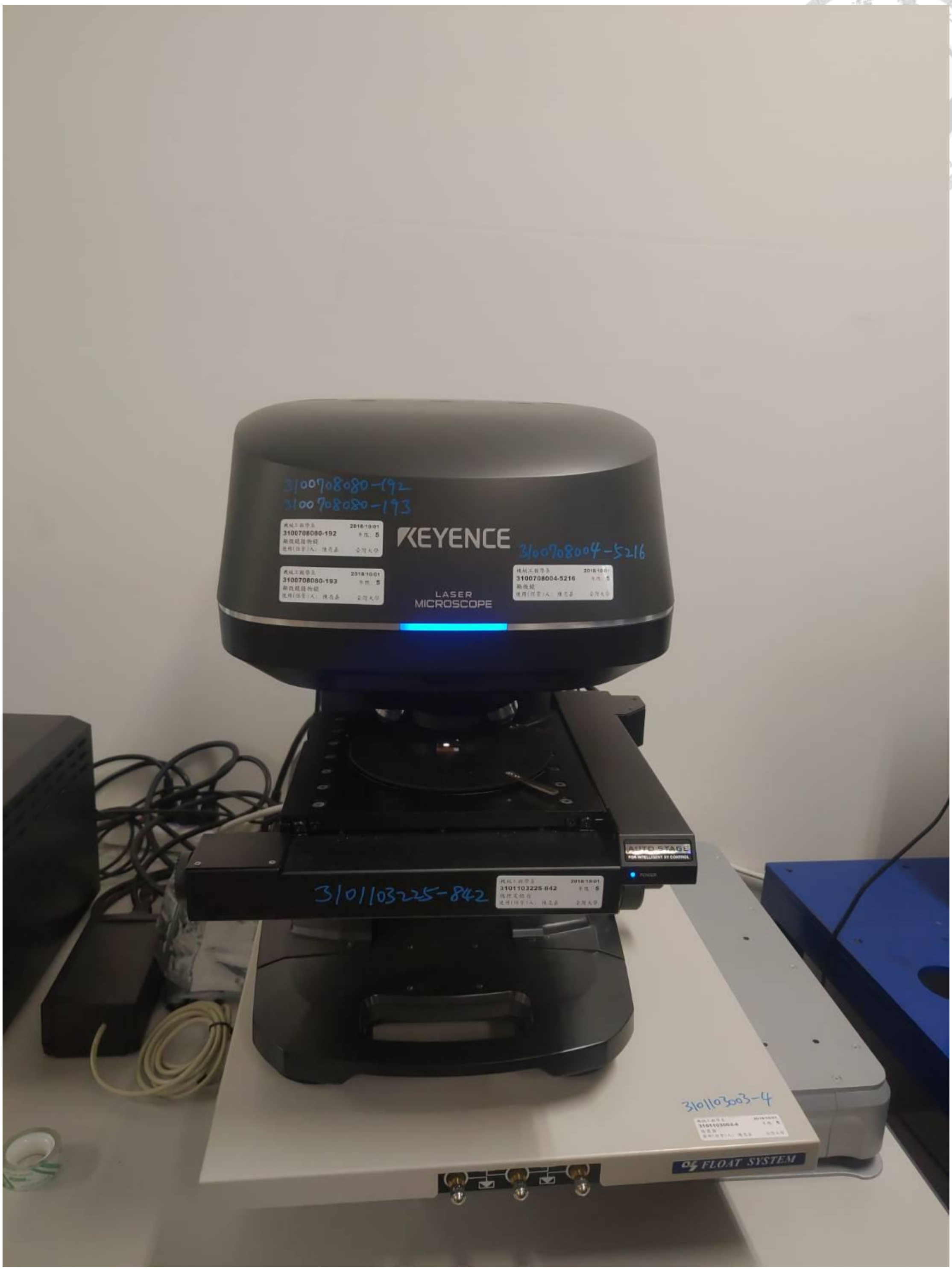

Figure 30.Laser scanning confocal microscope.

doi:10.6342/NTU202404361

## 3.3 Working fluid preparation

This study utilized sodium carbonate solution($Na_2CO_3$) as the working fluid, with 3 g of sodium carbonate dissolved in 1 liter of deionized water during the experimental configuration. Deionized water underwent two boiling cycles for degassing. The sodium carbonate solution was employed to investigate the impact of unidirectional square wave pulsed current electrolysis on the heat transfer of pool boiling.

**Figure 32.** illustrates the pool boiling curves of sodium carbonate solution and deionized water on a copper tube. The contact angle was measured using the contact angle goniometer in **Figure 31**. The results shown in **Table 3.** demonstrate that using sodium carbonate solution as the working fluid did not alter the observed trend in the pool boiling curves.

Table 3. Measurement results of the contact angle between water and sodium carbonate solution

| **Working fluid** | **DI water** | **$Na_2CO_3$ Water Solution** |
|---|---|---|
| **Image of water drops on a copper plate** | 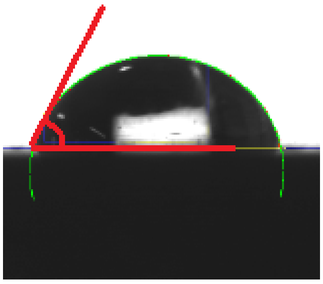 | 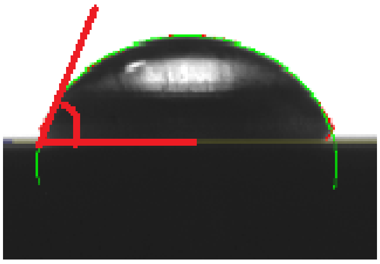 |
| **Contact angle** | **75.79°** | **75.67°** |

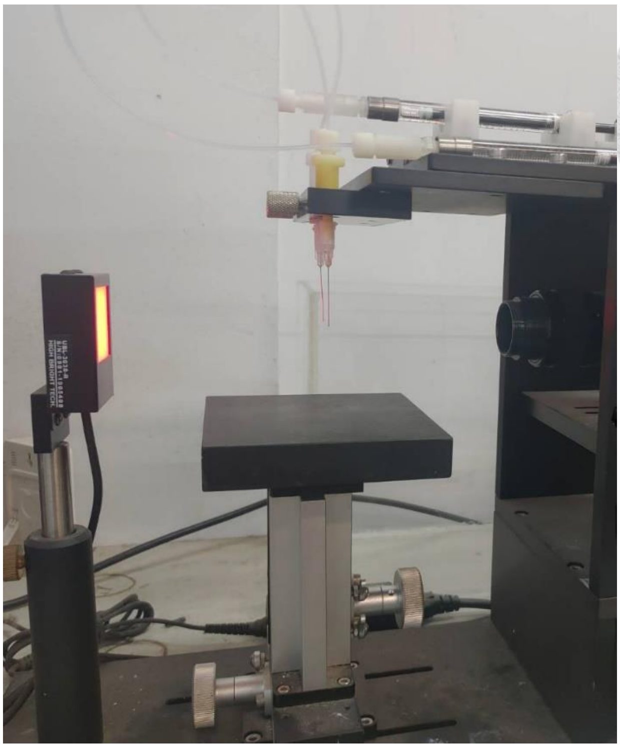

Figure 31.Contact angle goniometer.

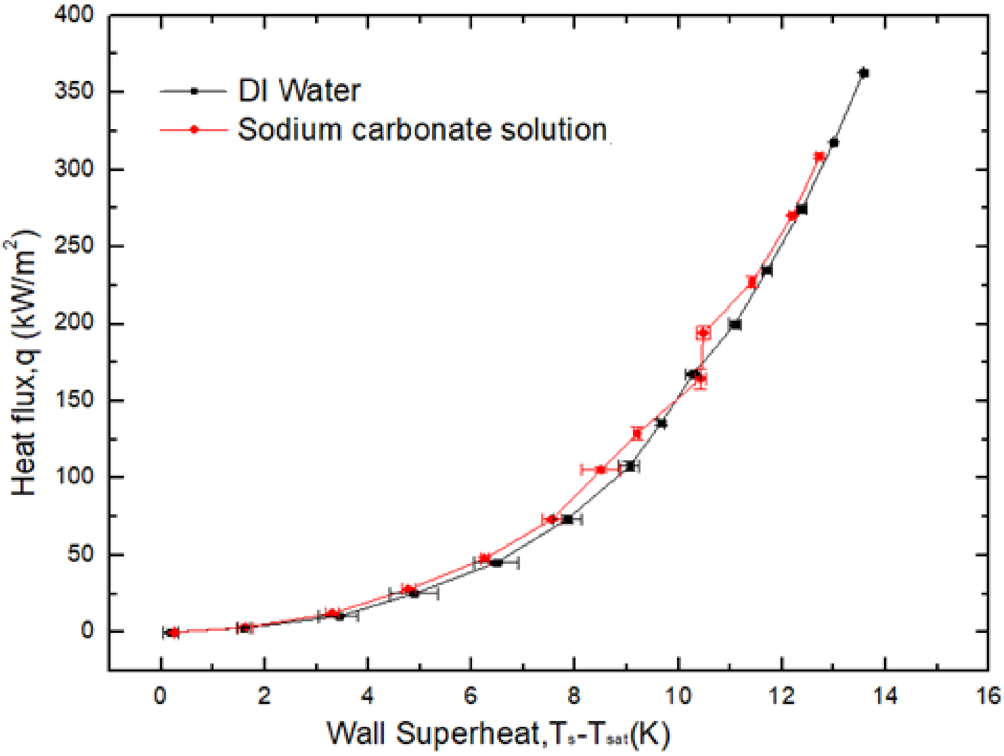

Figure 32. Pool boiling curves of DI water and Sodium carbonate solution as working fluid over a copper tube.

## 3.4 Experimental Procedure

Before the commencement of each experiment, the deionized water is utilized to clean the chamber, and the various components are assembled and configured in accordance with the requisite specifications. Subsequently, the condenser is opened to condense the vaporized water vapor into a liquid state. This process ensures that the vaporized water vapor returns to the chamber, thereby maintaining the quality of the experimental process and ensuring its constancy. Auxiliary heaters are then employed to heat the system to the saturation temperature, which is maintained for a period of 10 minutes. The signal generator, current meter, voltmeter, and power supply are opened, allowing the selected current and voltage to be adjusted. Finally, the temperature recorder is opened to record the temperature. Subsequently, the signal generator, ammeter, voltmeter, and power supply are activated and calibrated to the selected current and voltage, and the temperature recorder is initiated to record the temperature. The electrolysis current was set at 3 mA, 8 mA, 12 mA, and 16 mA. A three-minute interval was allowed for each heat flux condition to ensure that the heat transfer had been transmitted to the temperature logger, thus preventing inaccurate temperature logger measurements due to short-lived, transient heat transfer effects.

Due to the capacity limitations of the experiment equipment (cartridge heater), the test samples did not reach their CHF. Consequently, conditions that reached CHF were not considered in this study.

doi:10.6342/NTU202404361

## 3.5Data Reduction

The heat source of this study was the cartridge heater, which connected to the DC power supply. The input power (**$Q_{in}$**)was determined by the Equation (23).

$$Q_{in} = I \times U \tag{23}$$

Where ***I*** and ***U*** stand for Electric current and Electric voltage， respectively.

Before starting each experiment, a consistent layer of thermal paste was smeared between the heater and the copper tubes. The contact thermal resistance was disregarded. The loss in the axial direction is calculated by Equation 24, which employs Fourier's law of heat conduction for the copper tube on both sides.

$$Q_{loss} = 2 \times k \times A_c \times \left[\frac{T_{10mm} - T_{5mm}}{\Delta x}\right] \tag{24}$$

Where $k$ stands for the thermal conductivity of the copper tube(We used 400W/mK in this study.); **$T_{10mm}$** is the average of temperatures measured by the thermocouples which are inserted at a depth of 10mm into the copper tube; **$T_{5mm}$** is the average of temperatures measured by thermocouples which were inserted at a depth of 5mm into the copper tube; ***Ac*** represents the cross-sectional area of the copper tube(The losses from eight holes of 1mm diameter are calculated using the same principle as in the aforementioned equation but with the thermal conductivity of thermocouples, which is corrected in the calculation); The distance between the **$T_{10mm}$** and **$T_{5mm}$** thermocouples is designated as $\Delta x$. Since there is heat loss in each cross-sectional area on both sides of the copper tube, the 2 in the equation represents 2 cross-sectional areas on the left and right sides.

Next, the heat flux through the surface of the copper tube is calculated using **Equation (25)**.

$$q = \frac{Q - Q_{loss}}{A} \tag{25}$$

where ***A*** represents the outer surface of the copper tube.

The temperature of the outer surface (***Ts***) of the copper tube can be calculated according to **Equation (26)** as follows：

$$T_s = T_{avg} - \left[\frac{Q - Q_{loss}}{2\pi kL}\right] \times ln\frac{r_0}{r_c} \tag{26}$$

Where ***Ts*** stands for the temperature of the copper tube's outer surface, which is calculated based on Fourier's law of heat conduction. As the values of $\boldsymbol{T_{10mm}}$ and $\boldsymbol{T_{5mm}}$ result from direct measurement by thermocouples, these values were used in the aforementioned calculation of the heat loss from the left and right cross-sections of the copper tube. Furthermore, Fourier's law of heat conduction was employed, which assumes that the copper tube's temperature distribution is linear along the axis. This implies that if the temperature distribution along the axis of the tube is linear. By Fourier's law of heat conduction, it is possible to calculate the temperature at each point along the axis of the tube. $\boldsymbol{T_{avg}}$ stands for the calculated average of the temperature of the tube in the plane of the cylinder in which the thermocouple thermometer is located (The radius is the side surface of the cylinder where $\boldsymbol{r_c}$ is located.);$L$ is the axial length of the copper tube (in this study, L = 20 mm). $\boldsymbol{r_0}$ is the diameter of the outer surface of the copper tube (in this study, $\boldsymbol{r_0}$ = 11.5 mm), and $\boldsymbol{r_c}$ represents the measurement from the midpoint of the cross-sectional circle of the copper tube to the small hole where the thermocouple is inserted (in this study, $\boldsymbol{r_c}$ = 11 mm).

The surface superheat of a copper tube($\Delta T_w$) is calculated according to the following **Equation(27)**:

$$\Delta T_w = T_s - T_{sat} \tag{27}$$

where ***Tsat*** is the saturated temperature of DI water under atmospheric pressure.

Additionally, the HTC is calculated by Newton's Law of Cooling ,**Equation (28)**:

$$h = \frac{q}{\Delta T_w} \tag{28}$$

## 3.6 Uncertainty Analysis

In this study, the uncertainty analysis was calculated using Taylor’s method[22]. **Equation （29）（30）** estimates the uncertainties associated with wall superheat, heat flux, and heat transfer coefficient. **Table 4** presents the uncertainties for plain copper across three heat flux regimes, ranging from low to high values. For detailed calculations, please refer to the appendix.

$$\text{if } q = x + \cdots + z - (u + \cdots + w)$$

$$\delta q = \sqrt{(\delta x)^2 + \cdots + (\delta z)^2 + (\delta u)^2 + \cdots + (\delta w)^2} \tag{29}$$

$$\text{if } q = \frac{x \times \cdots \times z}{u \times \cdots \times w}$$

$$\frac{\delta q}{|q|} = \sqrt{(\frac{\delta x}{x})^2 + \cdots + (\frac{\delta z}{z})^2 + (\frac{\delta u}{u})^2 + \cdots + (\frac{\delta w}{w})^2} \tag{30}$$

Table 4 Uncertainty analysis with a plain copper tube using DIwater as the working fluid

| Uncertainty at specific heat flux | | |
|---|---|---|
| heat flux (kW/m$^2$) | Uncertainty parameter | |
| | $\Delta T_w$ (K) | h (kW/m$^2$-K) |
| q~75.30 | 0.51 | 0.99 |
| q~167.39 | 0.53 | 0.76 |
| q~336.41 | 0.54 | 0.84 |

# Chapter 4 Results and Discussion

## 4.1 Verification of the Experimental Setup

Before commencing our formal experiments, we initially evaluated the rationality of our experimental setup. This experiment used deionized water as the working fluid in horizontal copper tubes to investigate pool boiling phenomena. The results of the pool boiling experiments were plotted as pool boiling curves in **Figure 33,** and these results of pool boiling curves were then compared with those of previous authors[23-26] and the Rohsenow correlation[27]. As Arenales et al.[23] and Cheng et al.[25, 26] employed copper tubes and deionized water as working fluids, and the results of this study are in general agreement with those of Roensow[27]; the experimental setup can be demonstrated to be reliable.

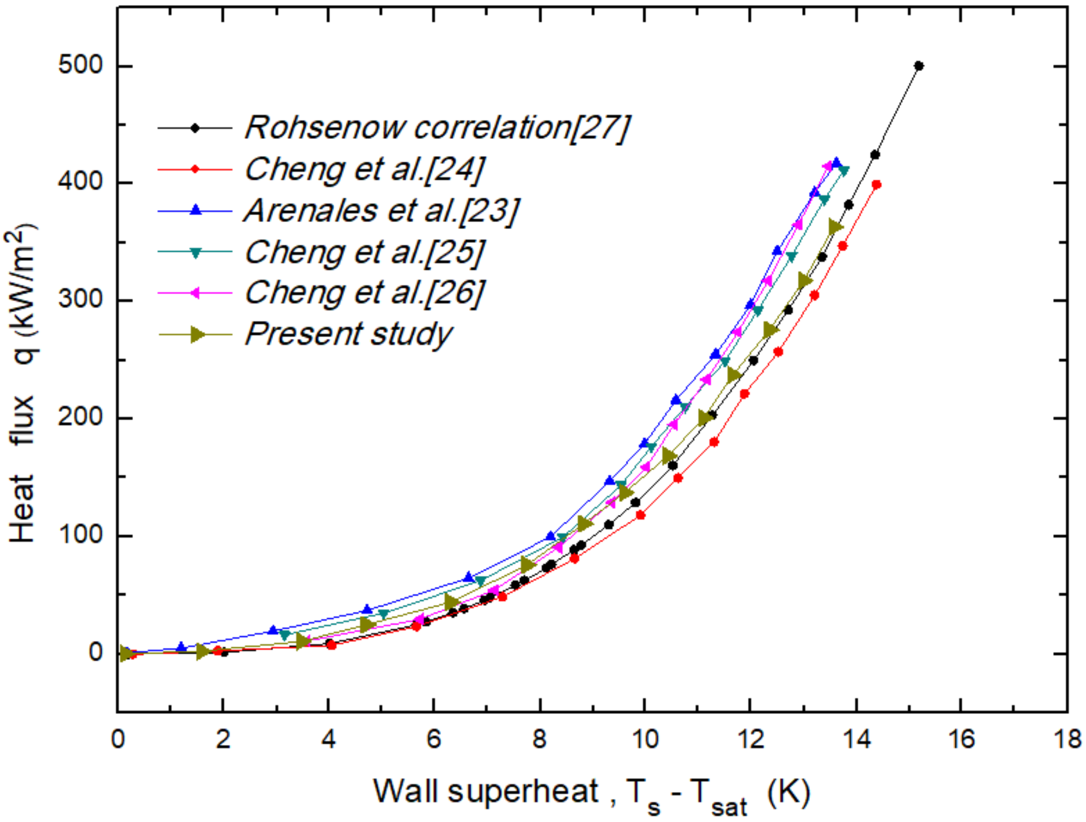

Figure 33. Cylindrical Copper Tube with DI Water as working fluid of Pool Boiling Curves and Previous Studies and Rohsenow Correlation.

## 4.2 Mechanism of electrolytic boiling heat transfer

This study conducted experiments to explore liquid pool boiling using an electrolysis method. The experimental principle is illustrated in the accompanying **Figure 34**. During the electrolysis process, the surface of copper serves as the cathode, and hydrogen bubbles are generated. Another electrode is inserted into the working fluid. Thus, hydrogen is generated on the surface of copper to prevent the oxidation of the copper surface caused by oxygen. The working fluid is sodium carbonate solution, as it is a salt solution that does not have any chemical reaction with copper. During the electrolysis process, hydrogen generation increases due to the number of nucleation sites on the copper surface. These hydrogen bubbles attach to particles on the copper surface or on the surface of the copper column and become new nucleation sites, promoting the formation and detachment of more bubbles. During the nucleation phase, this frequent bubble generation and detachment significantly enhances the heat transfer efficiency because each bubble carries away some heat as it detaches from the heated surface. Consequently, the generation of hydrogen enhances the heat transfer by increasing the number of nucleation points and promoting pool boiling.

T. Tanaka[10] researched electrolysis's enhanced effect on pool boiling. It was discovered that the hydrogen bubbles generated by electrolysis could act as nuclei of the boiling bubbles, effectively increasing the density of nucleation points and thus significantly improving the heat transfer efficiency. In the initial stage, the hydrogen produced dissolves into the working fluid. Subsequently, hydrogen near the copper tube becomes oversaturated and moves towards the heated copper surface in bubbles. These bubbles serve as nuclei for vapor bubbles during boiling. Increased bubble nucleation, caused by the phase change from liquid to gas due to latent heat, is further enhanced by

doi:10.6342/NTU202404361

electrolysis to improve the boiling heat transfer coefficient (HTC)."

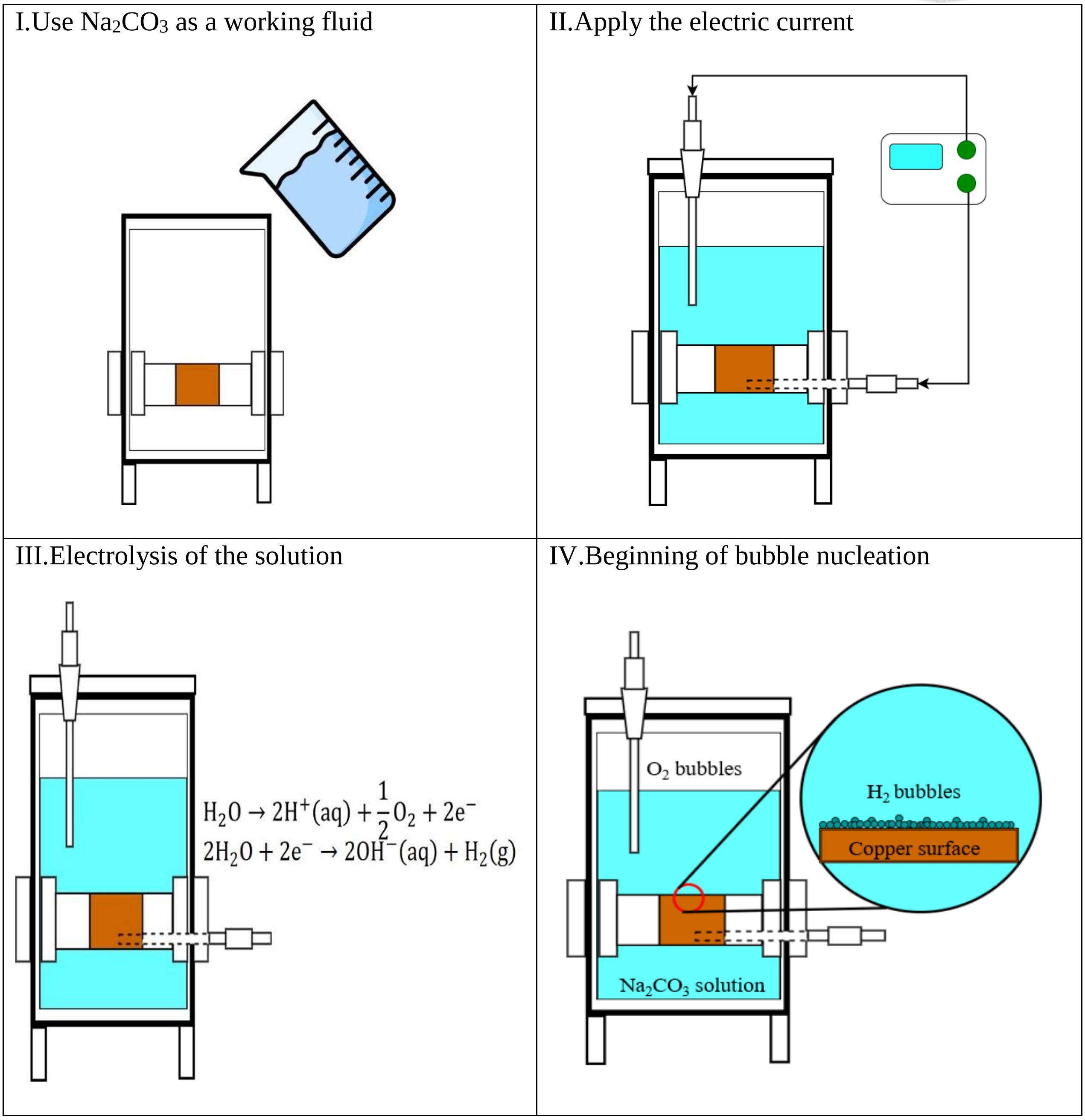
I.Use $Na_2CO_3$ as a working fluid

II.Apply the electric current

III.Electrolysis of the solution

IV.Beginning of bubble nucleation

Figure 34.Mechanism of electrolytic pool boiling.

The Volumetric hydrogen production rate by electrolysis can be calculated using Faraday's law.[28] In the context of pool boiling experiments, electrolysis is conventionally posited as the mechanism responsible for generating hydrogen vapor bubbles, as evidenced in **Figure 35.** This premise finds theoretical grounding in Equation (20) and Equation (21), which delineate the volumetric hydrogen production rate in accordance with Faraday's law and elucidate the vapor production rate, respectively. It is noteworthy that bubble nucleation commences at a notably low heat flux, approximately 3.74 kW/m², as evidenced by the bubble kinetic image in **Figure 35**, under specific experimental conditions of applied current. The volumetric generation rate of hydrogen gas, denoted as $V_h$, is calculated using the equation:

$$V_h = f \times vol_m \times \frac{I}{vF} \tag{20}$$

Here, $\boldsymbol{f}$ represents the gas evolution efficiency, assumed to be 1 for simplification. $\boldsymbol{vol_m}$ denotes the molar volume, and $\boldsymbol{v}$ indicates the number of electrons transferred in the reaction, equaling 2. $\boldsymbol{F}$ represents the Faraday constant.

The Volumetric vapor generation rate is derived from the following equation:

$$V_v = \frac{qA}{\rho_v h_{lv}} \tag{21}$$

Where $V_v$ is the volumetric generation rate for vapor, $q$ is the heat flux, $A$ is the heated surface area, $\boldsymbol{\rho_v}$ is the density for vapor and $h_{lv}$is the latent heat for liquid and vapor phase change.

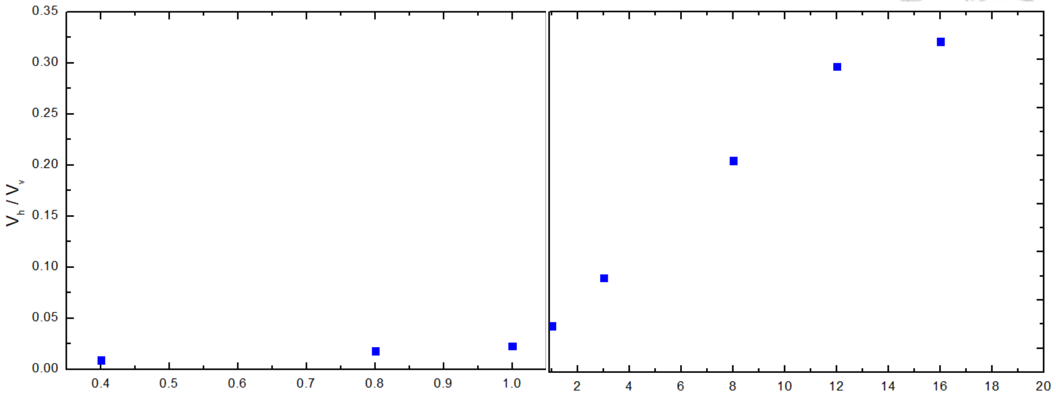

Figure 35.The volumetric generation rate of hydrogen gas at the heat flux of ~3.74 kW/m$^2$ in pool boiling.

## 4.3 Comparison of Unidirectional Square Wave Pulsed Current and Direct Current Electrolysis in Pool Boiling Heat Transfer

The experimental conditions for the electrolytic boiling are outlined in **Table 5. T**he principal factor that distinguishes the experimental settings is the varying levels of applied current, which result in differing electrolytic capacities. During the experiment, we compared the unidirectional square wave current (P1-P4) and the direct current (D1-D5). The objective was to investigate the distinction between unidirectional square wave current electrolysis and direct current electrolysis. The waveforms of the unidirectional square wave pulsed current and the direct current is illustrated in **Figure 36.**

doi:10.6342/NTU202404361

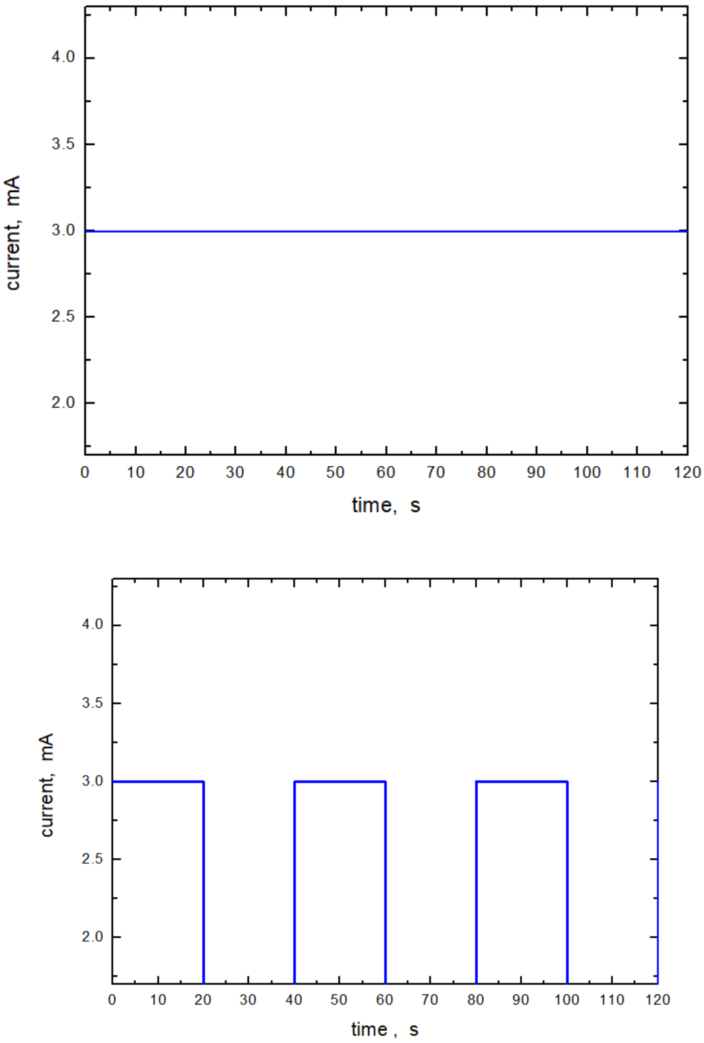

Figure 36.Waveforms of Direct Current and unidirectional square wave currents.

doi:10.6342/NTU202404361

Table 5 .Experimental conditions for electrolytic pool boiling using $Na_2CO_3$ water solution as the working fluid.

| **Test Conditions** | **Working fluid** | **Current of Electrolysis** | **Description** |
|---|---|---|---|
| B0 | DI water | 0 mA | No Electrolysis |
| P1 | $Na_2CO_3$ water solution | 3mA | Unidirectional Square Wave Pulsed Current |
| P2 | $Na_2CO_3$ water solution | 8mA | Unidirectional Square Wave Pulsed Current |
| P3 | $Na_2CO_3$ water solution | 12mA | Unidirectional Square Wave Pulsed Current |
| P4 | $Na_2CO_3$ water solution | 16mA | Unidirectional Square Wave Pulsed Current |
| D1 | $Na_2CO_3$ water solution | 3mA | Direct Current |
| D2 | $Na_2CO_3$ water solution | 8mA | Direct Current |
| D3 | $Na_2CO_3$ water solution | 12mA | Direct Current |
| D4 | $Na_2CO_3$ water solution | 16mA | Direct Current |

doi:10.6342/NTU202404361

As presented in **Table 5,** the first set of experiments employed unidirectional square wave pulsed currents and Direct Currents, respectively. In this thesis, the peak value of the square wave pulsed current is taken as the current value. The rationale for using the square wave current is that it can be considered an intermittent on-off control with the on-time equivalent of a Direct Current. In the first set of experiments, the period of the unidirectional square wave pulsed current was set to 40 seconds, with a frequency of 25 mHz. This equates to a period of 20 seconds of energized time and a period of 20 seconds of unenergized time. The experimental data obtained during the energized period was used as the result. The rationale behind selecting 40 seconds is that although the current is generated immediately following energization, the ions or groups of ions in the solution will only produce hydrogen through the gain or loss of electrons. This chemical reaction will take some time, as the objective of the experiment is to create more nucleation points through hydrogen production and to make an enhancement of heat transfer in pool boiling. The discussion of frequency will be carried out in the next set of experiments. According to the experimental conditions in **Table 5**, the electrolysis currents were 3mA, 8mA, 12mA, and 16mA, and their pool boiling curves are shown in **Figure 37**. and **Figure 38.**

**Table 6** and
**Table** 7 present the results of heat transfer coefficient (HTC) enhancement using sodium carbonate solution as the working fluid under direct current and unidirectional square wave current electrolysis (with a frequency of 25mHz) with currents of three mA, eight mA, twelve mA, and sixteen mA at107.74 $kW/m^2$ and 363.41 $kW/m^2$ respectfully.

The overall effect of unidirectional square wave electrolysis on HTC is superior to that of DC electrolysis. In the case of DC electrolysis, electrolysis occurs continuously, resulting in the constant generation and polymerization of hydrogen bubbles. Excessive polymerization can delay bubble detachment, potentially decreasing HTC. Conversely, with unidirectional square wave electrolysis, electrolysis pauses periodically, allowing bubbles sufficient time to detach, thus preventing excessive bubble accumulation and maintaining higher HTC. Consequently, the overall effect of unidirectional square wave electrolysis on HTC is superior to that of DC electrolysis.

The study shows the highest HTC increase of 31% when utilizing 12 mA unidirectional square wave electrolysis at 107.74 kW/m². The authors attribute this enhancement to bubble dynamics, discussed in detail in section 4.5.

Table 6. The enhancement ratio of HTCs at a heat flux of 107.74 kW/m².

| Electrolysis current | $h_p/h_{B0}$ | $h_D/h_{B0}$ |
|---|---|---|
| B0(0mA) | -- | -- |
| 3mA | 1.16 | 1.07 |
| 8mA | 1.16 | 1.06 |
| 12mA | 1.31 | 1.21 |
| 16mA | 1.29 | 1.15 |

Table 7.The enhancement ratio of HTC at a heat flux of 363.41 kW/m².

| Electrolysis current | $h_p/h_{B0}$ | $h_D/h_{B0}$ |
|---|---|---|
| B0(0mA) | -- | -- |
| 3mA | 1.07 | 1.00 |
| 8mA | 1.10 | 1.09 |
| 12mA | 1.30 | 1.13 |
| 16mA | 1.24 | 1.08 |

**Figure 37-40** shows the pool boiling curves and HTC curves for 3mA.8mA.12mA.16mA DC electrolysis and unidirectional square wave pulsed current electrolysis. In the initial stage, with the increase of current, the pool boiling curve shifts to the left, and the heat transfer coefficient becomes higher. However, at 16mA, the pool boiling curve no longer shifts to the left. However, the heat transfer performance becomes worse, which may be because, with the increase of current, the amount of nucleation points becomes more and more, but at 16mA, the excessive number of nucleation points may lead to the polymerization of bubbles, which in turn leads to too many bubbles attaching. Too many bubbles adhere to the surface and cannot be released quickly, decreasing heat transfer efficiency.

doi:10.6342/NTU202404361

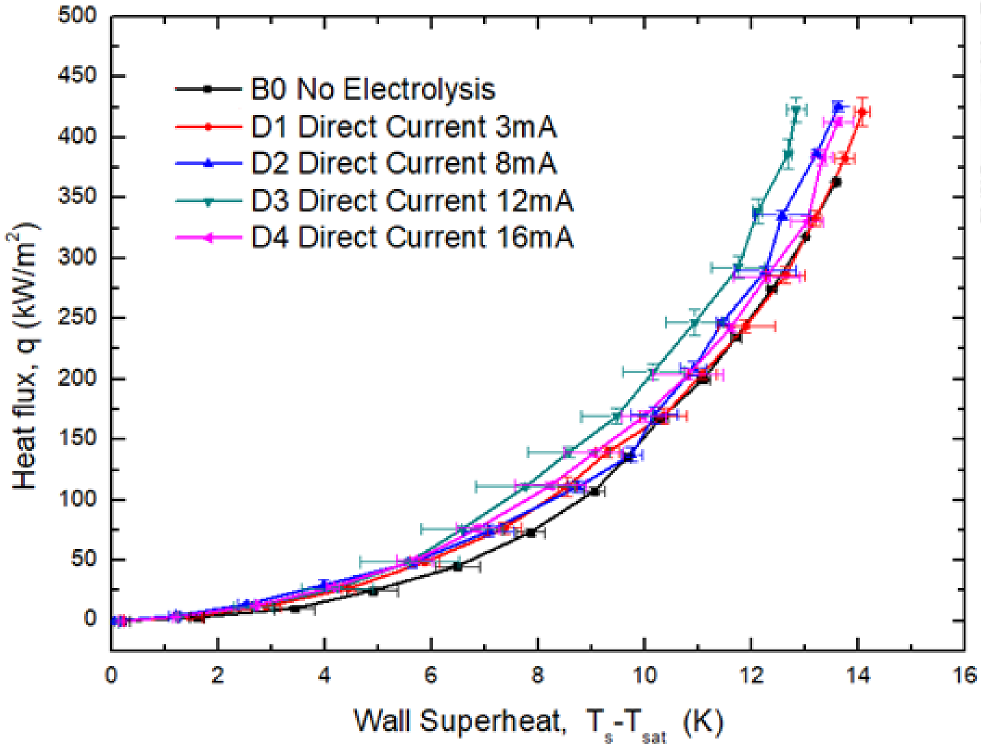

Figure 37. Pool boiling curves for electrolysis ($Na_2CO_3$ water solution,Direct Current).

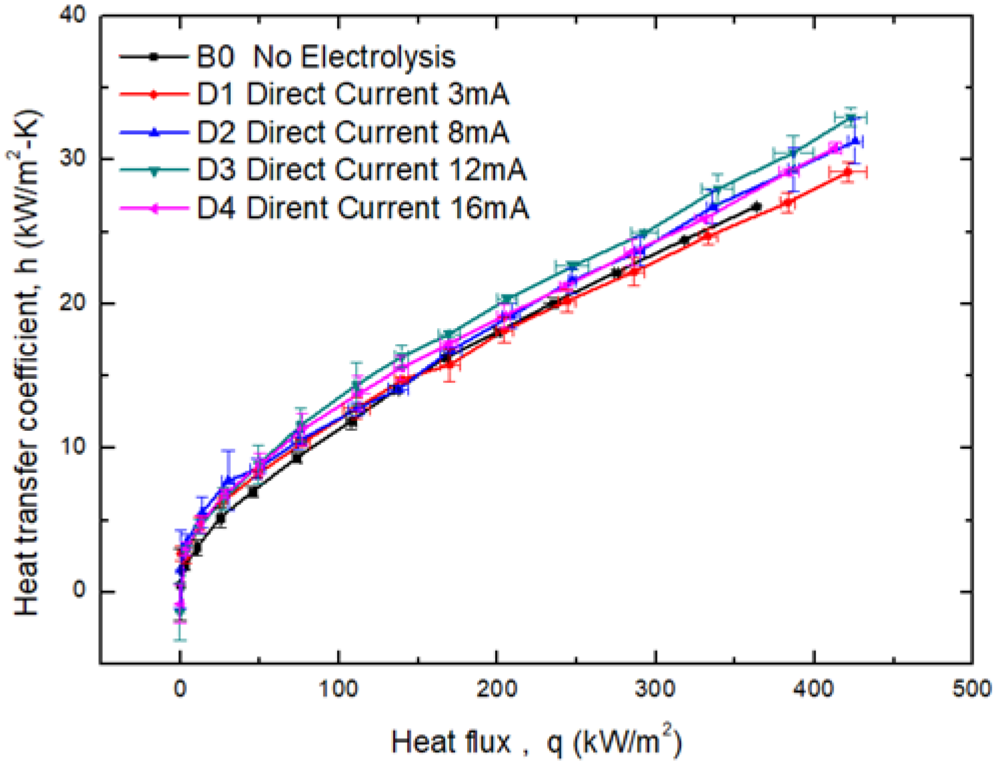

Figure 38. HTCs of test conditions for electrolysis ($Na_2CO_3$ water solution, Direct Current).

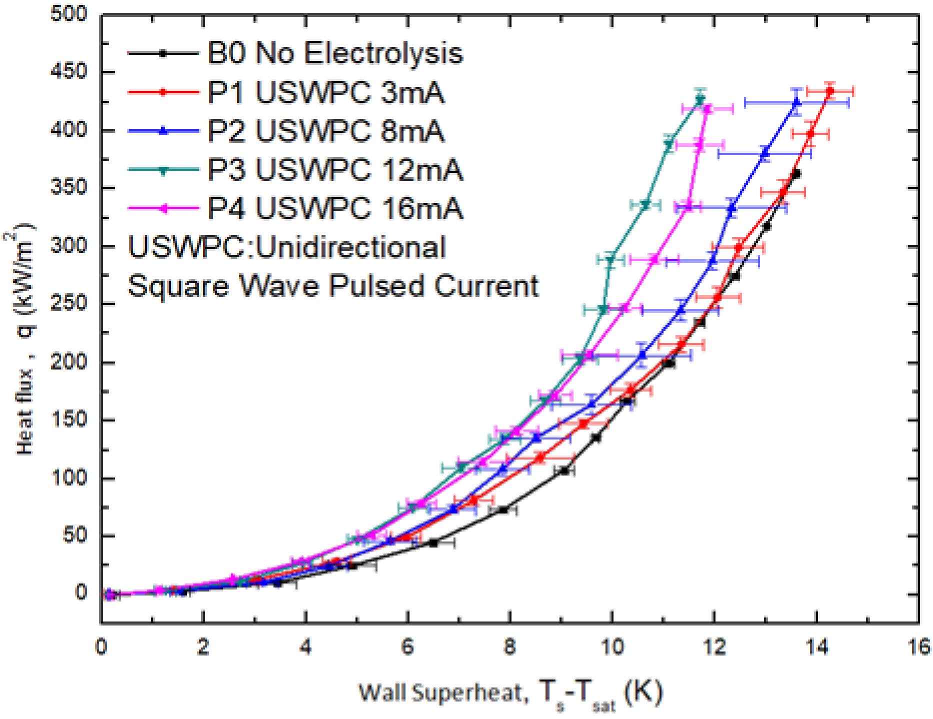

Figure 39. Pool boiling curves for electrolysis ($Na_2CO_3$ water solution,.Unidirectional Square Wave Pulsed Current).

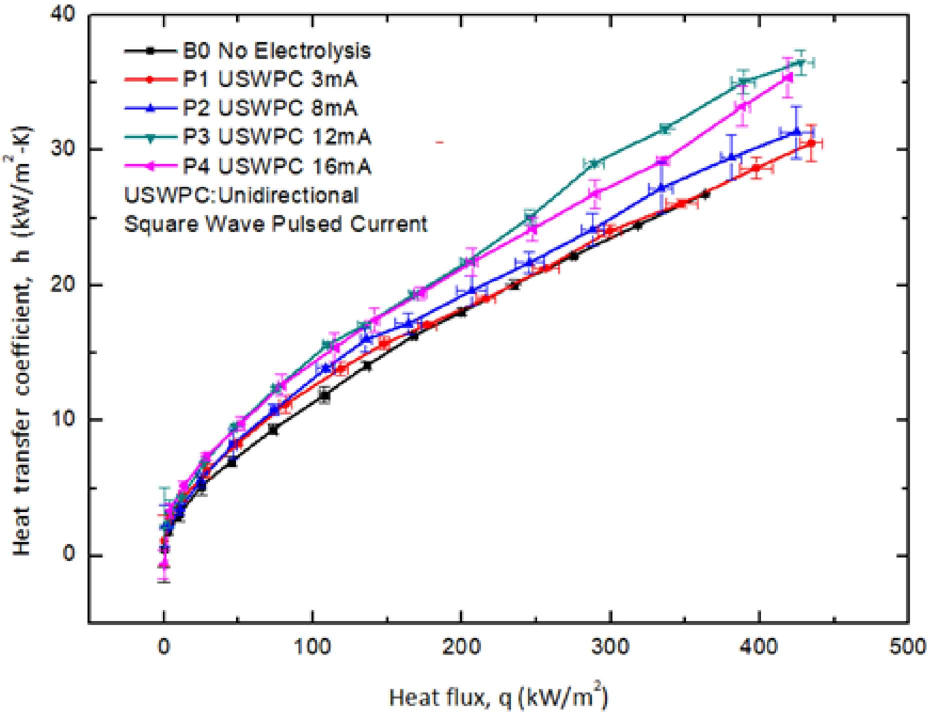

Figure40. HTCs of test conditions for electrolysis ($Na_2CO_3$ water solution , unidirectional square wave plused current).

doi:10.6342/NTU202404361

**Figures 41-48** compare the results of pool boiling curves for DC and unidirectional pulsed current at 3mA, 8mA, 12mA, and 16mA, respectively. It can be observed that the electrolysis of DC and unidirectional pulsed current is nearly identical to the curve of pure water at 3mA and 8mA due to the relatively low current intensity. However, at 12mA and 16mA, the curves diverge. As observed, the electrolysis of DC and unidirectional pulsed current is nearly identical to the curve of pure water at 3mA and 8mA, which can be attributed to the relatively modest current intensity. However, at 12mA and 16mA, However, at 12mA and 16mA, the heat transfer effect of single pulse current electrolysis is superior to that of DC electrolysis. This may be attributed to the unidirectional pulsed current not being electrolyzed for a certain period during the electrolysis process. In contrast to DC, the air bubbles can be detached by utilizing this brief period without electrolysis, thus preventing excessive air bubbles from gathering on the surface and enhancing the heat transfer performance and HTC.

doi:10.6342/NTU202404361

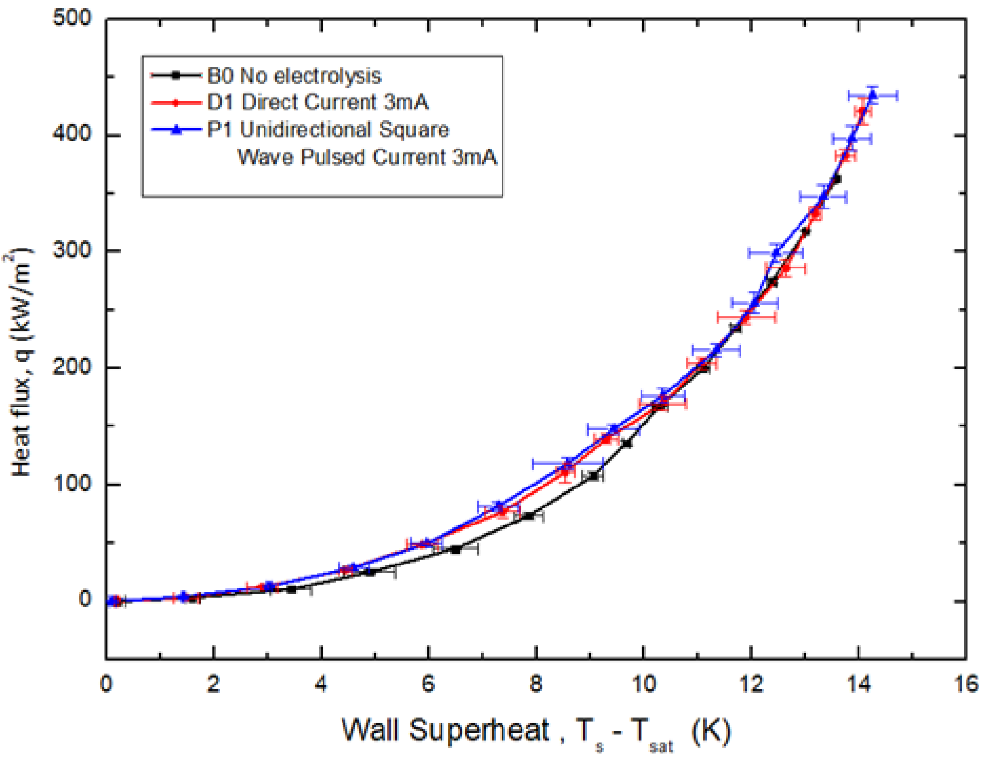

Figure 41.Comparison of pool boiling curves for unidirectional square wave current and DC current at 3mA.

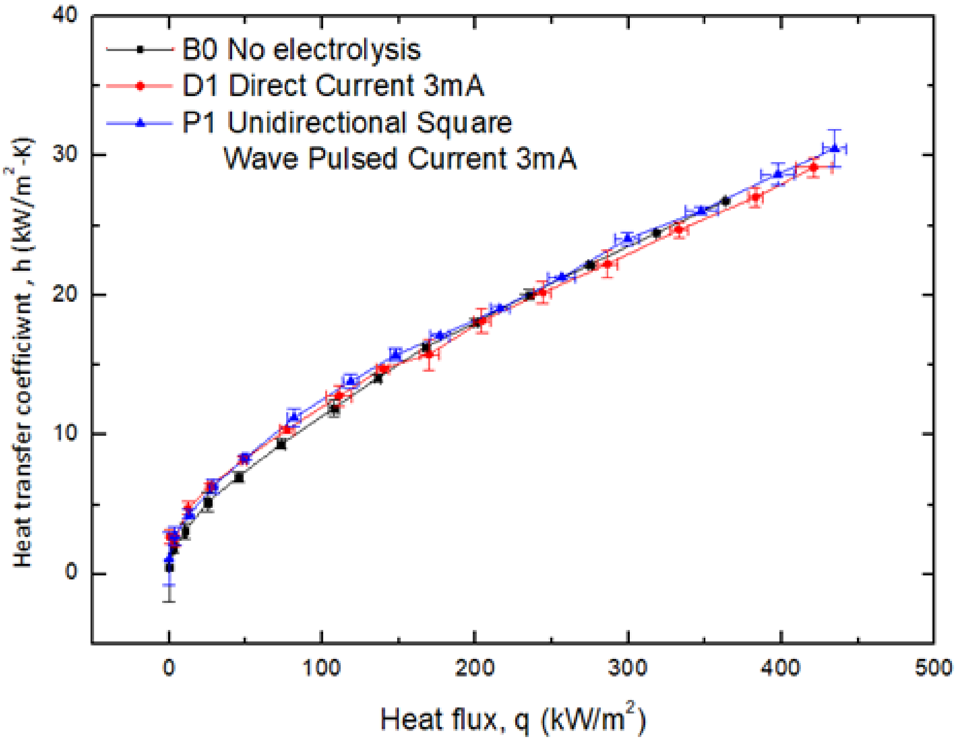

Figure 42.Comparison of HTC curves of unidirectional square wave current and DC current at 3mA.

doi:10.6342/NTU202404361

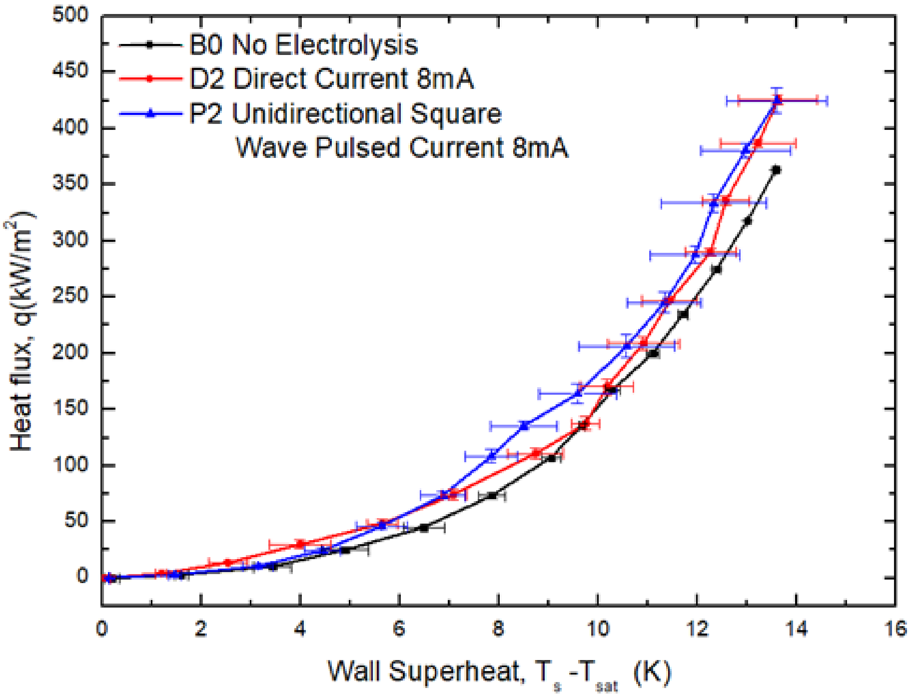

Figure 43.Comparison of pool boiling curves for unidirectional square wave pulsed current and DC current at 8mA.

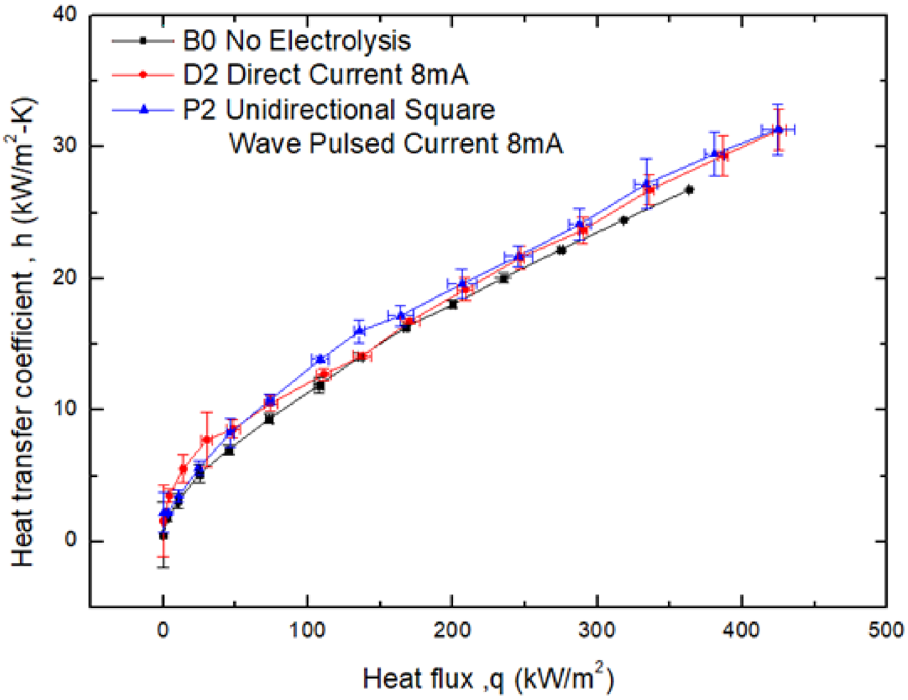

Figure 44.Comparison of HTC curves of unidirectional square wave current and DC current at 8mA.

doi:10.6342/NTU202404361

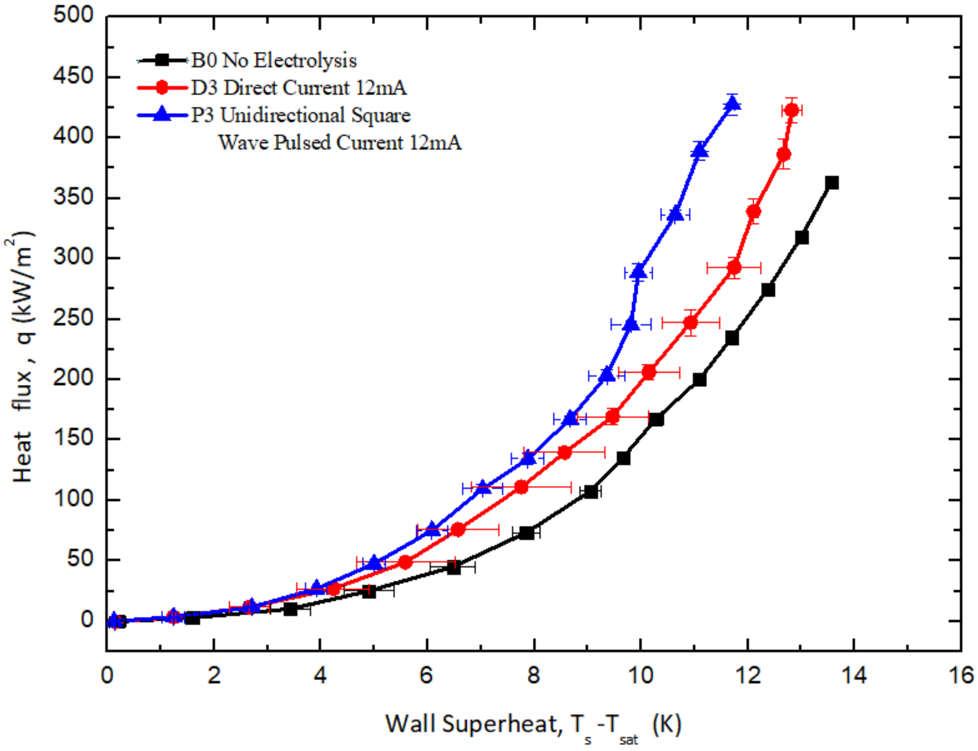

Figure 45.Comparison of pool boiling curves for unidirectional square wave pulsed current and DC current at 12mA.

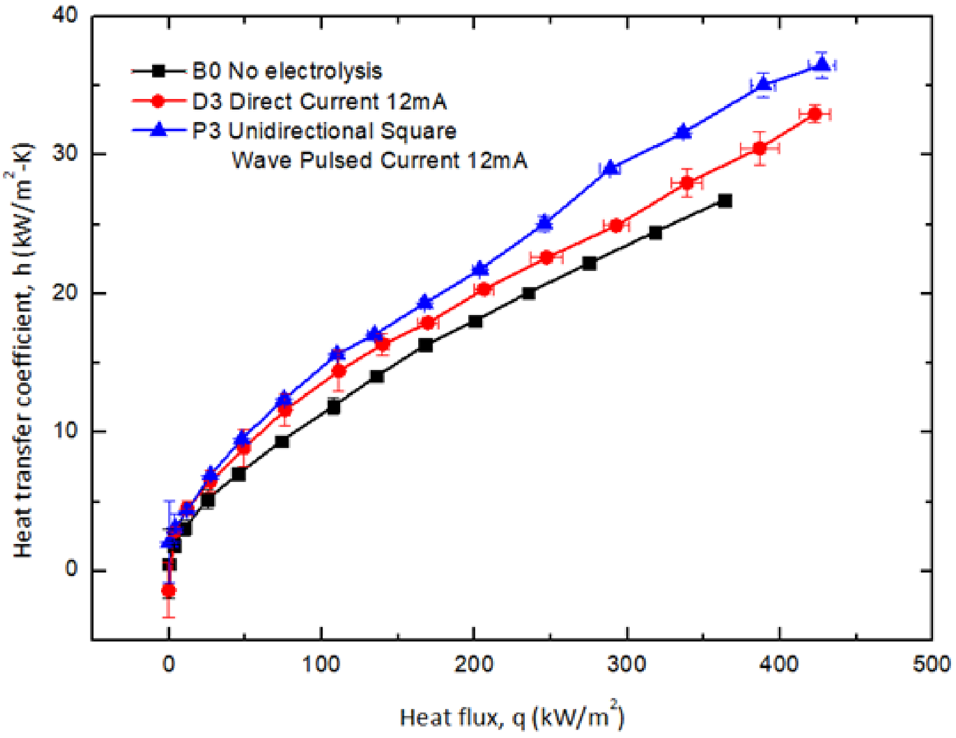

Figure 46.Comparison of HTC curves of unidirectional square wave pulsed current and DC current at 12mA.

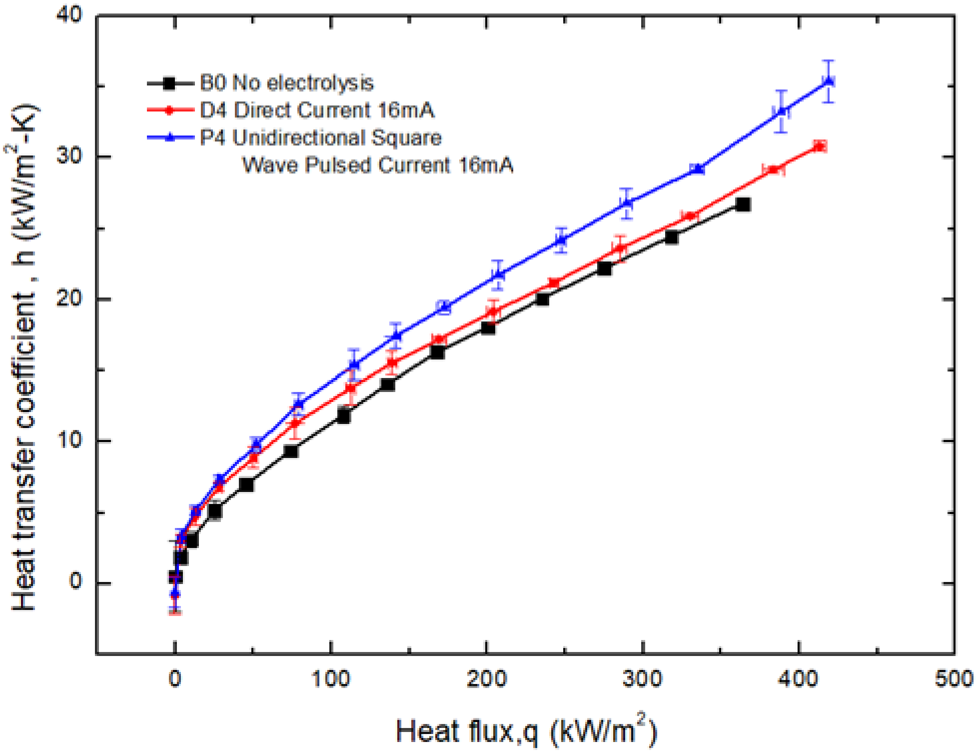

Figure 47.Comparison of pool boiling curves for unidirectional square wave current and DC current at 16mA

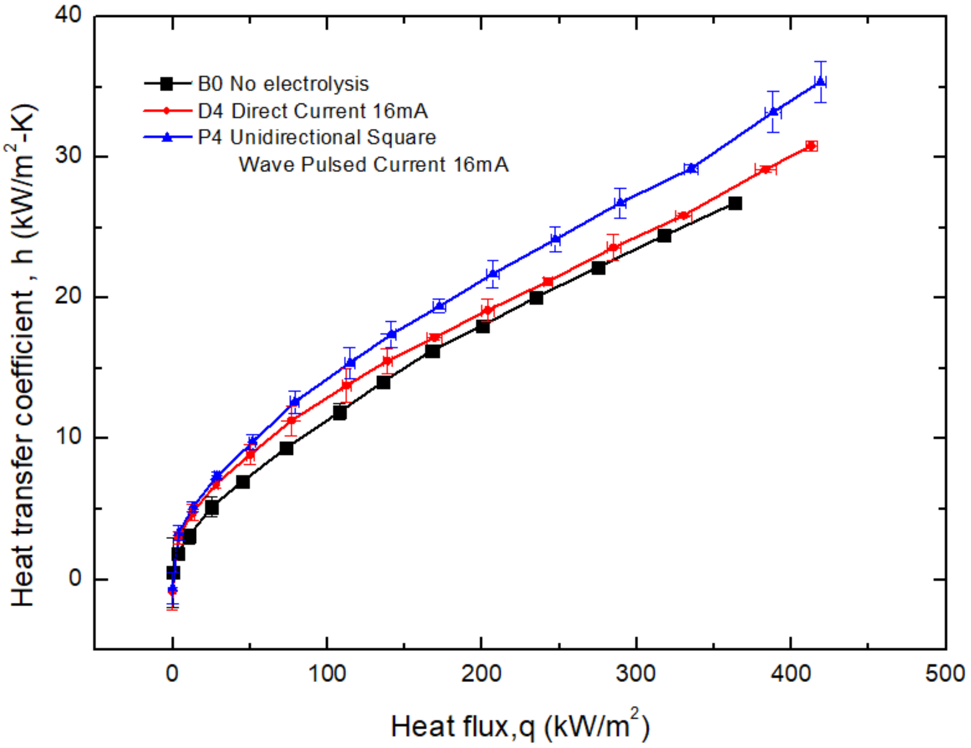

Figure 48. Comparison of HTC curves of unidirectional square wave current and DC current at 16mA.

doi:10.6342/NTU202404361

## 4.4 Comparison of boiling curves in using different frequency of unidirectional Square Wave Pulsed Current Electrolysis in Pool Boiling Heat Transfer

In this study, unidirectional square wave pulsed current electrolysis was employed to regulate the generation of hydrogen bubbles during electrolysis. As outlined in Chapter 3, the initial period was chosen to be 40 seconds at 25mHz. The rationale behind selecting this frequency and period is that when the current signal is emitted, the ions in the water move, and the chemical reaction takes a certain amount of time. If the period is longer, it may result in a chemical reaction in the water after the current signal is emitted. If the period is too short, it may result in the chemical reaction in the water occurring too soon for the formation of hydrogen to increase the nucleation point. Conversely, if the period is too long, there is no difference between the electrolysis in the energized time and the DC electrolysis, and there is no electrolysis effect to help the electrolysis effect in the non-electrified. Therefore, a frequency of 25mHz was selected for the experiment. The present study continues to explore the results in a similar frequency, as shown in **Figure 49.** This figure illustrates the boiling curves obtained using unidirectional square-wave pulsed current electrolysis at three different frequencies. It can be observed that due to the overlapping error ranges, it is not possible to determine which frequency is superior. However, it can be stated that within this range, the change in frequency does not have a significant effect on the results.

In practical industrial applications, such as electronic components cooling, etc., the objective is to reduce the likelihood of overheating while simultaneously enhancing the heat flux. However, if the period of USWPC is too long, it may result in re-cell boiling at a later stage rather than electrolysis. The temperature of the heating unit increases because

doi:10.6342/NTU202404361

of the time interval of no electrolysis. The present study employs a frequency of 25mHz, with an electrolysis cycle duration of 20 seconds. The experimental results indicate that the temperature rise during the 20-second electrolysis process will not exceed 1 degree Celsius (generally within 0.5 degrees Celsius). This tiny temperature rise can be ignored, preventing overheating while improving the HTC.

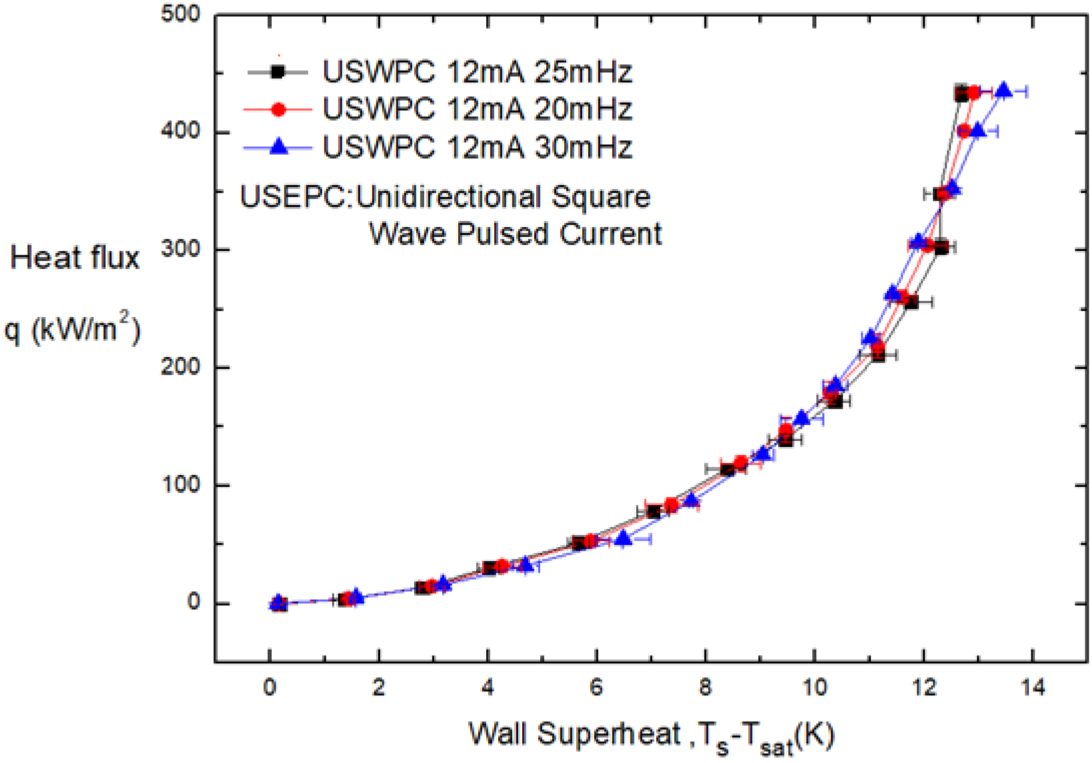

Figure 49.Comparison of pool boiling curves for unidirectional square wave current in different frequencies at 12mA

doi:10.6342/NTU202404361

## 4.5Bubble dynamics

**Figure 50.** shows a high-speed image capturing the bubble dynamics at the five different heat flux levels. The photographs demonstrate that the onset of nucleation at the point of nucleation (ONB) in the presence of current electrolysis occurs much earlier than in its absence (at ~3.74 kW/m2). This is attributed to hydrogen production due to the electrolysis effect, which promotes the generation of gas bubbles and early nucleation. As illustrated in the figure, at a heat flux of 3.74 kW/m², P1, P2, P3, and P4 have already reached ONB, whereas B0 has not yet reached ONB. This demonstrates the positive effect of electrolysis, which can be observed in the earlier nucleation at lower superheat compared to no electrolysis. The positive effect of electrolysis can be demonstrated.

A comparison of the results of each picture at 27.09 kW/m2 reveals that as the electrolytic current increases, the greater the electrolytic current, the more air bubbles with more nucleation points. Combined with the pool boiling curve, this trend suggests that the heat transfer rate also increase as the amount of nucleation points increases. However, when the boiling curve is considered, the optimal HTC is observed at 12 mA, while at 16 mA, the HTC is less favorable. This may be attributed to the high density of bubbles produced, which increases the likelihood of these bubbles merging. However, after merging, the larger bubbles detach less frequently. These bigger bubbles stay on the heated surface for a longer duration, which impedes the heat transfer from the heated surface. Due to the limited recirculation path of the liquid, the bubbles were carried away slowly enough, resulting in an HTC that was not as high as the 12 mA result but higher than the three mA and eight mA results.

doi:10.6342/NTU202404361

| Test Conditions | ~3.74 kW/m² | ~27.09 kW/m² | ~75.30 kW/m² | ~167.39 kW/m² | ~336.41 kW/m² |
|---|---|---|---|---|---|
| B0 | 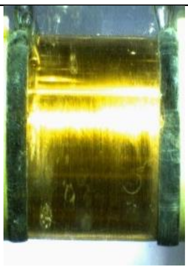 | 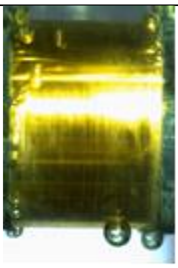 |  |  |  |
| P1 (3mA) |  |  |  |  | 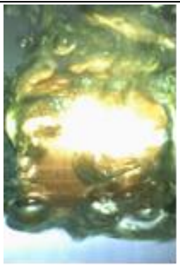 |
| P2 (8mA) |  |  |  |  |  |
| P3 (12mA) |  |  |  |  |  |
| P4 (16mA) | 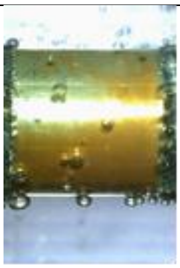 | 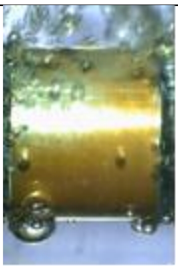 |  |  |  |

Figure 50.High-speed imaging was employed to document the dynamics of bubbles at varying heat flux intervals during the course of electrolytic boiling experiments conducted with a sodium carbonate solution serving as the working fluid.

| Test conditions | P1（3mA） | P2（8mA） | P3（12mA） | P4（16mA） |
|---|---|---|---|---|
| Bubble Images |  |  |  |  |
| Bubble Evolution Rate(ms) | 25-35ms | 25-30ms | 15-25ms | 30-40ms |

Figure 51. Bubble Dynamics at a Heat Flux of 107.74 $kW/m^2$ During USWPC Electrolytic Boiling Using $Na_2CO_3$ Solution as the Working Fluid

As illustrated in **Figure 51,** this figure depicts the bubble dynamics at a heat flux of 107.74 $kW/m^2$. The results of the high-speed camera demonstrate that at 3mA and 8mA, the time from bubble generation to detachment is generally in the range of 25-30ms. At 12mA, the time from bubble generation to detachment is generally between 15-25ms. At 16 mA, The time from bubble generation to detachment is generally in the range of 30-40 ms, because The higher current results in a more significant number of nucleation points, leading to the polymerization of bubbles with their surrounding environment. This process then allows for the detachment of the bubbles, with the resulting detachment time typically falling within the range of 30 to 40 milliseconds.

## 4.6Circumferential surface temperature difference

Experimental observations revealed that at the onset of boiling in the pool, the lower surface of the circular tube generates bubbles first, followed by the upper surface. Consequently, this study quantified the temperature differential between the upper and lower surfaces, as illustrated in **Figure 52.**

The temperature difference between the upper and lower surfaces is defined in **Figure 52**, where the upper surface temperature is the mean of the four thermocouple measurements above the circular tube, and the lower surface temperature is the mean of the four thermocouple intervals below the circular tube. The experimental results show that the temperature disparity between the upper and lower surfaces is at its peak at a lower heat flux (approximately 52.43 kW/m²). As the heat flux continues to increase, this temperature difference gradually decreases.

doi:10.6342/NTU202404361

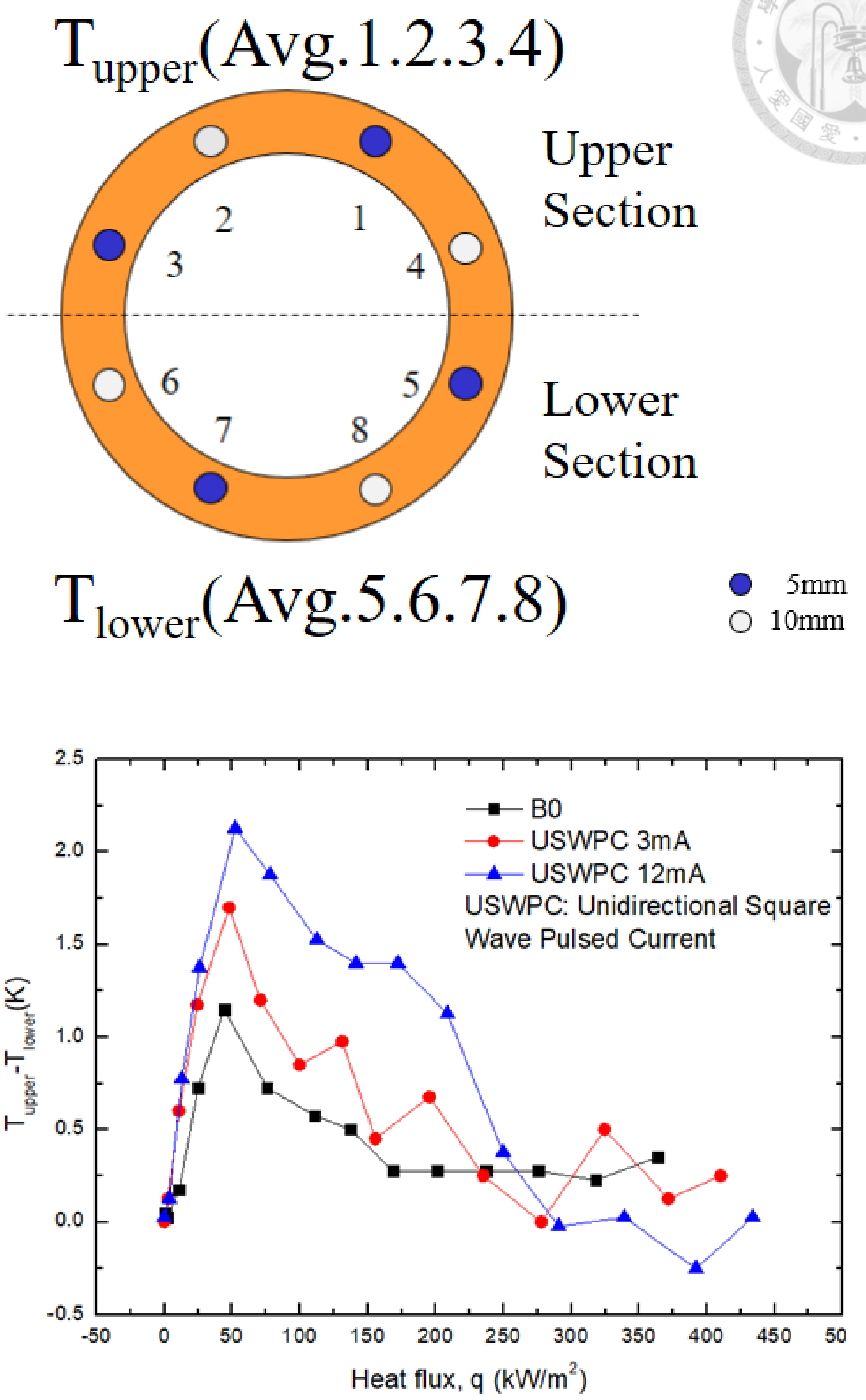

Figure 52. Temperature differences of copper tube surface for the test conditions B0, P1 and P3.

doi:10.6342/NTU202404361

The variation in temperature between the upper and lower surfaces reveals the microscopic processes that occur during boiling. It is evident that a small amount of air is always present in the interior of the liquid and that air is also adsorbed on the walls of the container and the surfaces of solid impurities. As the liquid in the container heats up, the kinetic energy of the air molecules increases, leading to more vigorous thermal motion and the transition of the liquid into a gaseous state. This process gives rise to forming a small bubble at the interface between the liquid and the gaseous phase. Additionally, a limited number of liquid molecules become gaseous due to evaporation and enter the bubble, contributing to the presence of both air and saturated vapor within the bubble.

Given that the density of air is less than that of water, it can be postulated that the air molecules within the pores on the upper surface are readily dislodged by the action of buoyancy. At the outset of the boiling stage of the pool, typically, the lower surface produces bubbles first. This does not imply that the upper surface does not produce bubbles; rather, it is due to the detachment of air molecules from the voids on the upper surface. The action of buoyancy results in the upper surface of the voids becoming less dense, which in turn facilitates the formation of nucleation sites. The density of the voids on the upper surface is less, and the amount of nucleation sites is less. Prior to the commencement of the heating process, the air within the void on the lower surface contains a large number of nucleation sites due to its adhesion to the copper tube. This results in the formation of air bubbles at the outset of the boiling phase of the pool. The addition of the electrolysis effect, a process where a direct electric current is passed through a liquid causing it to decompose into its elements, results in the initial stage of the boiling phase of the pool being characterized by the formation of bubbles on both the upper and lower surfaces. These bubbles nucleate earlier than those on the upper surface due to the phase transition potential taking away heat. Consequently, in low heat flux conditions, the temperature distinction between the upper and lower surfaces is greater.

As the heat flux increases, the heat transfer rate per unit area increases, and the liquid undergoes gasification, accompanied by adding air molecules. At high heat flux, the upper and lower surfaces of the copper tube are characterized by the presence of numerous air bubbles. The simultaneous phase change potential of the upper and lower surfaces results in the removal of a considerable quantity of heat, thereby reducing the temperature difference between the upper and lower surfaces.

# Chapter 5 Conclusions and Future Prospects

## 5.1 Conclusions

This study investigated the impact of unidirectional square wave pulsed current electrolysis heat transfer in horizontal copper tubes of pool boiling , utilizing diverse voltages and frequencies for electrolysis. The outcomes of unidirectional pulsed-current electrolysis were compared with those of direct-current electrolysis. The bubbles' kinetic properties were also investigated through a high-speed video camera. The findings of this research could be summarized as follows:

- Using a sodium carbonate solution as the working fluid has been demonstrated to facilitate an enhancement in the heat transfer effect observed in pool boiling. The observed effect is due to the production of hydrogen bubbles via electrolysis, which boosts the quantity of nucleation sites. Consequently, this improves the two-phase heat transfer efficiency and mitigates wall surface overheating. Nevertheless, irrespective of whether unidirectional square-wave pulse current or DC current electrolysis is employed, the heat transfer rate is disproportionate to the associated current.The HTC of unidirectional square-wave pulse current and DC is increased by 1.31 and 1.21 times, respectively, when electrolysed at 12 mA. And The application of the electrolysis method requires a lower energy input compared to other techniques.
- In the present study, unidirectional square wave pulse electrolysis was conducted at 25 mHz. This frequency was selected based on the observation that the chemical reaction required for electrolysis requires a certain amount of time before bubbles

doi:10.6342/NTU202404361

can be produced. The study's results demonstrated no significant difference in the effect on heat transfer enhancement in the frequency range of 20-30 mHz.

- In this research , the temperature distributions of the upper and lower surfaces of the circular tube were measured and compared. The experimental results demonstrate that the temperature of the upper surface is typically higher than that of the lower surface during the low heat flux stage, irrespective of electrolysis. The maximum peak temperature difference is observed at a heat flux of approximately 52.43 kW/m². This phenomenon can be attributed to the early nucleation of the lower surface at the outset, which impedes the temperature of the lower surface from rising significantly due to effective heat dissipation. Following the peak value, the temperature difference between the upper and lower surfaces gradually balances out with the increase of heat flux, ultimately reaching a stable value. Furthermore, it was observed that the boiling experiment utilizing electrolysis could attain higher peaks. This was attributed to the electrolysis effect, which increased nucleation points, thereby creating a larger temperature differential between the upper and lower surfaces at low heat fluxes.

## 5.2Future prospects

This study investigated the heat transfer behavior of pool boiling on the surface of a horizontal circular tube using unidirectional pulsed square-wave currents and direct current electrolysis. However, the heat flux provided by the heater was unable to reach the critical heat flux due to the limitations of the experimental equipment. Furthermore, this study can be extended and developed in the following aspects:

- Experiment with different concentrations and working fluids; different concentrations mean different conductivity. The higher the concentration, the better the conductivity and the greater the electrolysis effect. However, higher concentrations make the solution more viscous and, therefore, do not necessarily help to improve boiling behavior. In conclusion, the concentration of the working fluid may be an interesting topic for further study.
- Applying electrically enhanced pool boiling in reheat exchangers is also a direction for future research and development. In this study, only the level of a single copper tube has been investigated, not the level of the heat exchanger system, and in the future, we can try to apply the results of this work to reheat exchanger systems to evaluate further the advantages and disadvantages of using the active electrolysis method of pool boiling.
- In this study, the departure rate of the bubbles was only investigated qualitatively through a high-speed camera, and the dynamic properties of the bubbles were not investigated from a mechanical perspective. In the future, it would be possible to consider adding a numerical simulation method to enable a quantitative analysis of the bubbles' dynamic properties and verify the electrolysis process's effect on phase change heat transfer.

doi:10.6342/NTU202404361

## Reference

[1] Nukiyama, "THE MAXIMUM AND MINIMUM VALUES OF THE HEAT-Q TRANSMITTED FROM METAL TO BOILING WATER UNDER ATMOSPHERIC-PRESSURE," *International Journal of Heat and Mass Transfer,*, pp. vol. 27, no. 7, pp. 959-970, 1984, 1984.

[2] Y. Koizumi, "Outline of Boiling Phenomena and Heat Transfer Characteristics," in *Boiling*, 2017, pp. 1-11.

[3] C. S. Meena, A. Kumar, S. Roy, A. Cannavale, and A. Ghosh, "Review on Boiling Heat Transfer Enhancement Techniques," *Energies,* vol. 15, no. 15, 2022, doi: 10.3390/en15155759.

[4] J. S. Kim, A. Girard, S. Jun, J. Lee, and S. M. You, "Effect of surface roughness on pool boiling heat transfer of water on hydrophobic surfaces," *International Journal of Heat and Mass Transfer,* vol. 118, pp. 802-811, 2018, doi: 10.1016/j.ijheatmasstransfer.2017.10.124.

[5] H. T. Phan, N. Caney, P. Marty, S. Colasson, and J. Gavillet, "Surface wettability control by nanocoating: The effects on pool boiling heat transfer and nucleation mechanism," *International Journal of Heat and Mass Transfer,* vol. 52, no. 23-24, pp. 5459-5471, 2009, doi: 10.1016/j.ijheatmasstransfer.2009.06.032.

[6] H. Chu, X. Yu, H. Jiang, D. Wang, and N. Xu, "Progress in enhanced pool boiling heat transfer on macro- and micro-structured surfaces," *International Journal of Heat and Mass Transfer,* vol. 200, 2023, doi: 10.1016/j.ijheatmasstransfer.2022.123530.

[7] S. Hong, S. Jiang, Y. Hu, C. Dang, and S. Wang, "Visualization investigation of the effects of nanocavity structure on pool boiling enhancement," *International Journal of Heat and Mass Transfer,* vol. 136, pp. 235-245, 2019, doi:

10.1016/j.ijheatmasstransfer.2019.03.001.

[8] M. Boroumand Ghahnaviyeh and A. Abdollahi, "Experimental study of the effect of mechanical vibration on pool boiling heat transfer coefficient of Fe3O4/deionized water nanofluid," *Journal of Thermal Analysis and Calorimetry,* vol. 147, no. 24, pp. 14343-14357, 2022, doi: 10.1007/s10973-022-11591-2.

[9] S. Alangar, "Effect of boiling surface vibration on heat transfer," *Heat and Mass Transfer,* vol. 53, no. 1, pp. 73-79, 2016, doi: 10.1007/s00231-016-1803-8.

[10] T. Tanaka, K. Miyazaki, and T. Yabuki, "Electrolytic Bubble Nucleation Activation in Pool Boiling of Water: Heat Transfer Enhancement and Reduction of Incipient Boiling Superheat," *International Journal of Heat and Mass Transfer,* vol. 157, 2020, doi: 10.1016/j.ijheatmasstransfer.2020.119755.

[11] H. J. Cho, J. P. Mizerak, and E. N. Wang, "Turning bubbles on and off during boiling using charged surfactants," *Nat Commun,* vol. 6, p. 8599, Oct 21 2015, doi: 10.1038/ncomms9599.

[12] A. V. Ruban, H. L. Skriver, and J. K. Nørskov, "Local equilibrium properties of metallic surface alloys," in *Surface Alloys and Alloys Surfaces,* (The Chemical Physics of Solid Surfaces, 2002, pp. 1-29.

[13] T. Young, ""III. An essay on the cohesion of fluids,"" *Philosophical transactions of the royal society of London,,* no. no. 95,, pp. pp. 65-87,, １８０５.

[14] Y. Takata *et al.*, "Effect of surface wettability on boiling and evaporation," *Energy,* vol. 30, no. 2-4, pp. 209-220, 2005, doi: 10.1016/j.energy.2004.05.004.

[15] B. Bourdon, R. Rioboo, M. Marengo, E. Gosselin, and J. De Coninck, "Influence of the wettability on the boiling onset," *Langmuir,* vol. 28, no. 2, pp. 1618-24, Jan 17 2012, doi: 10.1021/la203636a.

[16] B. Shen *et al.*, "Bubble activation from a hydrophobic spot at “negative” surface

superheats in subcooled boiling," *Applied Thermal Engineering,* vol. 88, pp. 230-236, 2015, doi: 10.1016/j.applthermaleng.2014.10.054.

[17] X. Wang, S. Zhao, H. Wang, and T. Pan, "Bubble formation on superhydrophobic-micropatterned copper surfaces," *Applied Thermal Engineering,* vol. 35, pp. 112-119, 2012, doi: 10.1016/j.applthermaleng.2011.10.012.

[18] R. N. Wenzel, "Resistance of solid surfaces to wetting by water," (in English), *Industrial and Engineering Chemistry,* Article vol. 28, pp. 988-994, 1936, doi: 10.1021/ie50320a024.

[19] K. Seo, M. Kim, and D. H. Kim, "Validity of the equations for the contact angle on real surfaces," *Korea-Australia Rheology Journal,* vol. 25, no. 3, pp. 175-180, Aug 2013, doi: 10.1007/s13367-013-0018-5.

[20] A. B. D. Cassie and S. Baxter, "Wettability of porous surfaces," *Transactions of the Faraday Society,* vol. 40, pp. 0546-0550, 1944, doi: 10.1039/tf9444000546.

[21] M. Faraday, "VI. Experimental researches in electricity.-Seventh Series," *Philosophical Transactions of the Royal Society of London,* vol. 124, pp. 77-122, 1834, doi: doi:10.1098/rstl.1834.0008.

[22] J. Taylor, "Introduction to error analysis," *the study of uncertainties in physical measurements,* 1997.

[23] M. R. Mata Arenales, S. K. C.S, L.-S. Kuo, and P.-H. Chen, "Surface roughness variation effects on copper tubes in pool boiling of water," *International Journal of Heat and Mass Transfer,* vol. 151, 2020, doi: 10.1016/j.ijheatmasstransfer.2020.119399.

[24] H.-C. Cheng, H.-C. Lin,and P.-H. Chen, "Boiling heat transfer enhancement over copper tube via electrolytic and electrostatic effects," *Applied Thermal Engineering,* vol. 199, 2021, doi: 10.1016/j.applthermaleng.2021.117584.

[25] H.-C. Cheng, Z.-X. Jiang, T.-L. Chang, and P.-H. Chen, "Effects of difference in wettability level of biphilic patterns on copper tubes in pool boiling heat transfer," *Experimental Thermal and Fluid Science,* vol. 120, 2021, doi: 10.1016/j.expthermflusci.2020.110241.

[26] H.-C. Cheng, Y.-Y. Chen, T.-L. Chang, and P.-H. Chen, "Effect of biomimetic fishbone-patterned copper tubes on pool boiling heat transfer," *International Journal of Heat and Mass Transfer,* vol. 162, 2020, doi: 10.1016/j.ijheatmasstransfer.2020.120371.

[27] W. M. Rohsenow, "A method of correlating heat transfer data for surface boiling of liquids," *Cambridge, Mass.: MIT Division of Industrial Cooperation,* １９５１.

[28] M. Faraday, "-vi-experimental-researches-in-electricity-seventh-series.pdf>," *Philosophical Transactions of the Royal Society of London,* no. no. 124, pp. 77-122.